



Actin structure formation, membrane dynamics, and force generation during blood platelet spreading

Dissertation

for the award of the degree

“Doctor rerum naturalium”

of the Georg-August-Universität Göttingen

within the doctoral program in Physics

of the Georg-August University School of Science (GAUSS)

submitted by

Anna Zelená

from Prague (Czech Republic)

Göttingen, 2022

Thesis Committee

Prof. Dr. Sarah Köster

Institute for X-Ray Physics
University of Göttingen

Dr. Florian Rehfeldt

Experimental Physics I
University of Bayreuth

Dr. Marco Tarantola

Dept. Fluid Dynamics, Pattern Formation, and Nanobiocomplexity
Max Planck Institute for Dynamics and Self-Organization, Göttingen

Members of the Examination Board

Referee: **Prof. Dr. Sarah Köster**

Institute for X-Ray Physics
University of Göttingen

2nd Referee: **Dr. Florian Rehfeldt**

Experimental Physics I
University of Bayreuth

Further members of the Examination Board

Prof. Dr. Timo Betz

Third Institute of Physics - Biophysics
University of Göttingen

Prof. Dr. Andreas Janshoff

Institute for Physical Chemistry
University of Göttingen

Prof. Dr. Stefan Klumpp

Institute for the Dynamics of Complex Systems
University of Göttingen

Prof. Dr. med. Niels Voigt

Institute of Pharmacology and Toxicology
University Medical Center Göttingen

Date of Oral Examination:

March 22nd, 2022

Contents

1	Introduction	1
2	Blood Platelets	3
2.1	Platelet Origin and Structure in Hemostasis	3
2.1.1	Origin of Platelets	3
2.1.2	Structure of Platelets in the Resting Phase	5
2.1.3	The Role of the Cytoskeleton in Activated Platelets	8
2.1.4	Platelets in Hemostasis	9
2.2	Cell-Matrix Interactions	11
2.3	Time-Resolved Investigation of Actin Structures in Platelets	12
2.4	Contractile Forces in Platelets	13
3	Theoretical Background	17
3.1	Fluorescence Microscopy	17
3.1.1	Fluorescence	17
3.1.2	Epi-Fluorescence Microscope	19
3.1.3	FLIM Microscope	21
3.2	Metal-Induced Energy Transfer (MIET)	21
3.3	TFM Reconstruction	24
3.3.1	Elasticity Theory	24
3.3.2	Methods of Data Analysis	26
4	Materials and Methods	29
4.1	Platelet Purification and Staining Protocols	29
4.2	Fabrication of PAA Substrates	33
4.2.1	Coverslip Silanization	35
4.2.2	Substrates for Thrombin Experiments	35
4.2.3	Substrates for Fibrinogen Experiments	38
4.2.4	Elasticity Measurements of PAA Gels	41
4.3	Microscopy	45
5	Data Analysis	47
5.1	Calculation of Force with Optical Flow	47
5.2	Determination of the Time Point of Force	51

5.3	Determination of the Actin Boundary	52
5.4	Determination of Force Hot Spots and Spatial Correlation with Actin Boundary	53
6	Time-resolved MIET Measurements of Blood Platelet Spreading and Adhesion	57
6.1	Abstract	58
6.2	Introduction	58
6.3	Experimental	60
6.4	Results and Discussion	67
6.5	Conclusions	74
6.6	Acknowledgements	75
6.7	Supplementary Information	76
7	Force Generation in Human Blood Platelets by Actin Structures	83
7.1	Abstract	84
7.2	Introduction	84
7.3	Materials and Methods	86
7.4	Results	91
7.5	Discussion and Conclusions	98
7.6	Acknowledgments	99
8	Summary, Conclusion and Outlook	101
	Bibliography	103
	Acknowledgements	123
	Abbreviations	125

Chapter 1

Introduction

Blood platelets are essential to the formation of blood clots and prevent uncontrolled bleeding. They are non-nucleated fragments of larger bone marrow cells known as megakaryocytes. Platelets undergo fast morphological changes during blood flow recovery when they change their shape from a discoid to a flat structure [1]. The platelet cytoskeleton is reorganized during this process of activation and, ultimately, forms a strong adhesion bond to the extracellular matrix. In this stage, platelets have been observed to produce forces in the range of several hundred nN, which are comparable to much larger cell systems [2]. Despite its biological importance, the exact mechanism of the cell-matrix interaction and adhesion process remains elusive. Investigating these processes is crucial to understanding the healthy hemostatic mechanism and may help patients with congenital bleeding diseases, cancer patients, and patients with transplanted organs.

Platelets pose a challenge to conventional methods used for the study of cell-matrix interactions, as their small size is a limiting factor for most known methods, which have to compromise between high lateral and axial resolution. In the first study presented in this thesis, we apply the metal-induced energy transfer (MIET) method, which reaches high axial and lateral resolutions. With this method, we are able to map the basal membrane structure of living platelets. The rapid mode gives access to the dynamic rearrangement of the basal membrane. The second study focuses on actin structures and their correlation with contractile forces. By combining actin imaging [3] with traction force microscopy (TFM) [2, 4, 5], we investigate the force dependency of platelet contraction on thrombin activation and fibrinogen coverage of the contractile matrix. In this thesis, we investigate the biophysical properties of platelet-matrix adhesion, highlighting the dynamics of membrane and actin mor-

phology as well as force generation.

In Chapter 2, we discuss the biological background on human blood platelets and review the relevant methods used for their biophysical investigation. In the Section 2.1, we briefly introduce blood platelet function and origin. We describe the cytoskeleton and its role in activation and hemostasis while highlighting observations from time-resolved studies. In Sections 2.2, 2.3 and 2.4, we review the state-of-the-art methods used for the study of cell-matrix interactions, time-resolved studies of actin structures and contractile forces. Chapter 3 summarizes the theoretical background for this thesis. We provide the methodological background on fluorescence microscopy, MIET and TFM. In Chapter 4, the experimental procedures and sample preparations used in Chapters 6 and 7 are described in greater detail. The preparation of platelets is presented in addition to the staining procedures. Additionally, we describe the fabrication of polyacrylamide (PAA) substrates featuring different levels of fibrinogen coverage and thrombin activation as well as the used microscopy set-ups. In Chapter 5, we provide a detailed overview of the data analysis. We describe parameters used for the TFM analysis, the determination of actin boundary and spatial correlation between actin boundary and formed hot spots. Chapter 6 explains the results obtained by MIET experiments where we reveal the basal membrane structure and the membrane adhesion in a time-resolved manner. This chapter is published as Ref. [6]. In Chapter 7, we study how actin structures correlate with contraction forces under various conditions. Finally, in Chapter 8, the results of both studies are summarized. We conclude by discussing possible future experiments and open questions.

Chapter 2

Blood Platelets

This chapter summarizes the current knowledge about human blood platelets and the methods used to investigate them. Section 2.1 focuses on the origin of platelets and their cellular structures on a scale from the resting stage to hemostasis. Sections 2.2 and 2.3 provide an overview of different methods used to investigate cell-matrix interactions as well as time-resolved studies, which enable investigation of actin structures within platelets. Finally, Section 2.4 covers methods used to determine the cellular forces produced by platelets on a single cell level. These studies are essential for our understanding of the continuity of the hemostasis process and provide the foundation for the diagnosis and treatment of bleeding disorders.

2.1 Platelet Origin and Structure in Hemostasis

2.1.1 Origin of Platelets

Platelets with a diameter of 2-5 μm are the smallest cells in the human body [1]. By the end of the nineteenth century, platelets were identified as blood elements contributing to hemostasis with an unknown physiological significance [7]. Since then, the study of blood platelets has advanced and helped with uncovering for example their significance in the immune system [8]. Though platelets lack a nucleus and genes (apart from mitochondrial genome), they possess many of the typical characteristics of cells, including a range of organelles and receptors [1]. It is interesting to note the other example of non-nucleated blood elements, red blood cells, lose their nuclei in the process of enucleation [9], while platelets remain non-nucleated throughout their entire lifespan [1]. This is a consequence of platelets arising from the fragmentation of larger megakaryocytes (MKs) in the bone marrow and therefore

platelets are often referred to as cell fragments [1].

Platelets have a lifespan that ranges between 8 and 12 days [1]. If they are not activated, they reach the end of their lifespan in the spleen by antibody-mediated clearance by macrophages [10]. Their production rate is controlled to keep the physiological range between $150\text{-}400 \times 10^9$ platelets per liter of blood [1], but the exact amount of produced platelets may fluctuate around 10^{11} per day [1]. To maintain a balanced physiological state, the production requires a steady mechanism, which is precisely controlled.

The origin of platelets as small fragments of MKs is a commonly accepted fact, identified in bone marrow [11, 12] and stem cell-differentiation culture systems [13–15]. Many theories have been formulated to describe this mechanism, e.g., cytoplasmic fragmentation, platelet budding, and proplatelet formation [1]. Recent evidence leans towards the proplatelet formation theory [16], and thus it will be presented in more detail.

The idea of proplatelet formation was first introduced in 1906 by J. H. Wright, who suggested that platelets are formed as fragments from MKs extensions [17]. The production of platelets, called thrombopoiesis, starts with stem cells in the bone marrow [16]. Differentiation of the stem cells, called megakaryopoiesis, produces MKs from hematopoietic stem cells [16]. Once MKs mature, they begin a rapid invagination of their membrane system and accumulate cytoplasmic proteins essential for correct platelet functioning. Subsequently, the cytoplasm of MKs undergoes a reorganization and forms long, thin extensions, known as proplatelets [16]. The existence of proplatelet extensions has been confirmed by scanning electron microscopy (SEM) of bone marrow [11] in a wide range of mammalian species [18]. It has been further hypothesized that these proplatelets undergo a fragmentation into platelets [19].

The formation of proplatelets starts with thick pseudopodia, which elongate into thin tubules of 2-4 μm diameter with the intracellular contents at their ends [20]. The formed structures take on the shape of small balls of platelets connected through a thin bridge. To finalize the process of platelet assembly, the formed bridges are ruptured by the shear of blood flow. The individual platelets are thus released into the blood circulation [20]. Experiments with MK cultures confirmed the formation of platelets and proplatelets *in vitro*. Furthermore, the resulting structures show a similar appearance to native platelets [21, 22], however their morphology strongly differs as shown by later evidence [23]. These experiments and discoveries confirm that the formation of platelets is a complex process, possibly influenced by other, cellular mechanisms, which is still not fully known to us.

2.1.2 Structure of Platelets in the Resting Phase

Most platelets inside a functional blood flow circulate in a resting phase as small discoids. Upon damage of a blood-vessel, they rapidly change their shape and form aggregates [1]. To achieve such a fast morphological change, they require an unique structure. The mature platelets in the resting phase consist of a cytoplasmic membrane with a so-called open canalicular system (OCS), various surface receptors, a cytoskeleton, and secretory organelles such as α -granules, dense granules, and lysosomes [24]. Interestingly, platelets also contain simple mitochondria and glycosomes [24].

The plasma membrane with OCS is covered by an exterior coat called the glycocalyx. The glycocalyx contains a layer of glycoproteins and glycolipids with negative charge. The negative charge provides a repulsive force between platelets to prevent their spontaneous activation and aggregation in the blood flow [1]. Recently, the function of the glycocalyx has been shown to extend to the regulation of calcium ions and membrane stiffness [25]. The thickness of the glycocalyx has been reported to be in the range of 15-20 nm, thicker than for red or white blood cells [26]. The relatively large thickness of the glycocalyx is responsible for protecting many diverse types of receptors on the platelets surface, and it may play a role in regulating the platelet lifespan [1].

The plasma membrane is unstretchable and incompressible with a comparable morphology to any other cell in the human body. However, it contains some specific features seen only in platelets. The main structure in the resting phase has a thin polar membrane made of two layers of phospholipid molecules, folded such that the surface repels other platelets to prevent coagulation. It results in an even surface with a large number of small apertures of the OCS as pathway for transport between extracellular and intracellular space. During activation, those small apertures of OCS are responsible for an increasing membrane area of platelets covering the wound [1, 24]. The plasma membrane contains a large group of receptors. Here we mention the most important ones responsible for the adhesion and activation.

Glycoproteins (GPs) GPIb-IX-V and integrin α IIb β 3 (sometimes called also GPIIb/IIIa) mediate the first critical step in platelet adhesion, facilitating binding primarily to von Willebrand factor (vWF) and fibrinogen. Besides that, integrin α IIb β 3 is linked to actin filaments via cytoskeletal proteins, e.g., filamin[27], talin, and vinculin [28].

The membrane of the resting platelet exposes an inactivated tissue factor (TF) and negatively charged GP phosphatidylserine on its surface. During activation, the TF release micro particles, which enhance binding of coagulation factors Va, VIIa and Xa to the surface phosphatidylserine [24]. The area below the membrane contains a system of thin actin filaments, which are responsible for the shape change and translocation of receptors over the platelets surface during spreading [1]. Additionally, platelets contain multiple receptors for their activation. Important to mention here is a membrane group of protease-activated receptors (PAR) responsible for detecting thrombin occur as a result of platelet spreading [24].

The intracellular area inside platelets contains a system of contractile cytoskeletal structures and randomly distributed secretory organelles [1]. The platelet cytoskeleton consists of microtubules, actin, spectrin, and intermediate filaments like desmin and vimentin [1, 29]. In the resting phase, the shape is determined by ring-shaped microtubule coils in the so-called marginal band (MB) [20]. The shape change during spreading of the MB is provided by dynein/kinesin activity [30, 31]. Besides the MB, the shape of the resting platelet is supported by a cross-linked network of the actin filament cytoskeleton with organelles in the central area [32, 33] and by the spectrin membrane cytoskeleton interconnected with actin filaments [34, 35]. Actin takes up to 20% of the total protein mass in platelets [36] and exists as monomeric globular form (G-actin) or filamentous form (F-actin) [37]. In the resting phase, F-actin constitutes up to 50% of all actin [37]. Very little is known about the structure of intermediate filaments in platelets. The presence of vimentin and desmin has been confirmed by staining antibodies [29], revealing a similar distribution for both of them in the surrounding plasma membrane, cytoplasm, and granulomer zone [29].

Besides the membrane and cytoskeleton, platelets contain a large group of organelles randomly distributed along the intracellular area in the resting phase. However, during the activation process, the dense body organelles are moved toward the platelet center and secrete their contents through the OCS [24]. A single platelet contains around 50 to 80 α -granules in the intracellular space in the resting phase. Their fusion is the first indication that the cell is damaged, and it can also be a signal for several platelet disorders. Platelets also contain several MK-synthesized proteins such as thrombospondin, P-selectin, coagulation factor V and vWF, which has a major function in the primal hemostasis [24]. Besides the α -granules, platelets contain dense granules with substances such as adenosine triphosphate (ATP), adenosine diphosphate (ADP), serotonin, pyrophosphate, calcium and magnesium, but also a small amount of fibrinogen. Upon activation, the fibrinogen and vWF inside of

α -granules are released, thus initiating the platelet-platelet and platelet-endothelial cells of the blood vessel interactions [24].

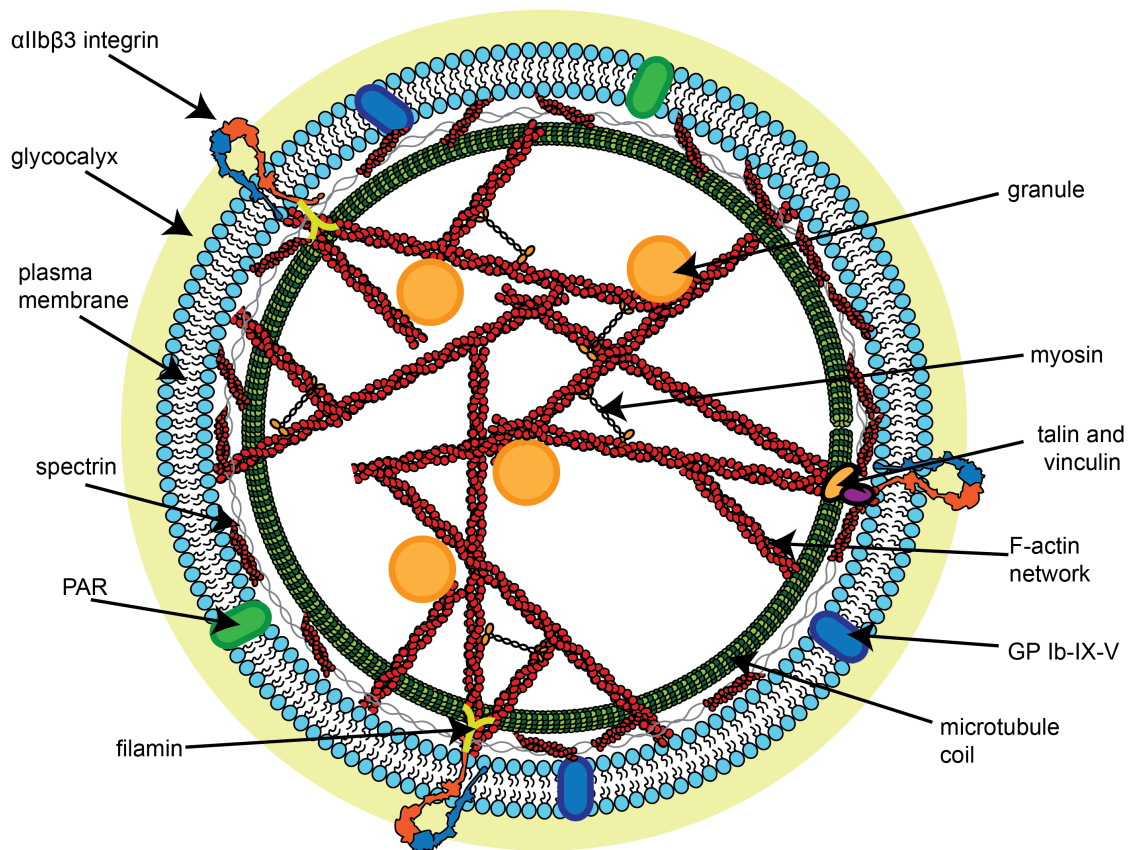


Figure 2.1: Schema of a resting platelet. The plasma membrane contains several important receptors like PAR (green), GPI-IX-V (blue) and integrin α IIb β 3 (orange β -subunit, blue α -subunit). Besides that, the β -subunit is connected via filamin (yellow) or talin-vinculin (orange/purple) to the actin filaments (red). The whole structure is covered by a glycocalyx coat (light green circle). Underneath the membrane, the spectrin network (grey) is bound to the actin cortex (red). Actin filaments (red) are connected with myosin motors (orange). The microtubule coils consists of tubulin dimers (dark/light green ring), which are responsible for the discoid shape of platelets. The shape change during spreading is provided by kinesin/dynein (neglected in these scheme). In general all organelles are indicated as yellow circles. The intermediate filaments are neglected for clarity.

2.1.3 The Role of the Cytoskeleton in Activated Platelets

As described in the previous Section 2.1.2, platelets contain a large amount of signaling organelles and receptors responsible for the activation of platelets. Platelets undergo a large shape change from discoid to a very thin and flat structure upon activation. The cytoskeleton is primarily responsible for this change of shape [1]. Microtubules and actin are among the most well-characterized structures of cells. They have polarized structures that serve as a path for the movement of molecular motors, such as actin-connected myosin [38] and microtubule-connected dynein [30] and kinesin [39]. They are responsible for the shape of the cell in the resting phase and change the shape of the platelet during activation and spreading. The cytoskeleton is also responsible for the cell's resistance to tensile forces and shear stress [40, 41]. Besides that, the cytoskeleton inside platelets is responsible for intracellular trafficking and spacial organization. It has an essential function as a connector to the extracellular environment, transducing mechanical forces and generating mechanical forces in turn [40, 41].

Upon activation, the cytoskeleton is completely remodeled. Although each platelet can differ in the final shape, all platelets follow a general spreading pattern. The most important step for the process of shape change are the polymerization and reorganization of actin filaments [1]. Upon activation by thrombin, the F-actin increases its proportion from 50% up to 70% of all actin [37]. Through OCS, organelles and granules can secrete their contents and possibly initiate the actin polymerization [40, 42].

The MB (microtubules organized in a ring structure) upon activation starts to coil and forms a smaller ring in the central area of the cell and thus allow the platelet to change its shape [30]. In the activated platelet, it has been suggested that acto-myosin tension leads to the spherical shape [30]. Upon initial contact to the endothelial cells of a damaged blood vessel, platelets change from a disc to a sphere with elongated filopodia consisting of F-actin bundles [1]. During this time, they search for a suitable environment for their adhesion and start the centralization of organelles and granules. After adhesion to the damaged endothelium, integrin activation generates morphological changes from the discoid to the round and flat membrane [1]. Once the membrane is spread, the actomyosin stress fibers are formed in varying shapes, e.g., circular, triangular, or spindle-like shapes and forms a strong platelet-extracellular matrix interaction [1].

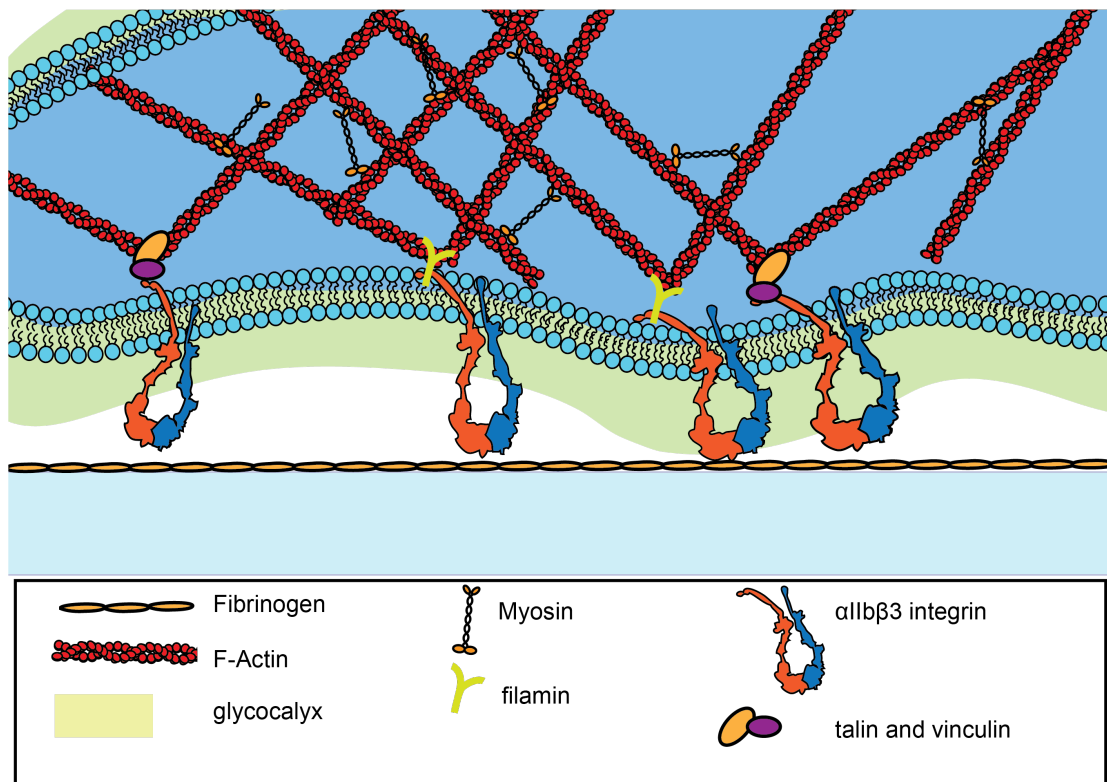


Figure 2.2: A schematic visualization of cytoskeletal structures inside a spread platelet on a substrate coated by fibrinogen. We show two examples of the connection between actin and integrin $\alpha\text{IIb}\beta\text{3}$ via filamin or talin-vinculin. FA spots are formed by accumulation of integrins $\alpha\text{IIb}\beta\text{3}$.

2.1.4 Platelets in Hemostasis

Platelets play an essential role during the process of blood clotting, known as hemostasis. As already mentioned, platelets undergo a fast morphological change upon an injury and form a blood clot, which helps restore the physiological blood flow. The first part of hemostasis (the initialization) includes the accumulation of platelets in the location of the injury. The second part consists of the coagulation cascade and forming of a blood clot [1].

Once a blood vessel is injured (vascular trauma), TF as a high-affinity receptor activates the factor VIIa and platelets start to mobilize to the blood vessel wall and thus initiate the first contact with the extracellular matrix. The mobilization occurs at low (in venous system $20\text{-}200\text{ s}^{-1}$) as well as at high (in arteries $300\text{-}800\text{ s}^{-1}$ and stenotic vessels $800\text{-}10,000\text{ s}^{-1}$) shear rates of the blood flow [43]. After the vascular injury, endothelial matrix proteins, like collagen or fibrinogen, are exposed to the blood flow and initiate the activation of blood platelets via receptors. At high blood flow rates, the collagen anchors plasma vWF, which interact with receptors (GP)Ib α

and GP Ib-IX-V. The platelets are immobilized directly on the matrix surface at low shear rates.

The coagulation cascade consists of interactions between several factors and their gradual activation is responsible for the full formation of blood clot. The initiator of the cascade is the interaction between TF and factor VIIa. This complex catalyzes the conversion of inactive protease factors IX and X into their active form IXa and Xa, but it is also responsible for the conversion of more factors VII into their active form VIIa and the production of a small amount of thrombin. This small amount of thrombin is insufficient to complete the fibrin formation, but sufficient to contribute to the amplification phase of coagulation. The thrombin is detected by the PAR receptor and its activation initiates the shape change from the resting phase of platelet. Thrombin also activates coagulation factors V, VIII and IX to generate their active forms. The prothrombinase complex Xa and Va increase the production of thrombin, which is then responsible for amplification of the coagulation cascade and converts fibrinogen to fibrin. In presence of factor VIIIa, more Xa is catalyzed and the coagulation cascade is amplified [1, 44, 45]. The receptor PAR responds to the presence of thrombin by an increase of concentration in the concentration calcium ions [1, 44, 45]. Once the initial layer of platelets is attached, the blood clot starts to recruit more platelets by releasing more thrombin from granules upon the increasing calcium concentration [1, 44, 45]. The fibrin network provides the connection between the platelets in the blood clot, as shown in Fig. 2.3.

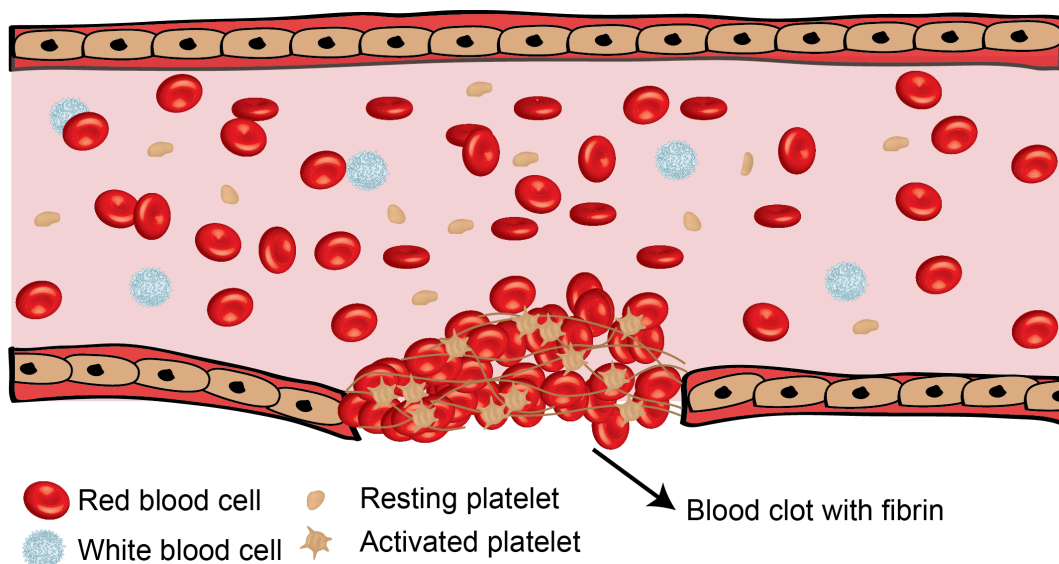


Figure 2.3: Schematic representation of the blood clot formation. Upon an injury, the platelets are activated and cumulated on the site of the injury in a large clot, thus restoring normal blood flow.

2.2 Cell-Matrix Interactions

Cell-matrix interactions describe the ability of a cell to stick to the extracellular matrix (ECM). Cell surface receptors (e.g., integrin $\alpha\text{IIb}\beta\text{3}$ and GP Ib-IX-V) mediate the adhesion to their extracellular ligands (e.g., fibrinogen, fibrin, collagen, or fibronectin). During the adhesion process, integrin molecules are clustered to form focal adhesions (FAs), which contain the structural and signaling molecules responsible for adhesion [1]. It is assumed that many adhesion types known for other mammalian cells like fibrillac adhesions, focal complexes, and podosomes [46] also apply to platelets. However, investigating focal adhesion in platelets is more challenging and usually requires improvements to conventional methods due to the small size of platelets. Here we present a short overview of methods that have been adapted to platelets. In early studies, high-resolution investigations were provided mainly by scanning electron (SEM) [47, 48] and transmitting electron microscopy (TEM) [48, 49]. They reveal information about the membrane structures in the resting phase and the organization of organelles in spread platelets as described in the previous sections. Additionally, SEM revealed the thickness of the platelet to be 40 nm at the periphery and around 100 nm for the cell center [47]. However, the preparation of samples for SEM or TEM requires dried and fixed cells.

Later experiments, implementing atomic force microscopy (AFM) [50–52], scanning ion-conductance microscopy (SICM)[53–56] or hopping probe ion conductance microscopy (HPICM),[57] provide a good picture of the shape of the apical membrane and confirm the involvement of the cytoskeleton in the spreading of platelets. With these methods, we can obtain a high resolution of the top membrane of living platelets, but their limitation is obvious. The basal membrane is not accessible with the scanning methods and the relatively slow speed of the scanning makes detailed investigation of spreading impossible. Those methods are often combined with conventional methods like fluorescence wide-field and confocal laser scanning microscopy (CLSM) to visualize adhesion molecules like fluorescently labeled integrins [58–60]. For the investigation of living platelets, mouse platelets are often preferred to human samples, because of a possible genetic labeling of cells. Mouse platelets have been used to observe actin nodules and structures similar to podosomes and study the dynamics of filamentous F-actin [42, 61].

The axial resolution can be increased by applying optical super-resolution methods like stimulated emission depletion (STED) and a combination of STED with 4Pi microscopy, known as isoSTED [62–64], which leads to an improvement of the

resolution down to < 21 nm in axial and 30 nm in lateral direction [65]. Platelets are very light-sensitive objects, so they have to be chemically fixed before observation with these super-resolution microscopy methods. However, compared to the SEM experiments [47], the samples observed with STED are hydrated and used for thickness measurements with results of 90 nm thickness at the periphery and about 320 nm in the center of the cell [66]. This comparison revealed that the dimensions of dried samples are smaller than those of hydrated samples.

The adhesion profile of the basal membrane can also be determined by traction force microscopy (TFM). The computation of these traction fields depends on the used mathematical model, displacement fields of beads inside of a soft substrate are used to calculate the forces exerted by a cell [2, 67, 68]. The generated forces are located at the basal membrane with distribution at so-called hot spots as locations of high traction forces [2].

Several methods to investigate the shape of the basal membrane have been developed. One of these, reflection interference contrast microscopy (RICM), uses a single monochromatic beam and has been used on mouse platelets. Results show distinguished zones between close contact areas with a distance of ~ 40 nm from the substrate, and regions with distances up to 110 nm [69]. This study provided unique quantitative insights into adhesion of platelets to protein coated surfaces, however a higher lateral resolution and its application on living human platelets in time-resolved studies remain elusive. An alternative to this method represents metal-induce energy transfer (MIET) technique. MIET provides a nanometer resolution in the axial direction, but it can provide also suitable lateral resolution of the image [70, 71]. MIET uses a knowledge of fluorophore behavior in presence of a thin metal film, responsible for modulation of de-excitation rate of the present fluorophore molecule [71]. Its application has been confirmed with larger cells [71–74] and can be further develop also for application with human platelets in time-resolved studies.

2.3 Time-Resolved Investigation of Actin Structures in Platelets

As introduced in Subsection 2.1.3, actin is involved in the spreading process of the platelet. It has been observed that platelets on stiff substrates tend to contain actin organized into stress fibers (often also called stress fiber-like structures) [1], bundles of actin filaments tensed by myosin II molecular motors [75–77]. In larger mammalian

cells, the stress fibers usually end in the FAs localized by accumulated molecules of integrin [78].

Due to lack of a nucleus and their very small size, platelets cannot be transfected or micro-injected with fluorescent dyes. Thus the experiments are more challenging than with typical cells. So far actin structures have been primarily observed and investigated on chemically fixed samples. The common techniques use phalloidin [79, 80], anti-actin antibodies [79, 81, 82] or electron microscopy studies [83, 84].

The first live-cell actin staining experiments comparable with those of chemically fixed samples, were performed with mouse platelets using Life-Act green fluorescent protein (GFP) staining [42, 61]. GFP-actin protein has been used to study actin dynamics in living platelets and define structures in living platelets as actin nodules [42]. The addition of thrombin causes actin nodules to vanish as stress fibers are formed [42]. A follow-up study used structure illumination microscopy (SIM) and direct stochastic optical reconstruction microscopy (dSTORM), along with total internal reflection fluorescence microscopy (TIRF), to present a detailed investigation of the actin nodules and their connection to talin and vinculin [61]. Talin and vinculin have importance in mechano-sensing [85, 86] via connections to the actin cytoskeleton [61, 87].

With these previous experiments, a few questions have been answered. However, the real goal is to apply these methods to human platelets. Studies in our group successfully applied live-cell actin staining by silicon-rhodamine (SiR) fluorophore to human platelets in combination with a stiff surface and revealed similar structures as observed with phalloidine stained samples [3]. The SiR actin represents a staining alternative for structures otherwise complicated to transfect [88].

2.4 Contractile Forces in Platelets

This section focuses on methods applicable to platelets for measuring cell adhesion forces. It has been observed during bulk experiments with blood clots, that contraction forces of platelets are responsible for controlling the retraction and stiffening of the clot [89]. However, the distribution of forces among platelets in the clot remains unknown. A first step to a better understanding of that mechanism are single cell experiments. One of the first methods used to directly measure the adhesion force of single platelets is AFM [90, 91]. AFM can be used to obtain a morphological map of apical membrane structures (Section 2.2) and for measurements of cellular

forces with a pN resolution. A typical setup uses a flexible cantilever of a known stiffness with a pyramidal probe tip for indentation mode and a protein-coated tip for measuring contractions of platelets. The indentation studies revealed the elastic modulus of a single platelet to be in the range of 1 to 50 kPa [52]. The stiffness in a spread platelet increases from the area with accumulated organelles (1.5-4 kPa) to the periphery (53 kPa) and refers to the distribution of actin filaments [52]. Recent studies with thrombin-activated platelets show even higher stiffness with values up to 224 kPa at the periphery and 32 kPa around the central area [92]. To investigate cell contraction, the tip of the cantilever as well as the substrate matrix are coated with fibrinogen. The platelet is thus forced to attach between the two fibrinogen layers, and the deflection of the cantilever by contraction forces has been measured [90]. The averaged forces show values of 19 nN [93]. AFM presents an exact method for measuring contraction forces of a single platelet. However, the geometry of the experiment focuses only on one direction and can be used only for the measurement of a single cell at a time. Similar to AFM, the previously mentioned SICM can also be used for measuring the elastic modulus of different regions in platelets and observing changes in distribution of stiffer and softer regions during spreading between the central area and the periphery [54].

Unlike the methods mentioned above, the adhesion profile of cells requires application of method implementing more dimensional resolution. One of the techniques, traction force microscopy (TFM) allows investigation of the behavior of platelets in the presence of an elastic substrate and can research their response to the matrix stiffness at a high spatial resolution. TFM rapidly developed over the past few years, including many approaches in a two-dimensional (2D) geometry, calculating tangential forces [94], but also in a three-dimensional (3D) geometry, which reconstructs cell forces applied to a fibrous matrix around the whole cell [95, 96]. A method between 2D and 3D is known as 2.5D TFM and it extends the 2D TFM analysis to calculations for normal forces [97, 98]. TFM is a reconstructive technique based on detection of substrate deformations by light microscopy. The commonly used substrates are usually elastic materials, with multiple approaches to detect the deformation. Two main approaches for experiments with platelets have been applied, one using poly(dimethylsiloxane) (PDMS) elastic micro-pillars [77, 99–101] and the other using elastic hydrogels containing fluorescent beads [2, 67, 68] or microdots [102]. In addition to those approaches, an experimental setup using molecular force sensors based on Förster resonance energy transfer (FRET) is under development [103–105]. A micro-pillar array uses a matrix covered by a large number of flexible pillars coated

by adhesive proteins like collagen or fibrinogen. Platelets are pipetted on top of this structure and allowed spread. Contracting platelets displace the micropillars, and the force is obtained from images of the deformation. The investigation of platelets with micro-pillars is usually performed on a micro-thrombus. Thus, several platelets are attached to each other. The average contractile force by a single platelet is established around 2.1 ± 0.1 nN and shows a dependence on thrombin concentration as more platelets interact in the micro-thrombus [99]. Following studies used fibronectin and vWF coated micro-pillars and showed that the activity of nonmuscle myosin IIA ATPase regulates the microthrombi contractile forces through Rho kinase (ROCK) and myosin light-chain kinase [77] and integrin α IIb β 3 and GP Ib-IX-V are important for the mechanotransducing of forces [106].

The hydrogel array uses protein coated elastic hydrogels with fluorescent beads as markers. With this method, we can achieve higher sensitivity and compute spatio-temporally resolved force fields rather than revealing total forces only. An optical microscope detects the displacement of the fluorescent beads caused by the deformation of the hydrogel by adherent spreading platelets. The measurement relies on substrate stiffness, the density of detected beads, and the mathematical algorithm used for the data analysis [2, 67]. With initial TFM experiments, it has been observed that platelets on soft gels (4 kPa) exert forces in the range of 34 nN in 25 minutes [67]. On stiffer substrates (19-83 kPa), platelets can reach an averaged value of forces around 200 nN in the range of 30 minutes. Moreover, the spatial resolution allows the detection of so-called force hot spots of the traction forces at the periphery of the cell [2].

Those results are in an agreement with observations by an integrative tension sensor (ITS) for force transmitted by the integrin α IIb β 3 [105]. ITS detected two levels of integrin tensions in platelets, high-level tensions and low-level tensions. High-level tensions are generated in a ring pattern and low-level tensions are generated in a dot pattern. By simultaneous visualization of FA and forces, they observed a co-localization of FAs and integrins at high-level tensions [105].

As a simple alternative to TFM, a method called platelet contraction cytometry (PCC) was developed. PCC is based on the displacement of fibrinogen-coated microdot pairs on hydrogels and can work under a range of various stiffnesses and inside of a microfluidic chip [102]. With this method they measured forces proportional only to the monomeric fibrin microdot area and their displacement. The force of a single cell is determined in the range of 20-50 nN [102]. PCC experiments revealed that the mechanosensitive contraction is dependent on the Rho/ROCK pathway by testing

platelets from populations with bleeding disorders (Wiskott-Aldrich syndrome) inhibiting the function of ROCK and thus the myosin IIa activity [102]. This method represents an alternative for fast clinical tests, however, the reduced spatial resolution may present an issue for exact contraction force measurements.

Chapter 3

Theoretical Background

Despite the fact that several methods for biophysical investigations of the platelet spreading process and force development have been applied, investigation in living cells remains difficult. To evaluate the outcome of our experiments, we further describe the theory underlying the methods used to investigate spread platelets. Section 3.1 describes how fluorescence microscopy works and gives examples of its usage in this thesis. Section 3.2 focuses on the theory behind metal-induced energy transfer (MIET). Section 3.3 describes the elasticity theory and compares different existing methods for bead detection in traction force microscopy (TFM) and the used analytical tools in more detail.

3.1 Fluorescence Microscopy

Fluorescence microscopy is a technique that uses light emission from chemical molecules specifically bound to the structure of interest of our biological samples and thus reveal their morphology. This method is very sensitive and has a broad spectrum of applications, from the investigation of simple organisms through cellular structures to single molecules. This broad spectrum makes it an excellent choice for our investigation of human blood platelets. Here, we apply two main methods using the fluorescence mechanism: well-known epi-fluorescence microscopy as shown in Fig. 3.1A and fluorescence-lifetime imaging microscopy (FLIM) as shown in Fig. 3.1B.

3.1.1 Fluorescence

Fluorescence is a physical phenomenon where chemical molecules, called fluorophores, can absorb certain energy photons and subsequently emit photons with

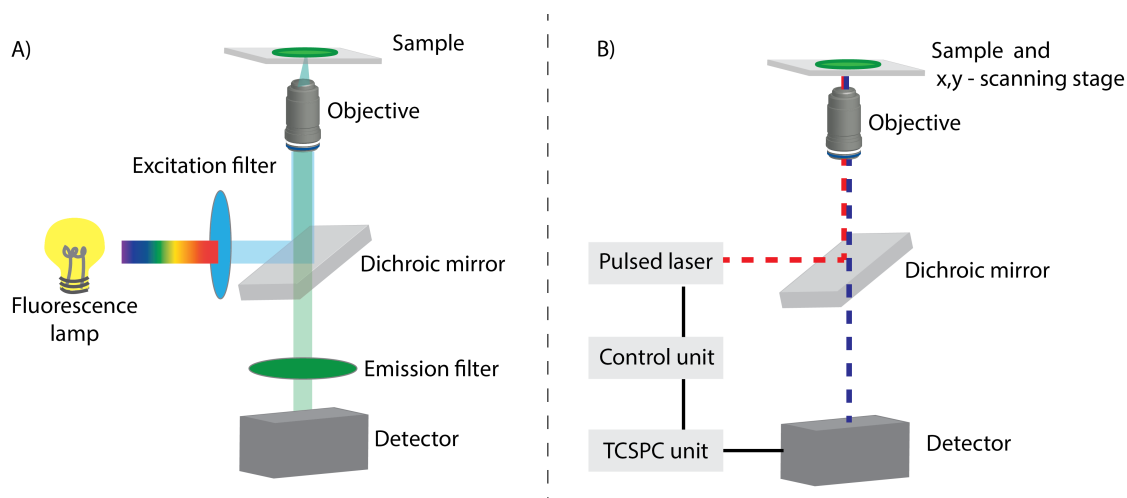


Figure 3.1: A) Inverted fluorescence microscope setup. The filtered light in blue is reflected by a dichroic mirror in the direction of the sample. The light emitted by the sample is collected by the objective, passes through the dichroic mirror and the emission filter, and reaches the detector. B) FLIM microscope setup. Here, a pulsed laser serves as a light source and the key element is the TCSPC unit, which is responsible for classifying each photon according to the arrival time with respect to the last laser pulse.

lower energy. From the quantum mechanic point of view, the fluorophore can be seen as a system of energy states (displayed as horizontal lines in the so-called Jablonski diagram in Fig. 3.2), namely a ground state S_0 and higher energy states. Here we only consider the first excited state S_1 for the sake of simplicity. The absorbed photon can come directly from a light source as shown in Fig. 3.2A or as a result from an energy transfer between donor and acceptor molecules, as shown in the example of Förster resonance energy transfer (FRET) in Fig. 3.2B [107].

By absorption of an excitation photon, the system is excited into a higher energy state S_1 . Following the law of the conservation of energy, the energy of the absorbed photon has to be equal to the energy difference between the ground state S_0 and the excited state S_1 . If the energy of the absorbed photon is larger than this difference, the molecule can undergo changes in vibration, rotation or it can also move into a higher electronic orbital S_2 . This means that the molecule generally allows more transitions with a broad range of energies as shown in an example of the absorption spectrum Fig. 3.3, but it also leads to a partial energy loss of the absorbed photon in heat. This energy loss causes a difference between the excitation and emission spectra known as the Stokes shift as shown in Fig. 3.3.

The excited state of the molecule is unstable, and eventually, the molecule returns back to its ground state S_0 . The excess energy is either emitted as a fluorescence photon or undergoes a non-radiative decay via thermal heat. The average time

necessary for the molecule to return from the S_1 state back to the ground state S_0 is called fluorescence lifetime τ and is given by

$$\tau = \frac{1}{k_f + k_{nr}} \quad (3.1)$$

where the k_f is the probability that the energy is emitted in the form of photon and k_{nr} represent the probability of a non-radiative decay. The probability that the energy is emitted in the form of fluorescence photon is called the quantum yield (QY), and it is given by

$$\text{QY} = \frac{k_f}{k_f + k_{nr}} = k_f \tau. \quad (3.2)$$

The fluorescence lifetime τ typically occurs on the order of nanoseconds, and it is very sensitive to the local environment [108]. Its detection can help us to answer questions concerning, for example, the position of the fluorophore in space and thus monitor the spatiotemporal dynamics of the system.

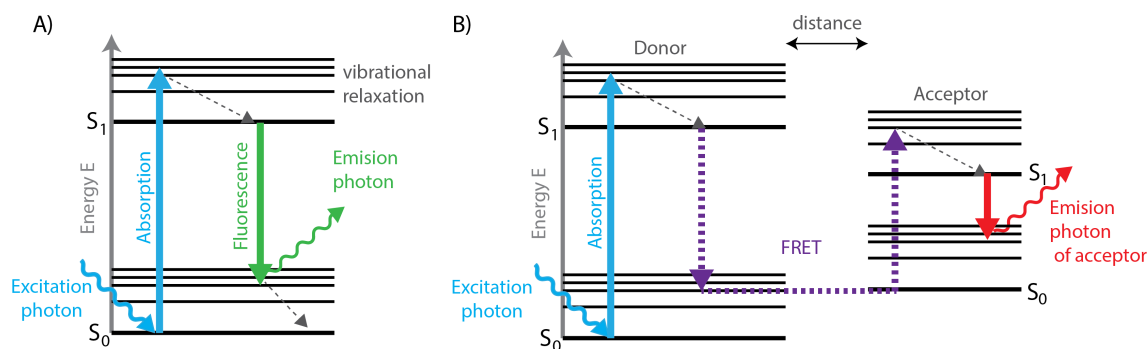


Figure 3.2: Jablonski diagrams illustrate the energy states of an excited molecule by the horizontal black lines. The bold lines are the lowest vibrational level of the corresponding energy state. Thinner lines represent the higher vibrational levels. The different colored arrows represent the various transitions that can transfer energy between the molecular states and are split into radiative and non-radiative transitions. A) Fluorescence occurs when an excited molecule relaxes back to the lower energetic state. The energy initially received as a photon is emitted again as a photon. B) In the presence of a second fluorophore, we can observe the effect of FRET. The energy is released during the donor molecule's relaxation phase is transferred via dipole-dipole interaction to the acceptor. It leads to an emission of photons from the acceptor molecule.

3.1.2 Epi-Fluorescence Microscope

Fluorescence can be beneficial in many scientific fields as presented here by application in an inverted epi-fluorescence microscope. The schematic of a typical inverted

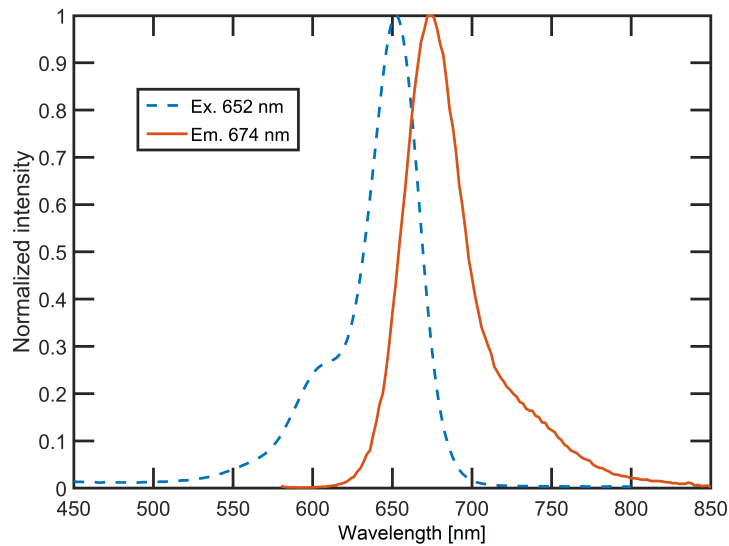


Figure 3.3: Spectrum of SiR actin [88]. The blue dashed curve shows the absorption spectrum of the dye and the red curve the emission spectrum. The peak of the emission is shifted to longer wavelengths which is known as the Stokes shift.

epi-fluorescent microscope is shown in Fig. 3.1A. We consider as a light source a fluorescence arc lamp, but it can be also replaced by a laser diode or high-power light-emitting diodes (LEDs), depending on the construction of an individual microscope. The construction with the fluorescence arc lamp requires an excitation filter to obtain the right excitation wavelength of the used fluorophores. A dichroic mirror reflects the filtered wavelength spectrum into an optical path through the objective to the sample. The dichroic mirror can reflect or transmit light depending on its wavelength. This is useful if we need to send the light of different wavelengths in two different directions. It usually reflects the shorter-wavelength excitation light up to the sample in the inverted microscope, while the longer-wavelength emission light passes through the dichroic mirror to the detector.

When the reflected light reaches the sample, it is absorbed by the fluorophore. Afterward, the fluorophore emits fluorescent light, which travels through the objective to the dichroic mirror. Thus, choosing the correct construction of such a mirror is essential. An emission filter then filters the emitted light. The objective plays the double role of focusing the excitation light onto the sample and the emitted light onto the detector of choice. In this case, either a charge-coupled device (CCD) or a complementary metal-oxide-semiconductor (CMOS) camera.

3.1.3 FLIM Microscope

In this thesis, we consider as FLIM a system based on a confocal scanning microscope that uses time-correlated single-photon counting (TCSPC) for fluorescence decay measurements. FLIM microscopy produces its images based on differences in the decay rate from the excited state to the ground state. The contrast between pixels is the lifetime of individual fluorophores and it is influenced by their emission spectra. The fluorescence lifetime has been defined in Eq. 3.1 as the average time that the fluorophore stays in an excited state. The lifetime measurement is more robust than a fluorescence intensity measurement, as the sample preparation or concentration do not influence it. However, further data analysis usually requires a large number of collected photons and thus, the fluorescent dye has to be stable and equally distributed throughout the sample.

For measuring the fluorescence decay at each pixel, TCSPC is implemented. This is a common technique for the detection of single-photon emission. The light source is a pulse laser and each detected photon is collected in a histogram according to the arrival time with respect to the last laser pulse. Once the histogram of the delay times is built, we obtain an estimated fluorescence decay shape. According to the number of components included in the signal, this can be exponentially or bi-exponentially fitted. The system has to be also corrected for the dead-time between the sensor's switching for the laser pulse and the recording of the signal. The dead-time of the system is usually in the order of tens of nanoseconds, but for very high temporal resolution investigations this shift can be a critical point.

3.2 Metal-Induced Energy Transfer (MIET)

Metal-induced energy transfer (MIET) is a simple and reliable super-resolution method for axial localization of fluorescence markers in nanometer range. The principle of MIET describes a phenomenon of fluorescence quenching in presence of a metal layer and it is similar to the earlier mentioned method FRET, which uses principle of transferring energy from an excited fluorophore molecule (donor) to another fluorophore molecule (acceptor) and this leads to a dramatic change of the radiative decay rate of the donor [107]. In contrast, MIET uses a non-radiative transfer between a fluorescent molecule, which acts like a donor, and surface plasmons within a metal film, which acts like an acceptor [71]. This leads to an acceleration of the

radiative decay rate. The energy transfer is distance-dependent, thus the fluorescence lifetime of a well defined fluorophore, can be directly converted into distance values with a help of a so-called MIET curve as shown in Fig. 3.4A [109]. The fluorescent molecule has to be well characterized in the used media by its refractive index and QY.

Compared to FRET, where molecules of donor and acceptor need to be at a very close distance (1-10 nm) and their spectra need to overlap, MIET can reach molecules up to 200 nm above the metal surface and register their positions in the nanometer range [109]. Additionally, MIET requires only one type of fluorescence staining. This makes MIET a very suitable method for many complex biological systems, which can be complicated for staining like blood platelets.

The evaluation of MIET measurements and its modeling has been well described in Ref. [110–112], here we briefly focus on the most important parts. The geometry of the experiment plays an important role as described by Fig. 3.4B. The fluorescent molecule is considered here to be an electric dipole emitter with orientation angles θ, ϕ along direction $\kappa = (\sin \theta \cos \phi, \sin \theta \sin \phi, -\cos \theta)$ per solid angle $\sin(\theta)d\theta d\phi$. The angular distribution of the electric-field amplitude \mathbf{E} into direction (θ, ϕ) is given by

$$\mathbf{E}(\theta, \phi) = \sin \beta [\mathbf{t}_s E_s^{\parallel}(\theta) \sin \phi + \mathbf{t}_p E_p^{\parallel}(\theta) \cos \phi] + \mathbf{t}_p \cos \beta E_p^{\perp}(\theta), \quad (3.3)$$

$$E_p^{\perp}(\theta) = \frac{n_g w_g}{w_m} \frac{q}{n_m} T_p e^{i w_m z} \quad (3.4)$$

$$E_p^{\parallel}(\theta) = \frac{n_g w_g}{n_m} T_p e^{i w_m z} \quad (3.5)$$

$$E_s^{\parallel}(\theta) = \frac{n_g w_g}{w_m} T_s e^{i w_m z} \quad (3.6)$$

where β is the angle between the vertical axis and the dipole axis and z is the distance between the fluorophore molecule and the surface as shown in Fig. 3.4B. q is the in-plane component of the wave vectors, w_g and w_m are z -components of the wave vectors in glass and medium, respectively, n_g is the refractive index of glass and n_m denotes the refractive index of medium, and $T_p(\theta)$ and $T_s(\theta)$ are Fresnel's transmission coefficients for plane p - and s -waves through the material interface

along direction κ , \mathbf{t}_s and \mathbf{t}_p are orthogonal unit vectors perpendicular to the direction given by κ ,

$$\mathbf{t}_s = \frac{\kappa \times \mathbf{e}_z}{|\kappa \times \mathbf{e}_z|}, \mathbf{t}_p = \mathbf{t}_s \times \kappa, \quad (3.7)$$

where \mathbf{e}_z is a unit vector perpendicular to the surface. Detailed equations using Fresnel's relations can be found in Ref. [109, 111, 113, 114].

Once the electric field amplitude is known, the full emission rate of the molecule is calculated by integrating the Poynting vector over a closed surface enclosing the molecule (more in Ref. [115]). We obtain the radiative emission power $S(\theta, z)$ as:

$$S(\theta, z) = S_{\perp}(z) \cos^2 \theta + S_{\parallel}(z) \sin^2 \theta, \quad (3.8)$$

where $S_{\perp}(z)$ is the radiative emission rates of the molecule oriented perpendicular and $S_{\parallel}(z)$ is the radiative emission rates of the molecule oriented parallel to the substrate. The emission power $S(\theta, z)$ is related to the probability of transition from the excited state to the ground state by emitting the energy in form of photon k_f as defined in Eq. 3.1. Taking into account the probability of non-radiative decay, which is determined by their QY as defined in Eq. 3.2, the final expression for the excited-state fluorescence lifetime $\tau_f(\theta, z)$ is

$$\frac{\tau_f(\theta, z)}{\tau_0} = \frac{S_0}{\text{QY} \cdot S(\theta, z) + (1 - \text{QY})S_0}, \quad (3.9)$$

where S_0 is the total emission power of the free-space emitter, τ_0 is the free-space lifetime and QY is the previously defined quantum yield of the emitter. The lifetime-distance curve is obtained as an average overall possible spatial orientations of the emitter molecule, an example is shown in Fig. 3.4A.

The range of sensitivity can be influenced by the material used for the metal coating of the surface as well as by the thickness of the metal surface and the surrounding environment. The standard metal used for this technique is gold, usually deposited on top of a different metal for better adhesion [70, 71, 73]. MIET with different materials as the acceptor layer, e.g. graphene [116, 117], is under development.

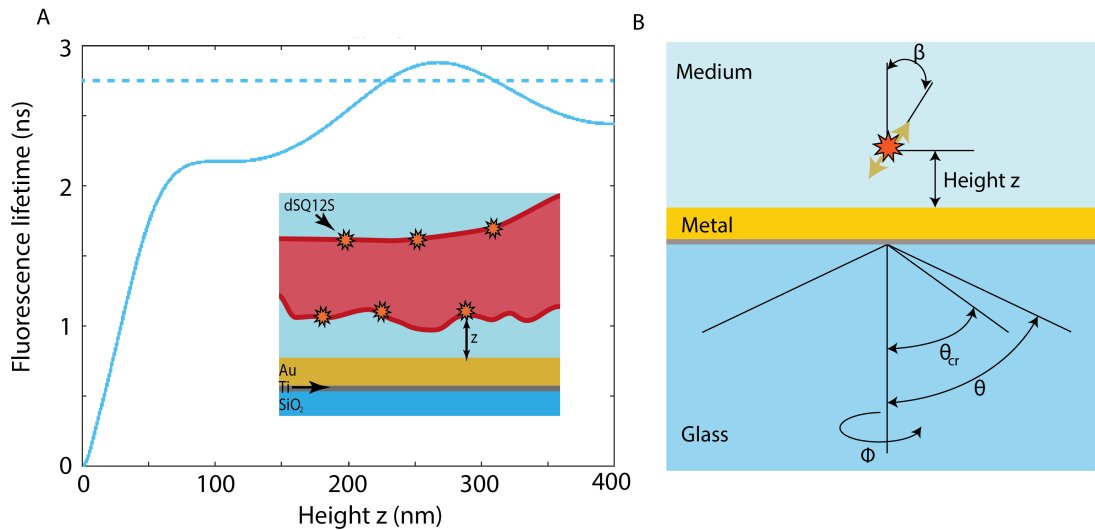


Figure 3.4: A) The so-called MIET curve shows the dependence of the fluorophore lifetime on its height z above the metal surface. The curve shown here is calculated for dSQ12S dye with a deposited metal layer of 15 nm gold and 2 nm titanium on a glass substrate. B) Geometry of a single electric dipole emitter (molecule of fluorophore) placed above a metal surface in a medium. The fluorescence is detected by a high NA objective from the side of the glass. The orientation of the emitter is described by the angles β between its dipole axis and the vertical axis and ϕ around the vertical axis. The angular distribution of radiation in glass is a function of angle θ . The total internal reflection between glass and water is θ_{cr} . The schema is adapted from Ref. [110].

3.3 TFM Reconstruction

Traction force microscopy (TFM) is a method used for determining traction forces produced on a surface by biological objects like cells. By measuring the displacement field of the surrounding matrix, we can obtain the forces. In TFM analysis, different approaches can be used based on elasticity theory, using calculations optimized according to the geometry and setup of the experiment. The deformation is always referred to an undeformed image, obtained before the cell adhesion [2, 67, 68] or after trypsinization of the adhesion surface [118, 119]. The theory behind the TFM has been described elsewhere, [94, 120] and here we briefly summarized the main principles.

3.3.1 Elasticity Theory

TFM measures the forces exerted by an adherent cell lying on a soft matrix. We assume a deformable body (e.g., elastic gel) on which is applied tangential tension exerted by cells, also known as traction forces. We always assume small deformations

of the body, which allows us to linearize equations and thus use the continuum elasticity theory [121]. In a Cartesian coordinate system we define a focal plane of the relaxed surface by coordinates (x_1, x_2) . The normal coordinate x_3 has a positive direction above the focal plane. Deformation is denoted by u_i along the coordinate i . The *strain tensor* ϵ is given in undeformed coordinates x_i [122] as:

$$\epsilon_{ij} = \frac{1}{2} \left(\frac{\partial u_j}{\partial x_i} + \frac{\partial u_i}{\partial x_j} + \sum_{k=1}^3 \frac{\partial u_k}{\partial x_i} \frac{\partial u_k}{\partial x_j} \right) \approx \frac{1}{2} \left(\frac{\partial u_j}{\partial x_i} + \frac{\partial u_i}{\partial x_j} \right). \quad (3.10)$$

Since we assume small displacement and strains, the last term in Eq. 3.10 can be neglected. Thus we define the strain, which measures the deformation of our material. To quantify the internal forces that neighboring particles exert on each other, we define the term *stress tensor* σ_{ij} as

$$\sigma_{ij} = \frac{F_i}{\delta x_j}. \quad (3.11)$$

According to the Inverted Hooke's law, if we consider linear elastic materials, the relation between stress σ_{ij} is and the strain ϵ_{ij} is given by

$$\sigma_{ij} = \frac{E}{1+\nu} \left(\epsilon_{ij} + \frac{\nu}{1-2\nu} \delta_{ij} \sum_{k=1}^3 \epsilon_{kk} \right), \quad (3.12)$$

where E is Young's modulus in N m^{-2} and ν is dimensionless Poisson's ratio. To solve the Eq. 3.12, we assume the adhesive substrate be infinitely large and thick, and forces are applied only in the 2D focal plane, it means that $x_3 = 0$. For this situation, we can solve the Eq. 3.12 by the Boussinesq solution, including the Green's function \mathbf{G}

$$\int_{\mathbf{R}^3} \mathbf{G}(\mathbf{x}' - \mathbf{x}) f(\mathbf{x}') d\mathbf{x}' = \mathbf{u}(\mathbf{x}), \quad (3.13)$$

$$\mathbf{G}(\mathbf{x}) = \frac{1+\nu}{2\pi E} \begin{pmatrix} \frac{2(1-\nu)r+z}{r(r+z)} + \frac{2r(vr+z)+z^2}{r^3(r+z)^2} x^2 & \frac{2r(vr+z)+z^2}{r^3(r+z)^2} xy & \left(\frac{z}{r^3} - \frac{1-2\nu}{r(r+z)} \right) x \\ \frac{2r(vr+z)+z^2}{r^3(r+z)^2} xy & \frac{2(1-\nu)r+z}{r(r+z)} + \frac{2r(vr+z)+z^2}{r^3(r+z)^2} y^2 & \left(\frac{z}{r^3} - \frac{1-2\nu}{r(r+z)} \right) y \\ \left(\frac{z}{r^3} + \frac{1-2\nu}{r(r+z)} \right) x & \left(\frac{z}{r^3} + \frac{1-2\nu}{r(r+z)} \right) y & \frac{z^2}{r^3} + \frac{2(1-\nu)}{r} \end{pmatrix}, \quad (3.14)$$

where $r = \sqrt{x^2 + y^2 + z^2}$.

Since we assume deformation only in the focal plane, the deformation observed near the surface simplifies the Eq. 3.13 and Eq. 3.14 [122, 123] to

$$\int_{\mathbf{R}^2} \mathbf{G}(\mathbf{x}' - \mathbf{x}) f(\mathbf{x}') d\mathbf{x}' = \mathbf{u}(\mathbf{x}), \quad (3.15)$$

$$\mathbf{G}(\mathbf{x}) = \frac{1 + \nu}{\pi E r^3} \begin{pmatrix} (1 - \nu)r^2 + \nu x^2 & \nu xy \\ \nu xy & (1 - \nu)r^2 + \nu y^2 \end{pmatrix}. \quad (3.16)$$

The traction forces are calculated by a regularized Fourier Transform Traction Cytometry (FTTC) [124].

3.3.2 Methods of Data Analysis

The theory behind the TFM has been explained. Here we focus in more detail on the theory behind the used algorithm. To find an optimal way to define the traction forces in practice is important to clarify options of different algorithms.

The detection of the substrate deformation is crucial and uses different algorithms e.g., particle image velocimetry (PIV) [2, 20, 68, 125–127], particle tracking velocimetry (PTV) [67, 97, 123, 128] and optical flow [2, 129, 130].

The PIV algorithm uses an approach of division of a large beads image into smaller sub-windows also called interrogation areas. The PIV assumes that all detected beads within the interrogation area move linearly in the same direction. The cross-correlation function determines the displacements. This method is suitable for a large density of beads. However, the chosen interrogation area has to fulfill several conditions. The displacement of the beads has to be smaller than the interrogation area. It has to include several particles so that the movement can be correlated with that of neighboring beads.

The PTV algorithm is one of the oldest techniques for beads displacement detection. It is based on the direct tracking of beads in the image, also known as the Lagrangian approach [131]. Each bead is detected in the image before deformation and in the deformed image and the algorithm tracks the trajectory. Compared to the PIV algorithm, PTV has a high computational cost thus, it requires a low beads density [131]. Moreover, with the PTV algorithm, eliminating falsely detected vectors can be extremely challenging. The advantage of this method is that the beads do not have to be homogeneously distributed as in the case of the PIV.

The optical flow algorithm is a more recently developed method [2, 129, 132]. Similar to the PTV, optical flow is a direct method for detecting beads. The dominant method used here is the Kanade-Lucas-Tomasi (KLT) feature tracker [130], which tracks single feature points (beads). Similar to the PIV method, the method assumes that the movement between neighboring beads is linear and small enough to be detected. The important assumption is that the pixel intensities of detected beads $I(x, y, t)$ are stable in time. First, a *Shi-Tomasi* corner detector finds corners in the image and calculates the motion of those corners between two consecutive frames. In the case of TFM, the detected corners belong to beads with a predefined quality level. Second, *pyramidal* KLT is used to measure individual beads with a search window of size w . The $I(x, y, t)$ moves by the distance $(\delta x, \delta y)$ in the time interval δt between two consecutive frames as described by

$$I(x, y, t) = I(x + \delta x, y + \delta y, t + \delta t). \quad (3.17)$$

By using Taylor expansion and removing common terms, we get

$$\frac{\partial I}{\partial x} \delta x + \frac{\partial I}{\partial y} \delta y + \frac{\partial I}{\partial t} \delta t = 0. \quad (3.18)$$

Dividing by δt we obtain the optical flow equation

$$\frac{\partial I}{\partial x} u + \frac{\partial I}{\partial y} v + \frac{\partial I}{\partial t} = 0, \quad (3.19)$$

where $u = \frac{\partial x}{\partial t}$ and $v = \frac{\partial y}{\partial t}$. To solve this equation correctly, we must assume that the movement between neighboring beads is similar. With this assumption we can determine u and v and obtain the movement of a single bead over time as

$$\mathbf{A} \begin{bmatrix} u \\ v \end{bmatrix} = \mathbf{b}, \quad (3.20)$$

where \mathbf{A} is a matrix of size $(w^2 \times 2)$ with rows filled by intensities (I_x, I_y) for each pixel at the corresponding position in the search window of size w . Vector \mathbf{b} has a length equal to w^2 filled with elements $-I_t$. To solve the least squares problem,

Eq. 3.20 is multiplied by \mathbf{A}^T

$$\begin{bmatrix} u \\ v \end{bmatrix} = (\mathbf{A}^T \mathbf{A})^{-1} \mathbf{A}^T \mathbf{b}. \quad (3.21)$$

The displacement vectors thus found are used in subsequent *pyramidal* levels to achieve better results. The application of *optical flow* with KLT is described in Chapter 5.

Finally, once the displacement field is calculated, independently of the method, traction forces are calculated in Fourier space using Fourier Transform Traction Cytometry (FTTC) [124]. Due to errors in the displacement fields, the FTTC has limitations, which are diminished by applying a regularization parameter.

Chapter 4

Materials and Methods

This chapter summarizes extended methods used in this thesis to investigate human blood platelets. Section 4.1 focuses on platelets purification from plasma concentrates, followed by actin and membrane staining. Section 4.2 describes the fabrication of polyacrylamide (PAA) gel substrates used for TFM experiments as well as stiffness characterization of PAA gels. Section 4.3 characterizes an experimental setup used for TFM experiments.

Note that parts of this chapter contain previously established methods published in Ref. [2, 3, 67] and they are adapted for Ref. [6] (Chapter 6) and for prepared manuscript in Chapter 7. All chemicals in their final and stock concentrations are found in Table 4.1.

4.1 Platelet Purification and Staining Protocols

The platelets are provided by the Department of Transfusion Medicine of the University Medical Center, Göttingen, in agreement with the ethical vote of the Ethics Committee of the University of Göttingen, votum 11/11/2009. To conduct these experiments, we use platelet concentrates donated by healthy human donors after their expiration for medical use. We store the concentrate on a shaker (Promax 1020, Heidolph Instruments, Schwabach, Germany) with a speed of 40-50 rpm at room temperature (RT) to prevent aggregation. The concentrate is used within four to seven days after the donation, to ensure enough healthy platelets for experiments [1]. On the day of the experiment, the platelets are purified fresh and used within four to five hours.

Fig. 4.1 illustrates the purification process. Used chemicals and their concentrations are shown in Table 4.1. We start by preheating PSG (PIPES Saline Glucose) and

HT-BSA (HEPES-Tyrode with bovine serum albumin) buffers in a 37°C water bath, where they will remain throughout the purification process. After opening the bag with a platelet concentrate, a sterile needle (Nr.1, \varnothing 0.90 x 40 mm, 100 Sterican®, B. Braun, Melsungen, Germany) is inserted through the opened valve and 2 mL of the liquid are withdrawn and discarded with a disposable syringe (2 mL, BD Discardit™ II, Becton, Dickinson and Company, Franklin Lakes, New Jersey, USA). To avoid contamination, the needle is kept in the bag, and 4 mL are withdrawn with a larger volume syringe (5 mL, BD Discardit™ II, Becton, Dickinson and Company). Prostaglandin E1 (PGE1 2.6 μ g/mL, Cayman Chemical Company, Ann Harbor, MI, USA) is added to the collected sample of platelets to prevent aggregation and activation. The PGE1-platelet mixture is then centrifuged for 20 minutes at $480 \times g$ and 21°C (Eppendorf Centrifuge 5810R, Eppendorf, Hamburg, Germany).

Following the centrifugation step, a pellet of platelets and red blood cells is settled at the bottom of the tube. The pellet is re-suspended in 4 mL of fresh and preheated PSG buffer after the supernatant has been removed. Following that, 10 μ L PGE1 (2.6 μ g/mL) is mixed with 90 μ L PSG buffer and added to the platelet suspension. The centrifugation step is repeated two more times with the same parameters and the formed pellet is re-suspended in fresh PSG buffer with PGE1 of the same concentration. After the third centrifugation, the supernatant containing PSG and PGE1 is removed. The pellet is re-suspended in 1 mL pre-warmed HT-BSA and placed on a rotor (MACS mix™ Tube rotator, Miltenyi Biotec) at a speed of 12 rpm to provide continuous movement of the sample and thus prevent platelets from spontaneous activation.

A hematocrit capillary (sodium heparinized 75 mm and 75 μ L, Hirschmann Laborgeräte GmbH, Eberstadt, Germany) is used to determine the concentration of purified platelets. To accomplish this, the capillary is filled with platelet solution, sealed with a wax lid, and centrifuged at $1000 \times g$ and 21°C for 10 minutes. We use a reading card (ZIPocrit, Microhemtocrif centrifuge, LW Scientific, Inc., Lawrenceville, Georgia, USA) to determine the platelet count. The expected range should be around $(2 - 10) \times 10^9$ platelets/mL. Purified platelets before experiments are diluted to a final concentration of 2×10^7 platelets/mL.

For membrane staining we use a squaraine dye with two zwitterionic amphiphilic anchors called dSQ12S [133], provided by Dr. Andrey Klymchenko (Laboratoire de Biophotonique et Pharmacologie, UMR 7213 CNRS, Université de Strasbourg, Faculté de Pharmacie, 74, Route du Rhin, Illkirch, France). Compare to other membrane dyes, dSQ12S shows a high affinity to the lipid membrane and it is optimal

choice for experiments with metal-induced energy transfer (MIET). When staining the membrane, we mix 1 μL of the dye and 999 μL of diluted and purified platelets to achieve a final concentration of dSQ12S 310 nM or 232.5 nM. The stained platelets are incubated in a tube for 5 minutes at 37°C and 5% CO₂. Following that, 10 μL PGE1 (2.6 $\mu\text{g}/\text{mL}$) is mixed with 90 μL HT-BSA and added to the platelet suspension prior to centrifugation. We centrifuge the tube for 5 minutes at 480 \times before re-suspending the pellet in 1 mL of HT-BSA. The stained platelets are then used directly in experiments.

For actin staining we use a commercially available dye SiR-actin (SiR-actin kit 50 nmol, stock solution 1 mM in dimethyl sulfoxide (DMSO), Spirochrome, Inc., Stein Am Rhein, Thurgau, Switzerland). The excitation and emission spectra of SiR actin are shown in Fig. 3.3. In tube 1 mL of purified and diluted platelets is stained for actin by adding the 0.5 μL of the SiR actin dye for a final concentration of 0.5 μM . The platelets are incubated for 15 minutes prior to the experiment, and the SiR actin is present in the solution throughout the experiment.

Table 4.1: Buffers and chemical solutions used for the experiments. For the definitions of the abbreviations used here, see Section 8.1

Chemical	Stock Solution	Working Solution
APS	10 mg powder in 100 μ L of MQ (10%)	5 μ L in 500 μ L of PAA stock solution with beads
dSQ12S	2.82 μ L of 1.1 mM dSQ12S in 7.18 μ L DMSO (310 μ M)	450 μ L of diluted platelets + 50 μ L of thrombin (final concentration 0.28 NIH units/mL) + 0.5 μ L of dye (232.5 nM or 310 nM)
Fibrinogen	100 mg of powder dissolved in 5 mL of 37°C MQ (20 mg mL ⁻¹)	5 μ L in 995 μ L of 1xPBS (0.1 mg L ⁻¹)
Fibrinogen Alexa 488	5 mg of powder dissolved in 3.33 mL of 0.1 M sodium bicarbonate pH = 8.3 (1.5 mg mL ⁻¹)	10 μ L in 140 μ L of 1xPBS (0.1 mg mL ⁻¹)
Fluorescent beads, 40 nm, carboxylated 505/515 nm ex/em	10 μ L of 5 % solid solution in 240 μ L of MQ (0.2% solid)	5 μ L in 495 μ L of PAA stock solution
HEPES buffer	119.15 g HEPES in 1 L MQ, pH 8.0 (0.5 M)	50 mL in 450 mL of MQ (50 mM) or 50 mL in 200 mL of MQ (100 mM)
HT-BSA	134 mM NaCl, 12 mM NaHCO ₃ , 2.9 mM KCl, 1 mM MgCl ₂ , 5 mM HEPES, 5 mM glucose, 0.34 mM NaH ₂ PO ₄ , pH = 7.4)	25 mL aliquot + BSA (5 mg mL ⁻¹)
PBS, 10X	1.37 mM NaCl, 27 mM KCl, 43 mM Na ₂ HPO ₄ · H ₂ O, pH = 7.2	50 mL in 450 mL of MQ (1X)
PAA stock solution, 34 kPa	0.75 mL of 2% Bis-Acrylamide, 2.5 mL of 40% Acrylamide, 6.75 mL of PBS	495 μ L of the PAA stock solution + 5 μ L of beads + 5 μ L of TEMED + 5 μ L of APS

PSG buffer	5 mM PIPES, 145 mM NaCl, 5 mM glucose, 4 mM KCl, 1 mM MgCl ₂ , 0.05 mM Na ₂ HPO ₄ , pH = 6.8	25 mL aliquot
PLL-g-PEG	1 mg mL ⁻¹ in 1X PBS (PLL(20)-g[3.5]-PEG(2 kDa))	0.1 mg mL ⁻¹ in 1X PBS
PLPP	Small aliquotes prefrozen (1X)	Directly used 5 μ L
Prostaglandin PGE1	1 mg powder dissolved in 940 μ L DMSO	10 μ L in 90 μ L of PSG (2.6 μ g mL ⁻¹)
SiR-actin	50 nmol vial in 50 μ L of anhydrous DMSO (1 mM)	0.5 μ L in 999.5 μ L of HT-BSA (0.5 μ M)
Sulfo-SANPAH	50 mg dissolved in 50 mL of 50 mM HEPES, pH = 8 (2.03 mM)	2 ml of 2.03 mM in 8 mL of 50 mM HEPES, pH = 8 (0.4 mM)
TEMED	1X stock solution	0.5 μ L in 500 μ L of PAA stock solution with beads
Thrombin	1 mg of 1 kU of thrombin from human plasma, specific activity 2800 NIH units/mg of protein + 10 mL of 0.1 % BSA, final stock concentration 280 U/mL	See Table: 4.2

4.2 Fabrication of PAA Substrates

In this Section, we present main approaches for fabrication of PAA substrates used for TFM experiments. All gels are fabricated in a similar way resolution in substrates with the same stiffness and thickness, however, some parts are slightly modified according to the final experiment and described more detailed in following sections. In Subsection 4.2.1 we describe preparation of silanized glasses, this part is the same for all demonstrated approaches and thus prepared glasses serve for adhesion of the PAA substrates. In Subsection 4.2.2 we describe preparation of PAA substrates employing

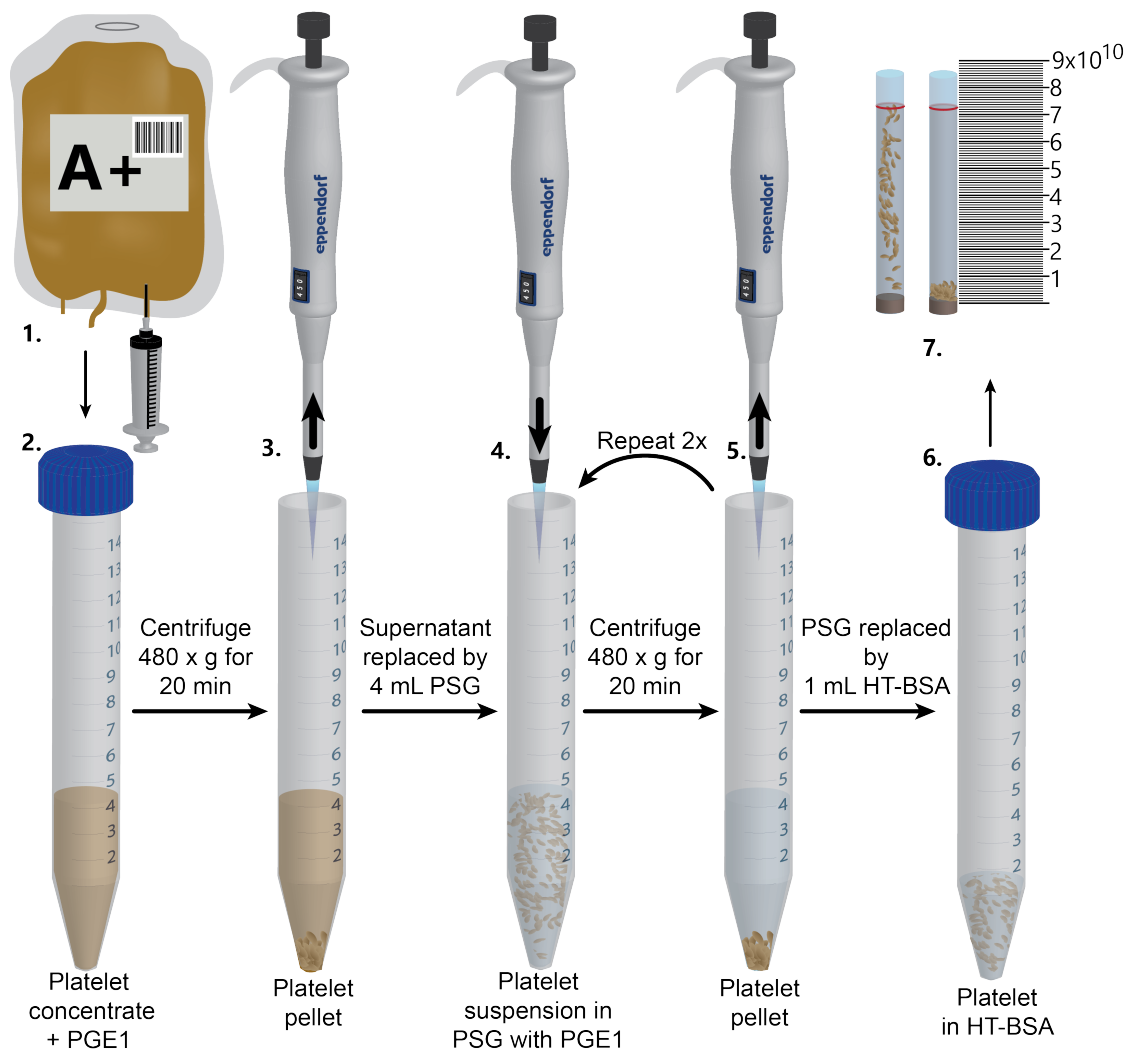


Figure 4.1: Schematic visualization of platelet purification and counting by a hematocrit capillary. 1. 4 mL of platelet concentrate is removed from the blood bag and placed in a 15 mL falcon tube. 2. 4 mL of the platelet concentrate is centrifuged with PGE1. 3. A pre-warmed PSG buffer replaces the supernatant. 4. The pellet is re-suspended in PSG with PGE1 and centrifuged again at $480 \times g$ for 20 min. 5. The supernatant is removed and replaced with 4 mL of fresh, pre-warmed PSG buffer, followed by centrifugation at $480 \times g$ for 20 min. 6. After the last centrifugation step, the supernatant is replaced by 1 mL HT-BSA buffer, and the pellet is re-suspended. 7. A small volume of the platelet concentrate is placed inside of a hematocrit capillary and centrifuged. From the reading card, we determine the concentration of the platelets in our prepared solution.

different thrombin concentrations. In Subsection 4.2.3 we describe preparation of PAA substrates used for TFM experiments using different degrees of fibrinogen coating.

4.2.1 Coverslip Silanization

The protocol has been modified in accordance with Ref. [134]. First, we make silanized glass coverslips, which serve as a bottom glass for adhesion of PAA substrates. The silanization treatment creates a strong covalent -Si-O-Si- bond between the substrate and the glass, as illustrated in Fig. 4.2. Square glass coverslips (24 mm × 24 mm No. 1, VWR, Radnor, Pennsylvania, USA) are cleaned with isopropanol and dried under a nitrogen stream. Following that, both sides of the glass coverslips are exposed to an air plasma (0.5 mbar, ZEPTO, Diener Electronics GmbH, Ebhausen, Germany) at 50 W for 1.5 minutes. The plasma cleaned coverslips are then soaked in a silanization solution consisting of 2%(v/v) 3-(trimethoxysilyl)propyl methacrylate (TMSPMA, Sigma-Aldrich, St. Louis, Missouri, USA) and 1%(v/v) acetic acid (100%, Carl-Roth GmbH, Karlsruhe, Germany) in absolute ethanol ($\geq 99.8\%$, Carl-Roth GmbH) for 10 minutes. The excess solution is aspirated, and the coverslips are rinsed with ethanol. Air-dried silanized coverslips are baked at 120° C for 1 hour and stored at RT. They can be stored in dry clean conditions in a ready-to-use state for several weeks.

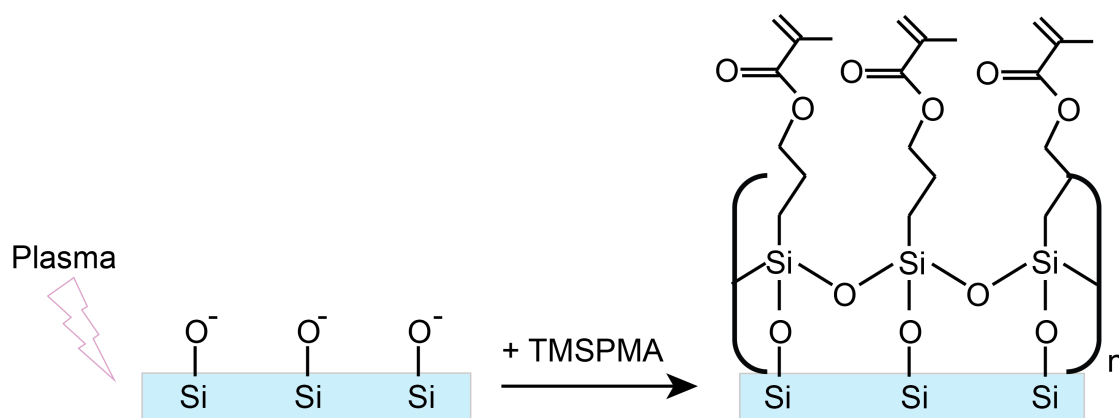


Figure 4.2: Chemical binding on the silanized glass coverslip. First, the glass coverslip is activated by plasma to obtain a negative charge of the surface. Second, the activated glass coverslip is exposed to the silanization solution containing 2%(v/v) TMSPMA.

4.2.2 Substrates for Thrombin Experiments

For the experiments employing different thrombin concentrations, circular glass coverslips (\varnothing 18 mm No. 1, VWR) are cleaned with isopropanol, dried under a nitrogen stream, coated with PlusOne Repel-Silane (GE Healthcare, Little Chalfont, UK) from

both sides for 5 minutes, and washed with ethanol. All round coated coverslips are dried and stored in a clean Petri dish (\varnothing 14 cm, Corning®Gosselin™, Corning) before usage. The PAA stock solution is prepared prior to the experiment no longer than four weeks and store at 5° C. The PAA stock solution is prepared according to the Table 4.1 of final stiffness 34 kPa.

495 μ L of the PAA stock solution is mixed with 5 μ L carboxylated beads (0.2% solids, FluoSpheres, carboxylate-modified microspheres, 40 nm in diameter, yellow-green, 505/515 nm, Thermo Fisher Scientific Inc., Waltham, MA, USA). The beads dispersion is prepared according to the Table 4.1 and homogenized in an ultrasonic bath for 10 minutes prior to the experiment. The whole process is performed under the hood to avoid dust contamination and because of manipulation with hazardous materials. The silanized coverslips are prepared according to Subsection 4.2.1 and they are cleaned of any dust particles stuck to the surface by a stream of nitrogen and placed inside of an isopropanol cleaned Petri dish. The catalyst ammonium persulfate (APS) is prepared from powder according to Table 4.1 and stored in the fridge at 5° C.

We place all material and chemicals under the hood and try to process following step fast to prevent formation of uneven gels. The addition of 5 μ L APS (10% APS, Bio-Rad Laboratories Inc.) and 0.5 μ L TEMED (Tetramethylethylenediamine, Bio-Rad Laboratories Inc.) initiates the polymerization. The PAA solution with beads, APS and TEMED is mixed and 10 μ L of the final mixture are pipetted on the circular, PlusOne Repel-Silane-treated coverslip and covered by the squared silanized coverslip. Once the liquid is in touch with the silanized glass, the liquid equally distributes between the two glass coverslips and forms a structure glass-gel-glass. The gel is polymerized upside-down for 1 hour under the hood protected from direct light. After the polymerization, the gel is soaked in phosphate buffered saline (PBS) and the circular glass coverslip is removed. The top layer of the gel is coated twice with 150 μ L Sulfo-SANPAH (0.4 mM in 50 mM HEPES buffer (pH=8), Thermo Fisher Scientific Inc.) and activated by applying UV light for 8 minutes (365 nm 2 tube 8 W, Herolab GmbH Laborgeräte, Wiesloch, Germany). Subsequently, 150 μ L of fibrinogen solution (100 μ g/mL, CalBiochem-Merck KGaA, Darmstadt, Germany) is added on top of the gel and incubated overnight for at least 10 hours at 5° C to achieve uniform coverage. Coated gels are washed with PBS and kept submerged in PBS until used in the experiments. The process is described in the schema in Fig. 4.3.

This volume of the gel creates a thickness around 50 μ m to avoid cells sensitivity to the stiff glass surface underneath. A small leakage of the gel on sides or shrinking to the center during polymerization cause small deviations in the thickness and before

every experiment the gels go through a quality check. We investigate the thickness of the gel by measuring the difference of the upper and lower layers of beads, and we discard gels thinner than $50\ \mu\text{m}$.

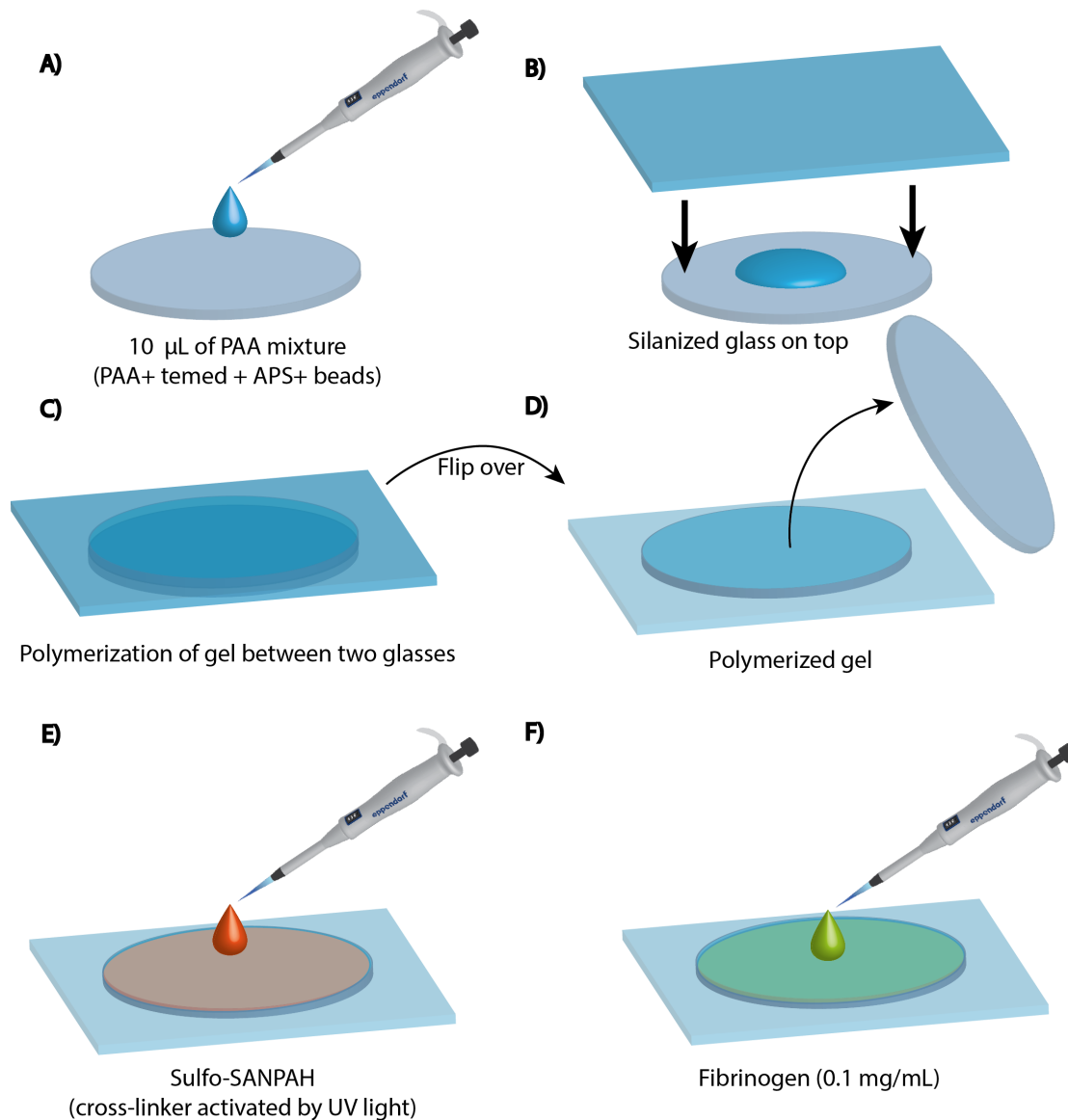


Figure 4.3: The schematic pictures of the preparation steps of substrates for experiments with different thrombin concentrations. A) A round glass coverslip with $10\ \mu\text{L}$ of unpolymerized PAA mixture. B) Adding the silanized bottom glass coverslip and forming a sandwich structure. C) Polymerization. D) Removal of the round glass. E) Sulfo-SANPAH cross-linking. F) Protein coating with $100\ \mu\text{g}/\text{mL}$ fibrinogen.

4.2.3 Substrates for Fibrinogen Experiments

For testing different degrees of fibrinogen coating, we use micro-patterned substrates and PLL-g-PEG coated beads. The reason for using PLL-g-PEG coated beads rather than carboxylated beads is discussed further below. First, we prepare (polydimethylsiloxane) PDMS stencils, which serve as a well for clear location of our pattern and reduce the amount of used chemicals. Second, we prepare micro-pattern glass coverslips and PLL-g-PEG modified beads. At last, we assemble the final gels for the fibrinogen experiments.

We start with a large plastic Petri dish cleaned by iso-propanol and blow-dried with nitrogen. In a large weighting boat, PDMS cross-linker (Sylgard®Silicone Elastomer Curing Agent, Dow Corning, Midland, Michigan, USA) is mixed in a ratio of 1:10 with the PDMS-elastomer base (Sylgard®, 184 Silicon Elastomer Base, Dow Corning). We place the mixture in the desiccator to remove residual air bubbles and pour it into the cleaned Petri dish as a very thin layer. Height variations are not a problem, so the PDMS can still be used for the experiment. We bake the PDMS in a Petri dish for 1 hour at 65° C. Once the thin PDMS layer is baked, we can cut out our stencils. For this purpose, we use a disposable biopsy puncher (\varnothing 3.5 mm Harris Uni-Core, US Pat. No.7093508, Qiagen GmbH, Hilden, Germany) to prepare wells and with a scalpel we carefully cut the PDMS into small areas. Those stencils we use for the following step with patterning to reduce the amount of used chemicals and define our printed area.

Next we prepare the micro-patterned glass by PRIMO (Alveóle, Paris, France) as shown in Fig. 4.4. The PRIMO module includes a UV laser diode (375 nm) and a digital micro-mirror device (DMD) to project digital pattern masks directly on the surface. The control system of the UV laser diode exposes the sample according to the pattern (loaded as a gray-scale 8-bit image shown in Fig. 4.4), which allows creating a controlled protein gradient or patterns of different concentration [135]. The PRIMO module is installed with an inverted fluorescent microscope (IX83, Olympus, Hamburg, Germany) with a motorized stage. The system is equipped with a 20 \times objective (LUCPLFLN, 20 \times /0.45 N.A. air, Olympus) and controlled *via* the software Leonardo (Alveóle). The first step in the patterning process is to create an anti-fouling layer on our substrate used for the protein pattern. We use isopropanol cleaned and nitrogen dried round glass coverslip (\varnothing 20 mm, No. 1 thickness, VWR, Radnor, Pennsylvania, USA). This glass coverslip is exposed to air plasma for 3 minutes at 40 W. On the plasma cleaned coverslip we attach one of our prepared stencils. This way, we create

a small well with a diameter of 3.5 mm, which we can easily fill with a small volume of liquid thus avoiding redundant chemical waste. As the anti-fouling layer, we use 10 μL of PLL-g-PEG (0.1 mg mL^{-1} in 1X PBS (PLL(20)-g[3.5]-PEG(2 kDa)), SuSoS AG, Dübendorf, Switzerland) and let it incubate for 1 hour. After 1 hour, the well is washed with PBS three times and left in a closed Petri dish before the patterning. The well stays filled with the PBS to prevent drying out until the UV illumination takes place. The PRIMO is calibrated according to the system instruction. A clean glass coverslip from the same batch as our coated glass coverslip is placed in the holder and marked by a highlighter pen (STABILO BOSS ORIGINAL Textmarker yellow, Heroldsberg, Germany). We manually focus on the top side of the glass coverslip and press the button for calibration. As a calibration mask, we use a picture with sharp edges and including gray gradients. Thus, the system could test if everything is perfectly aligned. Once we have prepared the system, we place our coated glass coverslip with the stencil in the sample holder and focus on the top surface of the glass coverslip. For precise focusing a water-soluble pen can be used to mark the glass surface next to the chamber. This is especially important for printing very small patterns. The PBS in the well is replaced by 5 μL of PLPP (Product of Liaison for Protein Patterning, Alveole). The PLPP degrades the passivated layer of PLL-g-PEG during exposure to UV light to a degree that is linearly dependent on the dose of the UV light [136]. The maximum dose we use for printing a pattern is 2000 mJ/mm^2 corresponding to 100% fibrinogen coverage. According to the linear dependence between dose and coverage, we prepare samples with 25% and 10% of the dose. After exposure to the UV light, the glass area inside the well is washed three times with PBS and subsequently filled with 10 μL of fibrinogen solution (100 $\mu\text{g}/\text{mL}$, CalBiochem-Merck KGaA). The fibrinogen protein is incubated inside the well for 2 hours at 5° C and then washed three times with PBS. The printing is checked on one sample from the same batch by replacing the unlabeled protein by fluorescent-labeled fibrinogen (100 $\mu\text{g}/\text{mL}$, AlexaFluor 488 conjugate, Ex/Em: 495/519 nm, Invitrogen, Darmstadt, Germany). For experiment is used only unlabelled fibrinogen. After washing off the remaining unbound protein, the pattern is ready to be transferred onto the PAA gel.

In contrast to the gels used for experiments with different thrombin concentrations in Section 4.2.2, we use in combination with micro-patterning PLL-g-PEG coated fluorescent beads [137]. We take a small volume of 12 μL of the stock beads dispersion (5% solids, FluoSpheres, carboxylate-modified microspheres, 40 nm in diameter,

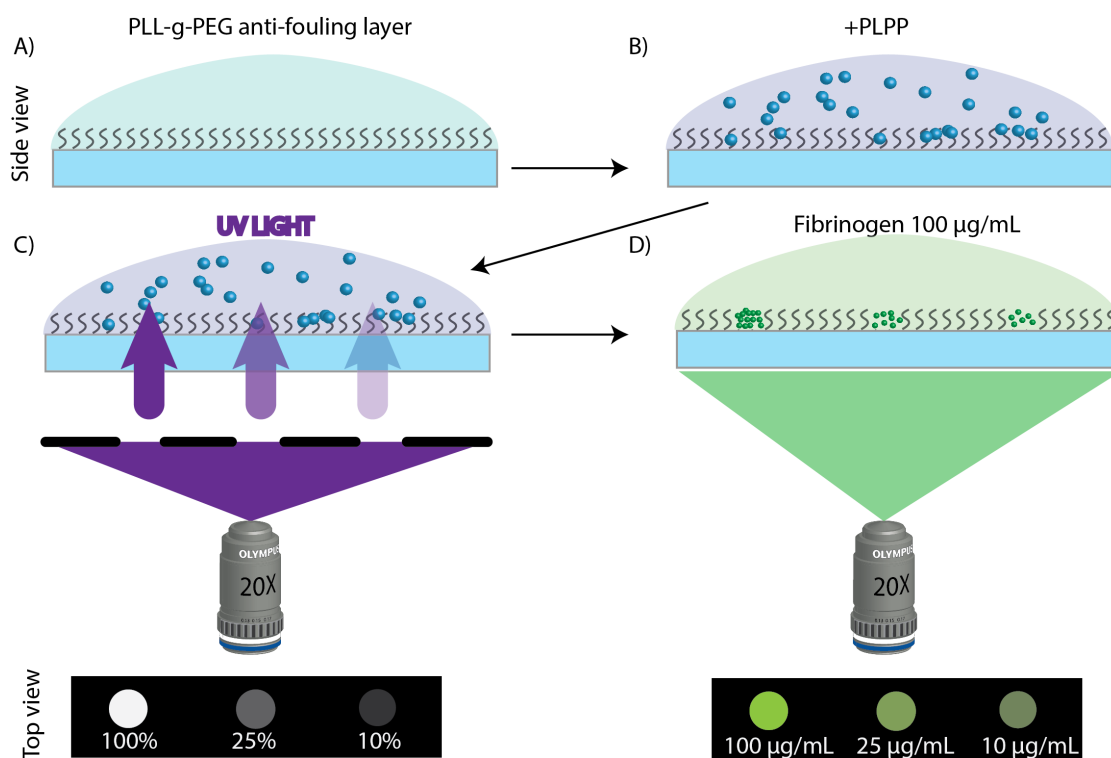


Figure 4.4: Micro-patterning with PRIMO on a glass coverslip. A) The glass substrate is plasma cleaned and uniformly coated by an anti-fouling layer of PLL-g-PEG. After 1 hour of incubation, the unbounded protein is washed out. B) Next, photo-activator PLPP is added to the well with the anti-fouling layer. C) The substrate with PLPP is exposed to UV light in the shape of our prepared grayscaled 8-bit masks. Pixels in white color (pixel value 255) correspond to 100% intensity of the laser, in black color (pixel value 0) equal to 0% laser intensity. D) Under the UV light of different intensity, we could control the concentration of the bounded protein to the exposed vacancies in the anti-fouling layer of PLL-g-PEG.

yellow-green, 505/515 nm, Thermo Fisher Scientific Inc.) and dilute it in 100 µL of 100 mM HEPES buffer, 10 µL of PLL-g-PEG (0.1 mg mL⁻¹ in PBS (PLL(20)-g[3.5]-PEG(2 kDa)), SuSoS AG) and fill with 878 µL of MQ (MilliQ, ultra-pure water) to 1 mL. This beads solution is then placed in an ultrasonic bath and for 1 hour regularly sonicated for 5 minutes every 20 minutes. Once the surface of the beads is passivated, we spin down the beads solution with a speed of 10.000 rcf (MiniSpin F-45-12-11, Eppendorf, Wesseling-Berzdorf, Germany) for 5 to 10 minutes until a pellet is formed. The supernatant is exchanged by fresh, clean HEPES and the beads dispersion is stored for a maximum of one week in the fridge. We use PLL-g-Peg coated beads to achieve an uniform layer without aggregations. An example of a distribution not suitable for TFM is shown in Fig. 4.5A, Fig. 4.5B shows an example of a suitable distribution of PLL-g-PEG beads in a gel. The distribution of the beads always needs to be checked before the experiments, and only gels with a uniform layer without

clusters are used.

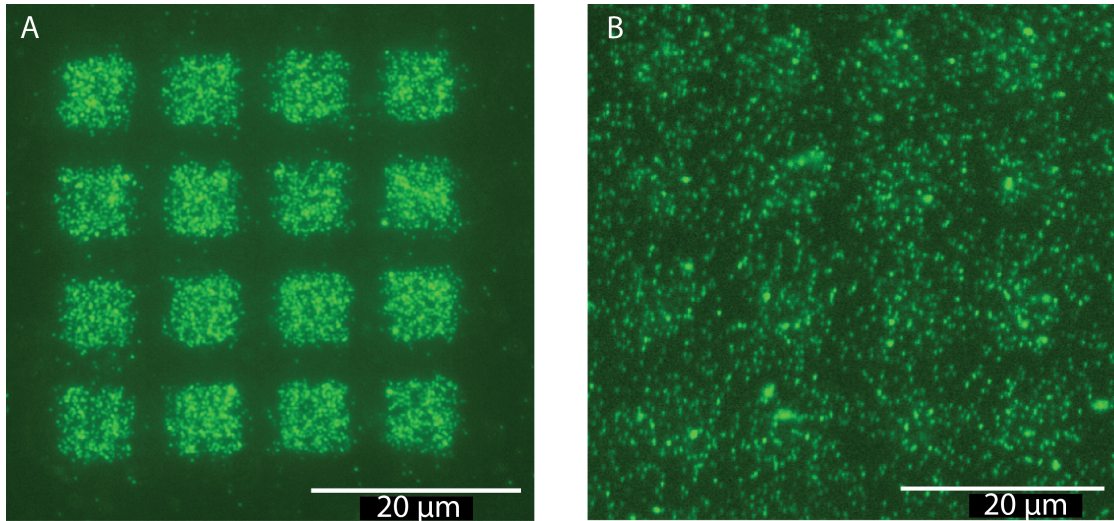


Figure 4.5: Effect of micro-patterning on the distribution of beads. A) A micro-patterned PAA gel with carboxylate-modified beads. B) A micro-patterned PAA gel with PLL-g-PEG beads.

To transfer the fibrinogen patterns from the glass coverslip to a PAA substrate, the PDMS stencil is removed and the glass coverslip is dried by blotting with tissues next to the pattern. A PAA mixture is prepared as described in previous Subsection 4.2.2 (with the difference that the fluorescent beads are passivated with PLL-g-PEG). We pipette 12 μL (note here, we use larger round cover slip due to the size of the holder for patterning) of the PAA mixture containing APS and TEMED on top of the circular patterned coverslip. The liquid is fast covered by the silanized coverslip. After 1 hour, the gel is soaked in PBS and the top glass with the pattern is gently removed. The surface of the gel now contains the fibrinogen pattern. We directly use the prepared gels for the TFM experiments to avoid any washing of the fibrinogen during prolonged storage. The process is depicted in Fig. 4.6.

4.2.4 Elasticity Measurements of PAA Gels

The stiffness measurement is critical in connection to the TFM experiment. The size of the displacement of the beads is dependent on the stiffness of the material and thus to obtain the right values of the forces, the stiffness has to be defined. A standard way to measure the stiffness of the PAA gel is shear rheometry (MCR501 Rheometer Anton Paar, Graz, Austria), which we also used as a common method in our previous studies [4, 67]. To confirm our results, we implement a measurement of local stiffnesses

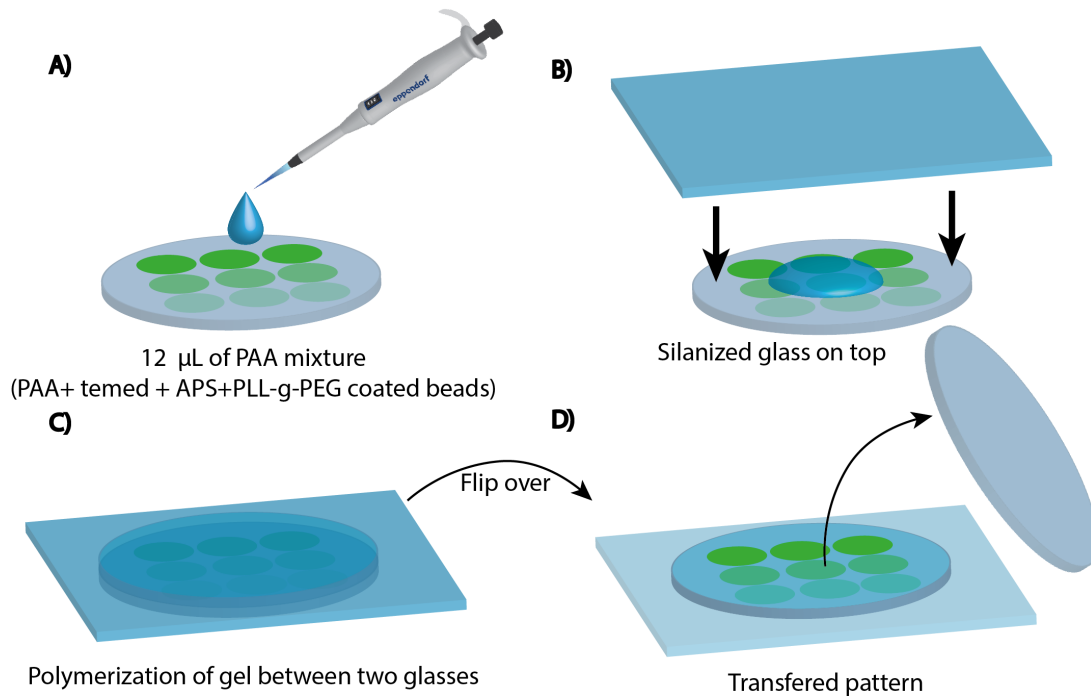


Figure 4.6: Schematic of the preparation of sandwich gels for experiments with different fibrinogen concentrations. A) A round patterned glass coverslip with 12 μL of unpolymerized PAA mixture. B) Adding the silanized bottom glass coverslip and forming a sandwich structure. C) Polymerization. D) Removing the round glass from the finished gel.

by nanoindenter (Chiaro Nanoindenter, Optics11, Amsterdam, Netherlands) and determine the minimum gel thickness [138]. For our experiments, we have chosen the stiffness 34 kPa corresponding to the stiffness of a healthy femoral artery tissues [139].

Shear Rheology

For the measurement with the rheometer, we use a cone plate of 25 mm in diameter and a cone angle of 2 degrees. We prepare a mixture of PAA with our required stiffness, and under the hood we add 0.5 μL of TEMED. To determine how long it takes to polymerize the gels and measure the stiffness, 5 μL of APS is added directly before measurement. For this size of the cone, a total 140 μL of the solution is suitable to start the measurement. The measurement is performed at RT and the gel is surrounded by wet tissues to keep a constant moisture. The measurement is performed with 1% strain which is applied for 15 s in 240 cycles. This way, we obtain a storage modulus G' and a loss modulus G'' , which together constitute the complex

modulus G :

$$G = \sqrt{(G')^2 + (G'')^2}. \quad (4.1)$$

The Young's modulus E is given by:

$$E = 2G \cdot (1 + \nu), \quad (4.2)$$

where $\nu = 0.5$ is the Poisson's ratio of the PAA gels [140]. Note here, that for previously measured values by A. Paknikar, $\nu = 0.3$ was used [4]. By recalculating the Young's modulus with the new Poisson's ratio, we obtain a stiffness of $E = 33.8 \pm 0.58$ kPa. This is in agreement with our measured values of 34 kPa as shown in Fig. 4.7.

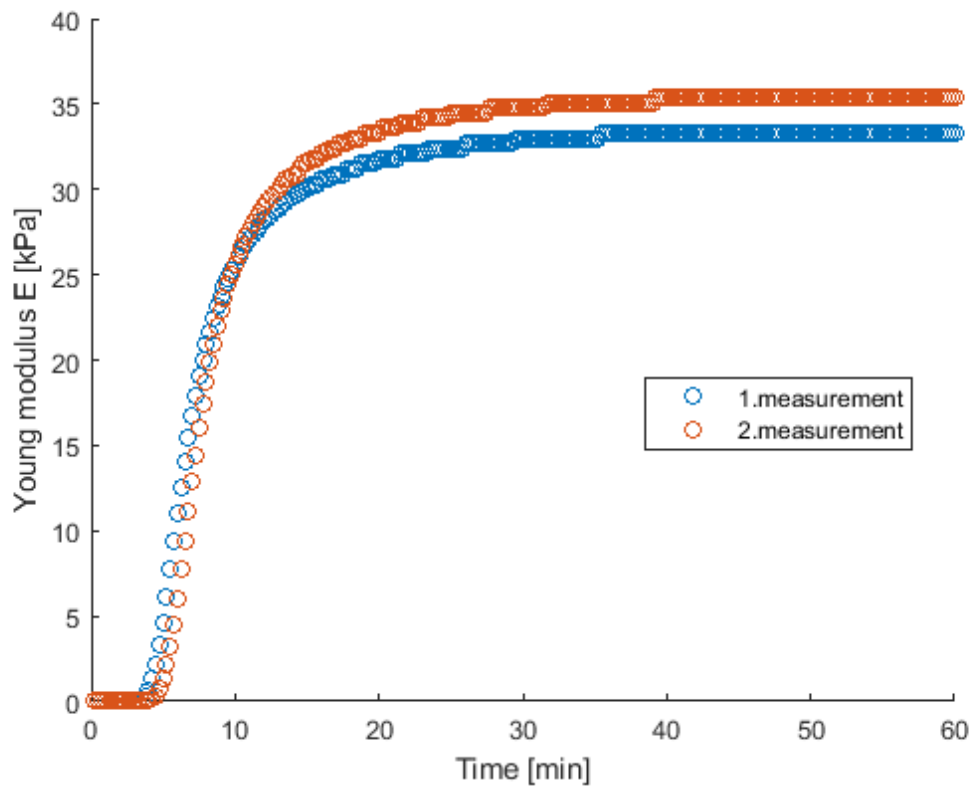


Figure 4.7: Shear rheology measurements for 34 kPa gels.

Nanoindenter Measurements

The nanoindenter Chiaro consists of a probe with a flexible cantilever of different stiffness with a spherical tip of various sizes for indenting. The cantilever is deflected by indenting the material. This deflection is measured with an interferometer and can thus be recalculated into the substrate's Young's modulus. The used probe has a cantilever stiffness of 0.440 N/m with a spherical tip of 50.5 μm radius. Each gel has been characterized at multiple spots of known thickness. The indentation has been provided by a time span of five seconds, consisting of two seconds load phase (setting with constant load 2 μN), one second hold phase and two seconds unload phase. Thus we obtain a load-displacement curve and in the linear regime for the first 30% of the curve we determine the final stiffness with a Herzian model [141]. In Fig. 4.8 we can see an example of such a result. The different thickness of gels is measured, and the minimum thickness of the gel is determined as 50 μm .

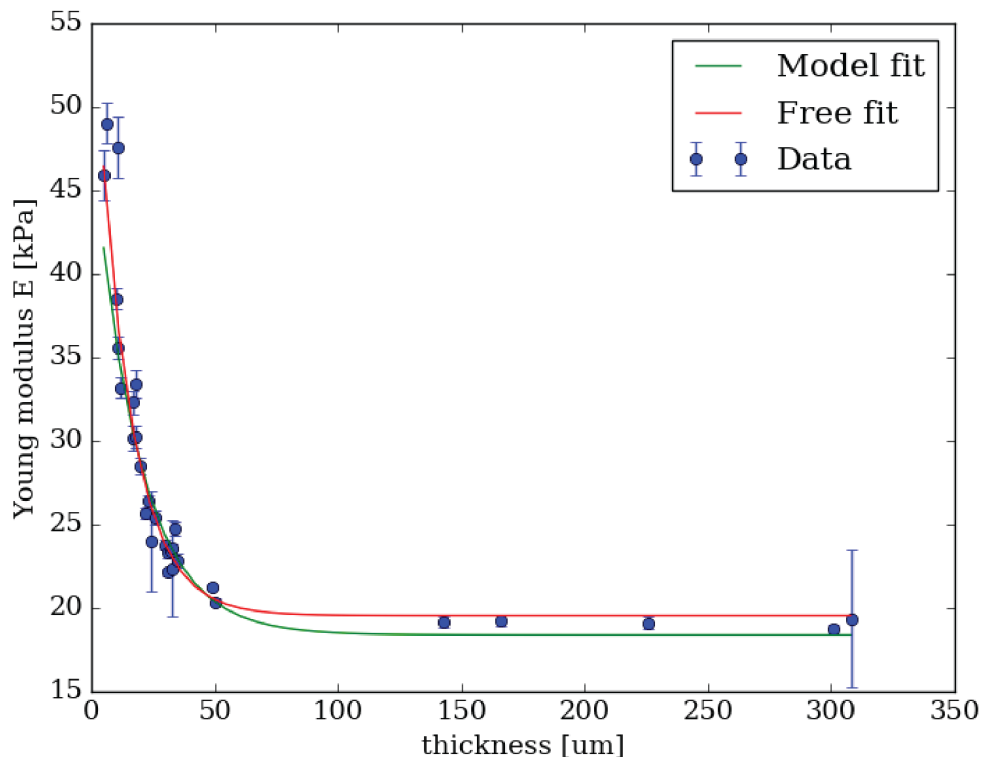


Figure 4.8: Young's modulus E of gel mixture with measured stiffness by shear rheology as 24.4 ± 0.6 kPa in relation to the thickness. Data were taken by S. Möhle and published in her bachelor thesis [138].

4.3 Microscopy

All TFM experiments, independent of the gel preparation procedure, are conducted on an inverted microscope (IX81, Olympus), equipped with a 60 \times water immersion objective (UPlanSApo, NA = 1.2, Olympus), a dual-band filter FITC/Cy5 (Fluorescein isothiocyanate/Cyanine 5 dye; excitation at 470 nm and 628 nm and emission at 537 nm and 694 nm (AHF Analysentechnik AG, Tübingen, Germany)) and a CMOS camera (Orca Flash 4.0 V2, quantum efficiency QE 82%, Hamamatsu Photonics Deutschland GmbH, Herrsching am Ammersee, Germany). The highly corrected water-immersion objective improves the image artifacts obtained by illumination through a thick layer of PAA gels. The refraction index of PAA gels is close to the water, and thus the usage of water immersion objective decreases spherical aberrations in comparison to oil immersion objectives [122]. Additionally, the highest available numerical aperture (NA) increases the signal-to-noise ratio of the recorded images. The CMOS camera, similarly like a CCD camera, converts light into electrons and further to the obtained charge of each pixel into voltage. The illumination set up was chosen to achieve a sufficient number of images per time and reduce the light exposure of our samples. The final axial resolution of the used set up is 0.1 μm \ px. Prepared PAA gels are washed with HT buffer containing BSA and placed inside an incubation chamber (Stage Top Incubator STX, Tokai Hit Co., Ltd., Fujinomiya, Shizuoka-ken, Japan), including a home-built sample holder optimized for 24 mm \times 24 mm coverslips. The incubation chamber guarantees stable physiological conditions of 5% CO₂ and 37°C throughout the experiment. All gels have a thickness of at least 50 μm and we select areas with homogeneous bead coverage for the experiments.

90 μL of SiR-actin stained platelet suspension are pipetted on the preheated PAA gel. 10 μL of thrombin solution (thrombin from human plasma activity 2800 U/mg (U denotes NIH-units here), Sigma-Aldrich; diluted in HT with BSA) is added directly before the recording starts to activate the platelets. The final thrombin concentration varies from 0.05 U/mL to 11.2 U/mL as shown in Table 4.2. The different fibrinogen coatings are investigated using a thrombin concentration of 0.1 U/mL. As soon as the platelets start spreading and adhering, we start to record the beads and actin structures simultaneously. The light intensity is set to 12 % of the lamp with 50 ms exposure time. We record the platelet spreading for 2 hours at one frame every 7.5 s. See schema of the experimental setup in Fig. 4.9.

Table 4.2: Thrombin concentrations

Final concentration in experiment	Volume of thrombin (280 U/mL) [μ L]	Volume of HT-BSA [μ L]	10X solution
0.05 U/mL	5	2795	0.5 U/mL
0.1 U/mL	10	2790	1 U/mL
0.5 U/mL	10	550	5 U/mL
1 U/mL	10	270	10 U/mL
5 U/mL	10	46	50 U/mL
11.2 U/mL	10	15	112 U/mL

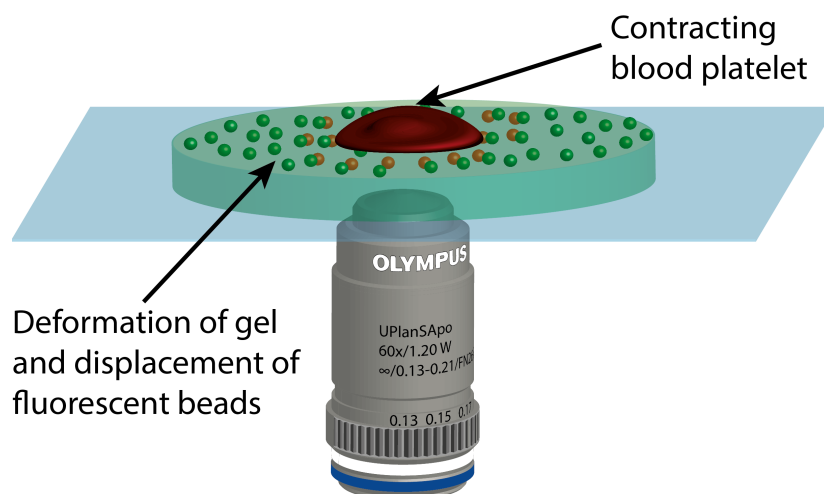


Figure 4.9: Sketch of a TFM experimental setup with spreading platelet. The platelet is spread on an elastic PAA substrate with fluorescent beads to visualize deformations.

Chapter 5

Data Analysis

The first part of this Chapter focuses in more detail on the TFM analysis, introduced in Chapter 3.3, and defines used parameters for force measurements with platelets. The second part of this Chapter describes the correlation of traction forces with the development of actin structures. For TFM analysis on platelets several different approaches have been published [2, 67] and for further analysis here we apply a method based on the optical flow algorithm. The analytical tool was contributed by Prof. Ulrich S. Schwarz, Dr. Dimitri Probst and Johannes Blumberg from the University of Heidelberg. Note that parts of this chapter are also briefly explained in Chapter 7 and are part of a prepared manuscript.

5.1 Calculation of Force with Optical Flow

The original videos were recorded with the microscopy setup described in Subsection 4.3. The videos are cropped into smaller regions, later known as initial cropped windows, which contain a single platelet with all its deformations. An example of the full field of view is provided in Fig. 5.1A. Only healthy-looking single platelets are analyzed with a minimum spreading time of 30 minutes. For a platelet to be defined as healthy-looking it has to deform the gel, such that there are visible contractions (Fig. 5.1C), form visible actin structures (Fig. 5.1B) and change its shape. Obvious clusters and fragments of platelets without contractions are neglected.

We start with a description of the software work flow with all important steps as shown in Fig. 5.2. A detailed explanation of regularization and the exact used algorithms are described in Ref. [4, 5] and briefly in Chapter 3.3. Here, we use the optical flow algorithm [142] with implemented pyramidal Kanade-Lucas-Tomasi

(KLT) feature tracker [143]. The analysis starts with a minimum of two images, down-sampled from 16 to 8 bit in ImageJ [144].

The KLT optical flow starts with a *Shi-Tomasi* corner detector to register the relevant parts of the image, in our case beads. The parameter is set to detect not more than 1000 beads, thus it provides an optimal balance between the amount of detected vectors and the computational capacity. To avoid double-counting of clusters, a minimum distance between beads is set to 3 pixels. The positions of beads are detected in the reference image first and then in the deformed image. The reference image represents the distribution of beads in the gel before placing the platelets on it. This is different to typical TFM analysis of larger cells where the reference image without contractions is obtained by trypsinization of the cells. The *pyramidal* KLT optical flow algorithm tracks in small search windows intensity gradients around the beads assuming that the intensity is constant between two successive images and that neighboring pixels have a similar motion. The selected search window has to be large enough so that it contains enough beads (minimum of 2-3), but it also has to be small enough so that the beads show a similar motion. This is a particular challenge for platelets, because the deformation they cause is large compared to their size. In addition, it means that the comparison of only two images before and after contraction is not sufficient and we have to analyze more time points in between. Thus a whole sequence of successive images is analyzed and the final displacement is determined as the sum of the small displacement steps. The size of the initial search window with our objective magnification and camera pixel size is $23 \mu\text{m}^2$ (width = 48 px) in the first run and is $5.8 \mu\text{m}^2$ (width = 24 px) in the second run of the *pyramidal* KLT. Subsequently, a drift correction is calculated in a region without deformation and is then subtracted from the bead displacement vectors. Therefore the final algorithm output is a discrete drift-corrected displacement field.

The drift-corrected displacement field is Fourier-transformed and converted to traction forces using regularized *Fourier Transform Traction Cytometry* or short FTTC [123]. The system uses Tikhonov regularization [123, 145] of 0th-order with regularization parameter λ defined by Generalized Cross-Validation (GCV) [146]. The program offers two options, the regularization parameter λ can be calculated for each converted traction force map individually or one value of λ can be applied for the whole sequence of images. To achieve a faster calculation, λ is calculated for several successive force maps and once the value stops to change, it is used for the whole sequence. The regularization parameter is located between $\lambda = 10^{-3}$ and $\lambda = 10^{-2}$ [5]. The regularization ensures to reduce artifacts during the FTTC analysis

due to errors in the displacement fields [147]. An important role in the calculation of the traction forces plays the defined stiffness of our used gels (here 34 kPa) and the Poisson's ratio (here $\nu = 0.5$ [140]). As part of post-processing, we apply a Tukey filter of $\alpha=0.2$ [148] to ensure that the obtained velocity field on the border of the initial cropped window is equal to zero. The total force F_{tot} exerted by the platelet is given by

$$F_{tot} = \int_{A_{roi}} |\vec{T}(\vec{x})| dA_{roi}, \quad (5.1)$$

where $\vec{T}(\vec{x})$ is the traction force at a given position \vec{x} , A_{roi} defines the selected area of the initial cropped window with a single contracting platelet.

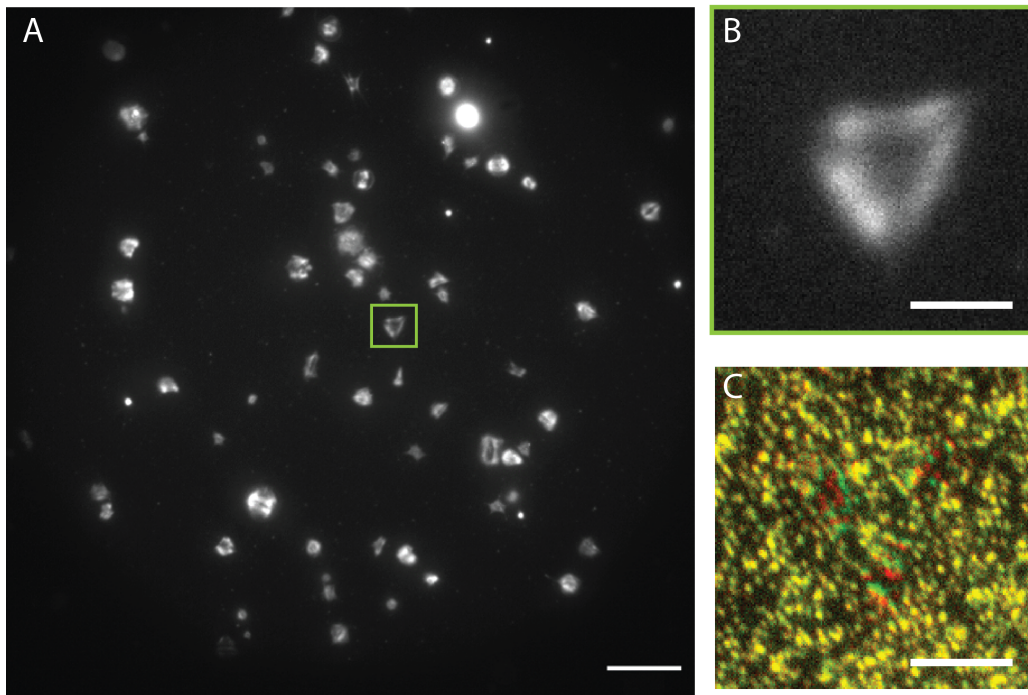


Figure 5.1: A) An example of the full field of view with a marked initial cropped window in a green square. Scale bar corresponds to 20 μm . B) The initial cropped window contains information about the actin structures and C) the contraction of beads visualized as a merged image of beads at $t = 0$ min and $t = 30$ min. Scale bars correspond to 5 μm .

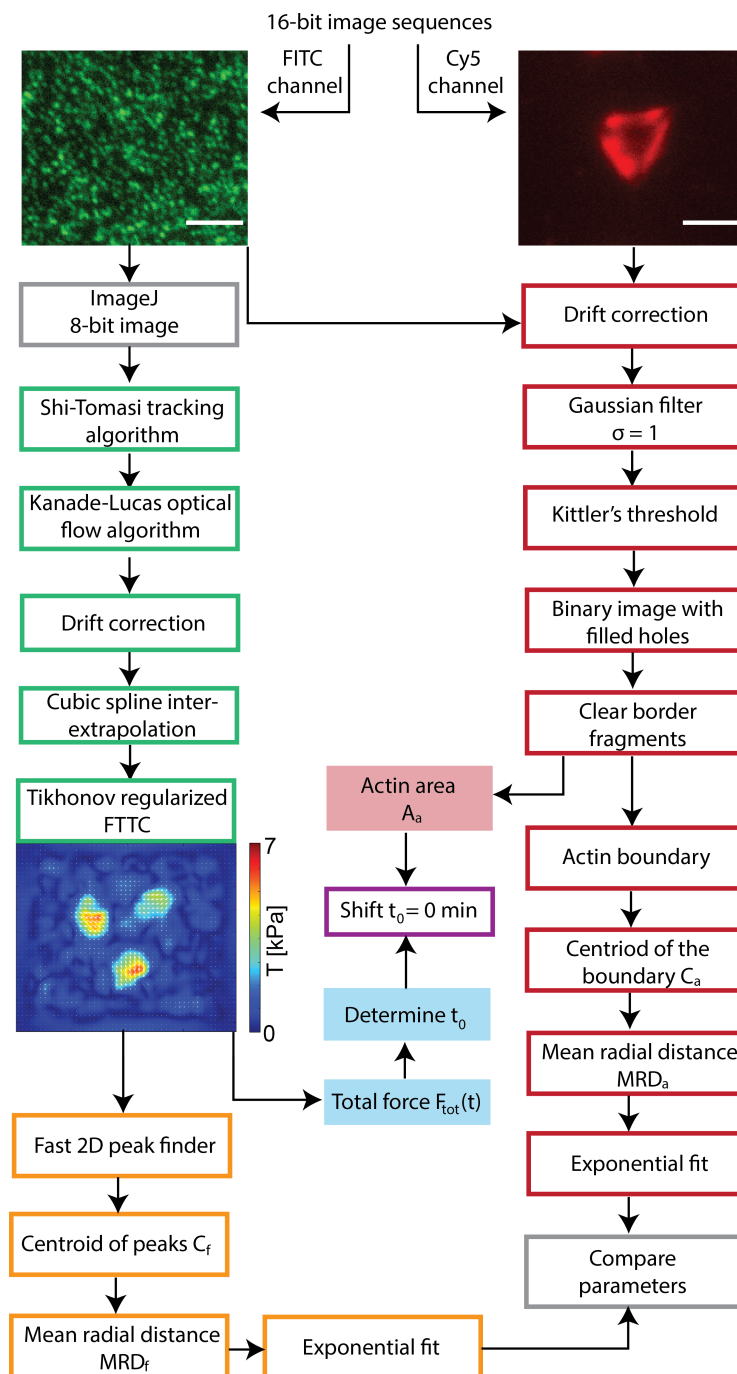


Figure 5.2: Schema of algorithms used for the traction force computation and the analysis of actin structures. The colors describe the classification of each step: green boxes show the individual steps in the algorithm for the regularization-based approach of TFM, red boxes show the actin area determination, yellow boxes show the process of analysing FTTC images obtained from the TFM analysis.

5.2 Determination of the Time Point of Force

The time-resolved total force $F_{tot}(t)$ provided by the TFM analysis (Subsection 5.1) at this stage has no clear defined time point $t_0 = 0$ min, which we need to compare the curves from different platelets. Based on the actin images only videos where platelets are clearly forming actin structures are selected for the TFM analysis. However, just from the formation of actin structures it is difficult to determine when the contraction is starting to take place. This is why we look into the $F_{tot}(t)$ in more detail to determine a common starting point for all experimental curves. Each $F_{tot}(t)$ is plotted such as we can detect a visible change in the slope of the increasing force using a second derivative test. The curve $F_{tot}(t)$ is smoothed by the *rloess* function in Matlab [149], which reduces the effect of outliers, and the second derivative $F''_{tot}(t)$ is calculated by the *gradient* function using a central difference approximation of the derivative. t_0 is defined as the time point of the first maximum of the second derivative of the smoothed $F_{tot}(t)$. An example of the determination is shown in Fig. 5.3.

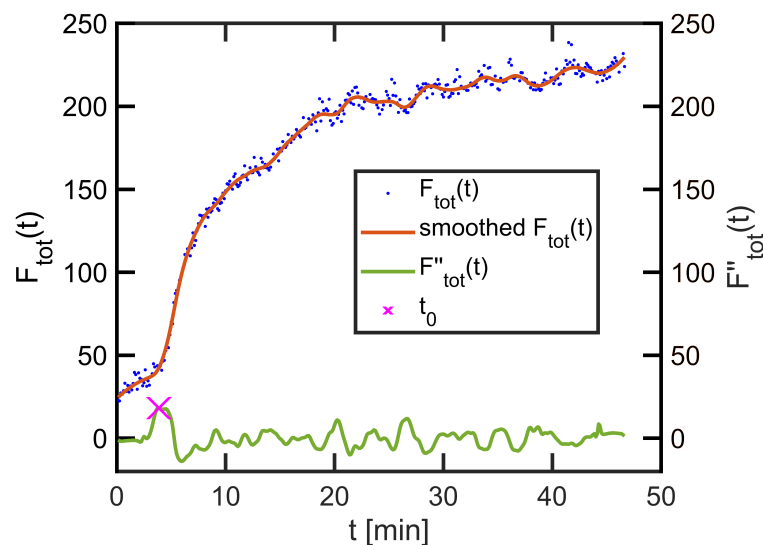


Figure 5.3: A graphical determination of $t_0 = 0$ min. The measured total force curve $F_{tot}(t)$ is shown as blue dots. The smoothed $F_{tot}(t)$ is shown as the red curve with its second derivation as a green curve. The $t_0 = 0$ min (magenta cross) is determined as the first maximum of the second derivation.

5.3 Determination of the Actin Boundary

In the following step, we determine the boundary of the actin structure and measure the area covered by actin A_a . The area determination is shown as part of the algorithm work flow in Fig. 5.2. A typical image sequence, containing a spreading single platelet, is shown in Fig. 5.4.

Before the boundary is determined, a spot is selected, where no cell is attached and the underlying beads in the gel are used to calculate the drift in the field of view. Thus the actin structures are drift corrected the same way as the beads in the TFM analysis. On the drift-corrected images of the actin structures our Matlab program applies a Gaussian filter with standard deviation $\sigma = 1$ to reduce noise by smoothing the gray values in the images. Next, we threshold the image following Kittler's method of minimum error thresholding [150]. The method performs well in cases where the distributions of the object and background have unequal variances. The result is used to create a binarized image with filled structures by the Matlab function *imfill*. The structure of interest is identified as the largest connected object by the Matlab function *bwareafilt*. The result is determined as the area covered by actin structures A_a and it is plotted in a time-resolved manner for all successive images. Subsequently, the Matlab function *bwperim* determines the boundary of the area covered by actin A_a and its centroid.

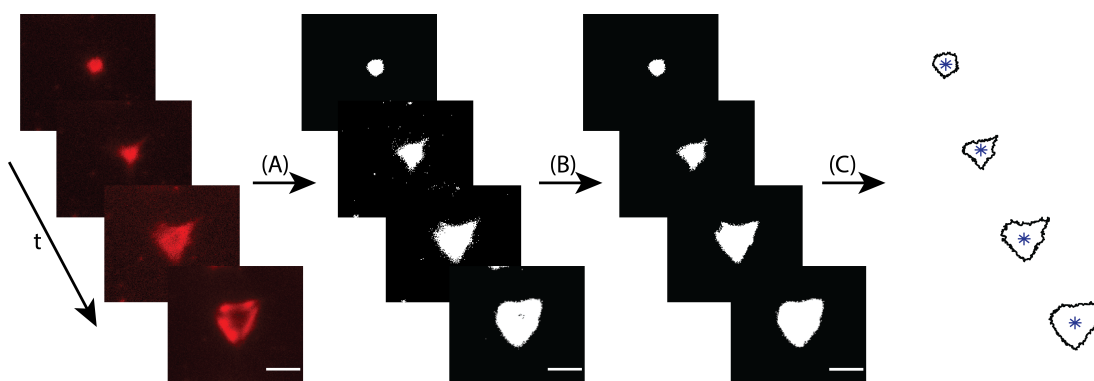


Figure 5.4: Sketch of the procedure used to determine the actin boundary. (A) From the actin structures we obtain binarized images by Kittler's thresholding. (B) Holes in the binarized images are filled and fragments are removed. (C) The boundary is detected and its centroid (blue star) is determined. The scale bar corresponds to $5 \mu\text{m}$ and refers to all sub-panels.

5.4 Determination of Force Hot Spots and Spatial Correlation with Actin Boundary

The force field takes on specific geometric patterns where the forces are typically concentrated at the edges of the cell in so-called hot spots [2]. These hot spots seem to be co-localized with the boundary of the actin area. To determine their spatial and temporal correlation in more detail, we establish an analysis based on a geometrical investigation.

From the previous Subsection 5.3 we determine the centroid of the actin boundary $C_a(x_{ca}, y_{ca})$ (see blue stars in Fig. 5.5A) at each time point. Additionally, we introduce a variable for the mean radial distance of the actin area MRD_a , defined as the average Euclidean distance between the centroid C_a and the actin boundary:

$$\text{MRD}_a = \frac{1}{K_a} \cdot \sum_{k=1}^{K_a} \sqrt{(x_{ca} - x_a(k))^2 + (y_{ca} - y_a(k))^2},$$

where K_a is the number of pixels on the actin boundary and (x_a, y_a) are the coordinates of the pixels.

To quantify the spatial and temporal correlation of the force fields and actin structures, we first determine the position of the force hot spots using the Matlab function *Fast 2D peak finder*[151]. Here, we focus on those peaks that exceed a level of 50% of the highest traction force at each time point as shown in Fig. 5.6. For each platelet, we determine the centroid of these peaks $C_f(x_{cf}, y_{cf})$ (see orange cross in Fig. 5.5B) and the mean radial distance of the force MRD_f , defined as the average Euclidean distance between the centroid C_f and the detected hot spots:

$$\text{MRD}_f = \frac{1}{K_f} \cdot \sum_{k=1}^{K_f} \sqrt{(x_{cf} - x_f(k))^2 + (y_{cf} - y_f(k))^2},$$

where K_f is the number of detected peaks and (x_f, y_f) are the coordinates of the detected peaks.

In Fig. 5.7 we present an example of the MRD_a and MRD_f of a typical platelet in a time-resolved manner. It is evident that both curves show a very similar exponential increase. We quantify this trend by fitting the curves with an exponential model:

$$\text{MRD}(t) = \text{MRD}_{max} \cdot [1 - B \cdot \exp(-(t + d)/\tau)],$$

where MRD_{max} is the maximum MRD_a or MRD_f , respectively, d is the time offset, and τ is the time constant.

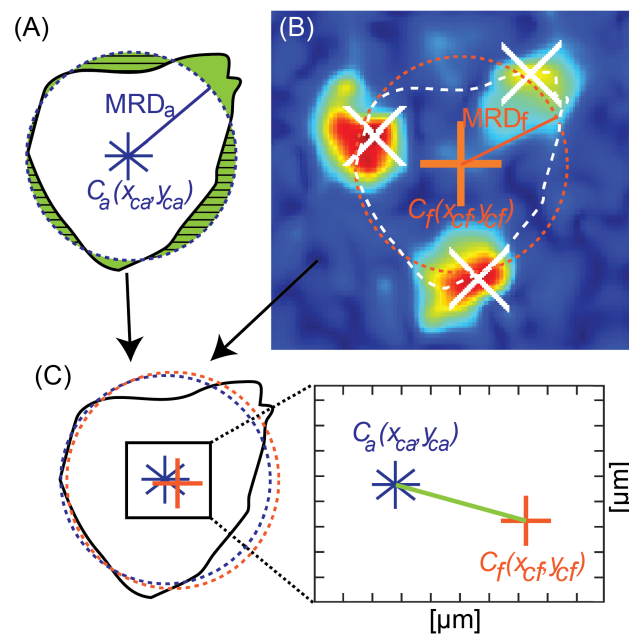


Figure 5.5: A determination of the distance between centroids, MRD_a and MRD_f . (A) First the boundary of the actin is detected with its centroid $C_a(x_{ca}, y_{ca})$ as a blue star. The mean radial distance of the actin MRD_a is shown as a blue dashed circle with a defined radius. The green area is equal to the green striped area. (B) The detected peaks are labeled as white crosses. The centroid of the hot spots $C_f(x_{cf}, y_{cf})$ is calculated and is represented as an orange cross. MRD_f is shown as an orange dashed circle with a defined radius. (C) An overlay of the actin boundary (black), MRD_a circle (dashed blue) and MRD_f circle (dashed orange). The distance between the centroids of the two circles is shown in the inset and is represented by the green line.

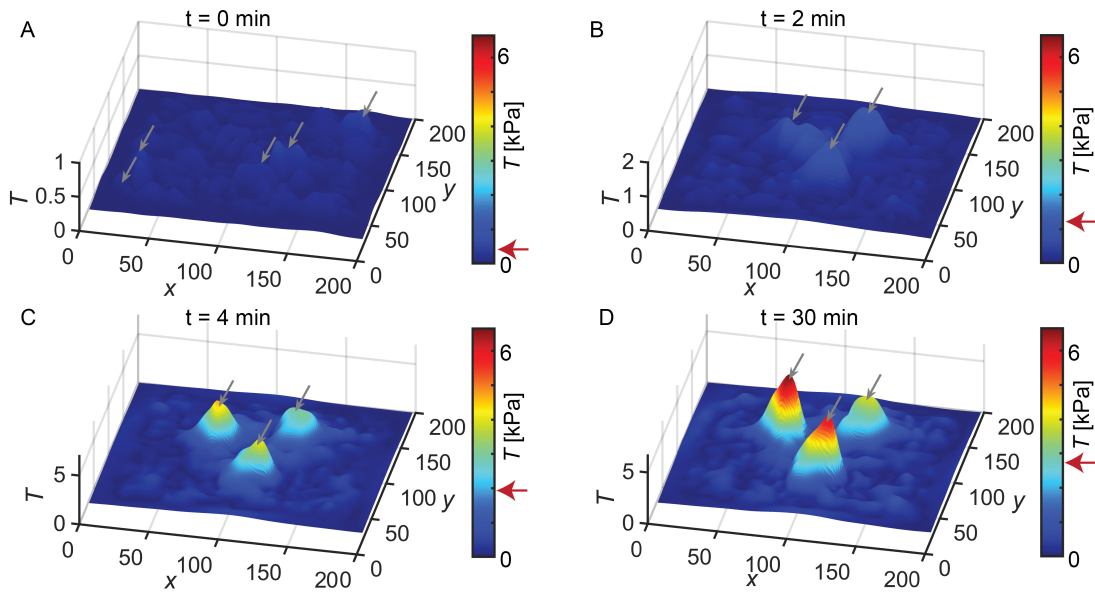


Figure 5.6: A determination of the force hot spots at A) $t = 0$ min, B) $t = 2$ min, C) $t = 4$ min and D) $t = 30$ min. Note that the z-scale of all sub-figures are scaled differently to observe the formed peaks, but the color scale is the same for all subfigures. The detected peaks are labeled by gray arrows. Red arrows indicate on the color scale the threshold, determined as 50% of the maximum force at the corresponding time point.

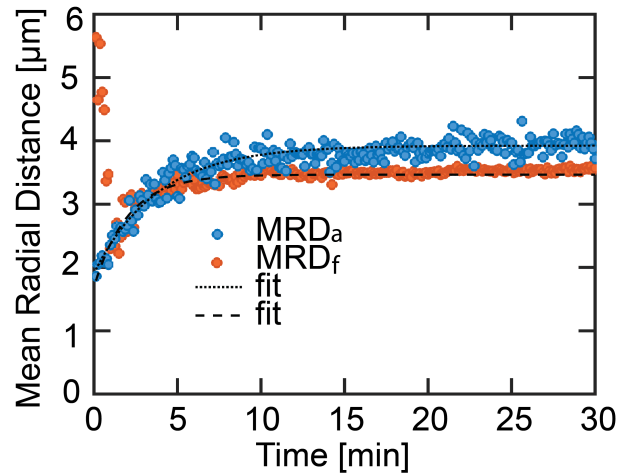
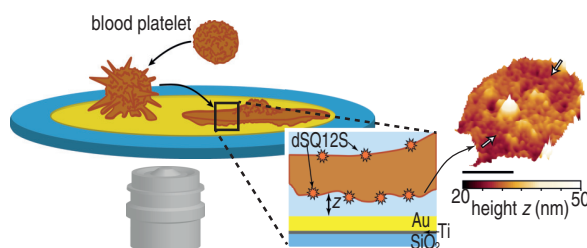


Figure 5.7: Temporal evolution of the MRD_a (blue) and MRD_f (orange) for the example platelet shown in Figs. 5.5 and 5.6 with marked exponential fits.

Chapter 6

Time-resolved MIET Measurements of Blood Platelet Spreading and Adhesion



This chapter is published as "Time-resolved MIET measurements of blood platelet spreading and adhesion" (Anna Zelená,^a Sebastian Isbaner,^b Daja Ruhlandt,^b Anna Chizhik,^b Chiara Cassini,^a Andrey S. Klymchenko,^c Jörg Enderlein,^b Alexey Chizhik^b and Sarah Köster^{*a,d,e}, *Nanoscale*, 2021, DOI:10.1039/D0NR05611A). Reproduced from Ref. [6] with permission from Royal Society of Chemistry.

S.K. and J.E. conceived and supervised the project; A.Z. and Anna Chizhik performed static experiments and A.Z. and S.I. performed the rapid experiments; A.S.K. provided the experimental membrane dye; D.J., S.I. and A.Z. analyzed the data; C.C. helped with statistical analysis; Alexey Chizhik contributed materials and analytical tools. All authors contributed to writing the manuscript and reviewed the paper.

^a Institute for X-Ray Physics, University of Göttingen, Friedrich-Hund-Platz 1, 37077 Göttingen, Germany. Fax: +49 (0)551 / 39 29430; Tel: +49 (0)551 / 39 29429; E-mail: sarah.koester@phys.uni-goettingen.de

^b Third Institute of Physics – Biophysics, University of Göttingen, Friedrich-Hund-Platz 1, 37077 Göttingen, Germany.

^c Laboratoire de Biophotonique et Pathologies, UMR 7021 CNRS, Université de Strasbourg, Faculté de Pharmacie, 74, Route du Rhin, Illkirch 67401 Cedex, France.

^d German Center for Cardiovascular Research (DZHK), partner site Göttingen, Germany.

^e Cluster of Excellence "Multiscale Bioimaging: from Molecular Machines to Networks of Excitable Cells" (MBExC), University of Goettingen, Germany.

6.1 Abstract

Human blood platelets are non-nucleated fragments of megacaryocytes and of high importance for early hemostasis. To form a blood clot, platelets adhere to the blood vessel wall, spread and attract other platelets. Despite the importance for biomedicine, the exact mechanism of platelet spreading and adhesion to surfaces remains elusive. Here, we employ metal-induced energy transfer (MIET) imaging with a leaflet-specific fluorescent membrane probe to quantitatively determine, with nanometer resolution and in a time-resolved manner, the height profile of the basal and the apical platelet membrane above a rigid substrate during platelet spreading. We observe areas, where the platelet membrane approaches the substrate particularly closely and these areas are stable on a time scale of minutes. Time-resolved MIET measurements reveal distinct behaviors of the outermost rim and the central part of the platelets, respectively. Our findings quantify platelet adhesion and spreading and improve our understanding of early steps in blood clotting. Furthermore, the results of this study demonstrate the potential of MIET for simultaneous imaging of two close-by membranes and thus three-dimensional reconstruction of the cell shape.

6.2 Introduction

Blood platelets are small, non-nucleated fragments of megakaryocytes, with a diameter between 2 and 5 μm in the resting state and play a crucial role in early steps of blood clotting [152]. During a blood vessel injury, platelets are stimulated by the presence of, *e.g.*, thrombin, adenosine diphosphate (ADP) or serotonin [153], which initiates a shape change in the cells from discoid to spherical, followed by the formation of extended filopodia which initiate the adhesion to a substrate [152–154]. The platelet membrane consists of a typical phospholipid bilayer [152], whose surface is covered with a particularly thick (15–20 nm) glycoprotein and glycolipid coat, known as glycocalyx, carrying negative charges. Thus, platelets repel other platelets and blood components [26]. Platelets do not divide and lack a microtubule spindle apparatus, however, they do possess an acto-myosin cytoskeleton which promotes adhesion, spreading and contraction [3, 30]. Once a platelet adheres to the substrate, it becomes very flat and its thickness in air-dried conditions reaches from 40 nm for the periphery to 100 nm for the cell center, as measured by scanning electron microscopy (SEM) [47]. Due to the flattening during platelet spreading, the cell's surface area increases drastically. The necessary additional area is created by

unfolding of wrinkled membrane that consists of numerous folds into the platelet interior and is known as the open canalicular system (OCS) [155, 156].

Changes in platelet shape during adhesion and spreading have been studied by various methods in order to understand cell-matrix interactions in more detail. Atomic force microscopy (AFM) [51], scanning ion-conductance microscopy (SICM) [53–56] or hopping probe ion conductance microscopy (HPICM) [57] provide a good picture of the shape of the apical membrane and confirm the involvement of the cytoskeleton. However, early stages of spreading are difficult to visualize with these methods as the scanning probe approaches the platelet very closely. Additionally, the basal membrane is typically not accessible. Conventional light microscopy techniques, including fluorescence wide-field and confocal laser scanning microscopy (CLSM), are diffraction limited and thus provide a restricted axial resolution of 1 μm or 500 nm, respectively [58–60]. Optical super-resolution methods like stimulated emission depletion (STED) microscopy overcome this limitation, and a combination of STED with 4Pi microscopy, known as isoSTED [62–64], leads to an improvement of the resolution down to < 21 nm in axial and 30 nm in lateral direction [65]. Thus, the thickness of hydrated, chemically fixed platelets was determined to be 90 nm at the periphery and about 320 nm in the center [66], showing that measurements on air-dried platelets underestimate the thickness of the cells [47]. The limitation of current isoSTED applications to platelets is that it cannot easily be used on living cells, and thus, dynamic measurements are difficult to realize.

Living platelets have been characterized by traction force microscopy (TFM) [2, 67, 68]. The heterogeneous force patterns, which dynamically change in time and display “hot spots” of high traction forces, give rise to the question of how the height profile of the membrane with respect to the substrate varies during adhesion and spreading. This question has been addressed using reflection interference contrast microscopy (RICM) on murine platelets [69]. The authors used a single monochromatic beam and were able to analyze the data in a semi-quantitative way and thereby distinguish between close contact areas with a distance of ~ 40 nm from the substrate, and areas with distances up to 110 nm [69].

Metal-induced energy transfer (MIET) imaging is a recently developed method that allows for measurements with nanometer axial resolution within a few hundreds of nanometers above a substrate [70, 71]. MIET is based on the modulation of the de-excitation rate of a luminescent molecule to the ground state by the near-field coupling to surface plasmons in a thin metal film deposited on the substrate surface [71]. Experimentally, this effect can be measured as a change of the emitter’s excited-state

lifetime by fluorescence lifetime imaging microscopy (FLIM), which can be directly converted into a distance value. MIET imaging has been applied to cell adhesion studies in the past, including comparatively thick kidney and lung cells, as well as the study of the epithelial-to-mesenchymal transition (EMT) [71, 72]. Dual-color MIET imaging was employed to demonstrate the extremely high resolution of the method by measuring the thickness of the nuclear envelope [73] as well as to determine the three-dimensional architecture of stress fibers of human mesenchymal stem cells [74]. In all previous cell studies using MIET, thick and slowly adhering cells were studied with the apical membrane located beyond the measurable range of a few hundreds of nanometers from the substrate, thus the focus was on the basal cell membrane. In a very recent study, single-color MIET was used to distinguish the two leaflets of a lipid bilayer spread on graphene and measure its thickness [116].

In the present work, we show that MIET imaging complements existing methods for the study of flat (parts of) cells, by visualizing two close-by membranes, *i.e.* the basal and the apical membrane, of living and highly dynamic platelets. Platelets are particularly thin and thus provide a perfect experimental system to benchmark the abilities of MIET in recording and analyzing data from both membranes simultaneously. We apply two modalities of MIET imaging. First, we characterize the three-dimensional profile of the basal and apical membranes of fully spread, unfixed platelets with nanometer accuracy in the axial direction. We find areas, where the platelet membrane approaches the substrate particularly closely. Second, we characterize the basal membrane-to-substrate distance of platelets while they spread, in a temporally resolved, quantitative manner using a rapid FLIM setup. These time-resolved data show an increased activity of the outermost rim of the platelets and this area stays further apart from the substrate than the inner area. Our results quantify platelet adhesion and spreading in a spatially and temporally resolved manner and thus help to better understand this crucial step in early hemostasis.

6.3 Experimental

Platelet Purification

Experiments were performed in accordance with the ethical vote of the Ethics Committee of University Medical Center Göttingen, votum 11/11/19. Each human donor had to fulfill specific criteria for medical application with negative history of anti-platelet treatment. The process of platelet purification was described previously

[67]. Briefly, 4 mL of platelet concentrate were mixed with prostaglandin E1 (PGE1 2.6 $\mu\text{g}/\text{mL}$, Cayman Chemical Company, Ann Harbor, MI, USA) and centrifuged for 20 min at $480 \times g$ and 21°C . The pellet was dissolved in PIPES saline glucose buffer (PSG: 5 mM PIPES, 145 mM NaCl, 5 mM glucose, 4 mM KCl, 1 mM MgCl_2 , 0.05 mM Na_2HPO_4 , pH 6.8) with PGE1. Note that PGE1 was used during purification to avoid premature platelet activation, but was washed out prior to the experiments. The process was repeated twice. After the third centrifugation, the pellet was re-suspended in HEPES-Tyrode buffer (HT: 134 mM NaCl, 12 mM NaHCO_3 , 2.9 mM KCl, 1 mM MgCl_2 , 5 mM HEPES, 5 mM glucose, 0.34 mM NaH_2PO_4 , pH 7.4) with bovine serum albumin (BSA, 5 mg/mL, Macs BSA stock solution, Milteny Biotech, Bergisch Gladbach, Germany). The final concentration of the purified platelets was measured in a hematocrit capillary.

Membrane Staining

The platelet membrane was fluorescently stained with dSQ12S [133]. Platelets were purified as described above and diluted to a final concentration of 2×10^7 cells/mL. For free space measurements on glass and rapid FLIM measurements on gold/titanium coated glass bottom Petri dishes (μ -Dish 35 mm diameter, high type, Ibidi GmbH, Martinsried, Germany), the platelets were stained with dSQ12S at a final concentration of 310 nM. The diluted platelets were mixed with the dye and incubated for 5 minutes at 37°C and 5% CO_2 . After the incubation, PGE1 was added at a concentration of 2.6 $\mu\text{g}/\text{mL}$ and the solution was centrifuged at $480 \times g$ for 5 min at 21°C to remove residual unbound dye. The supernatant was carefully removed with a pipette and the pellet was re-suspended in HT containing BSA. For static MIET experiments a lower concentration of dye was used (232.5 nM) and the centrifuging step was omitted. Labeled platelets were added to the Petri dish, activated by thrombin (human plasma thrombin, Sigma Aldrich, St. Louis, MO, USA; diluted in HT buffer with BSA to final concentration of 0.28 NIH units/mL).

MIET Imaging

Metal Deposition

A semitransparent metallic film consisting of a 15 nm gold film deposited on a 2 to 3 nm titanium film for better adhesion to glass was prepared by vapor deposition onto a cleaned substrate (thickness 170 μm , μ -Dish 35 mm diameter, high type, Ibidi

GmbH) using an electron beam source (Univex 350, Laybold, Cologne, Germany) under high-vacuum conditions ($\sim 10^{-4}$ Pa). During the vapor deposition, the film thickness was monitored using an oscillating quartz unit, and afterwards verified by AFM. Our experiments were performed on stiff glass surfaces, as MIET imaging is currently limited to such substrates. This circumstance does, however, not limit the comparability to literature data, since most previous experiments were also performed on stiff substrates. We did not use any additional coating of the substrate (for instance, with collagen) in order to prevent any variation of the cell membrane height because of the coating thickness variation.

MIET Imaging Setup

The static MIET measurements were carried out with a custom built confocal microscope equipped with a multichannel picosecond event timer (HydraHarp 400, PicoQuant GmbH, Berlin, Germany) allowing for fluorescence lifetime imaging. The system was equipped with a high numerical aperture objective (Apo N, 60 \times /1.49 N.A. oil immersion, Olympus, Hamburg, Germany) for both focusing excitation light and collecting fluorescence light. A white-light laser system (SC400-4-20, Fianium, Southampton, England) with an acousto-optical tunable filter (AOTFnc-400.650-TN, AA Optic, Orsay, France) served as the excitation source. The excitation light was reflected by a non-polarizing beam splitter towards the objective. Back-scattered excitation light was blocked with a long-pass filter (BLP01-635R, Semrock, Rochester, NY, USA). The collected fluorescence was focused onto the active area of an avalanche photo diode (PDM series, MPD, Bolzano, Italy). A pixel size of 100 nm was chosen with a pixel dwell time of 10 ms. Depending on the size of scanned area, a single scan took between 1.7 min and 3.4 min and was repeated three times. To ensure physiological conditions, the microscope was equipped with an incubation chamber and the cells were kept at 37°C.

Rapid FLIM Setup

Rapid fluorescence lifetime imaging was performed on a custom-built confocal setup. The sample was excited with a pulsed diode laser (LDH-640-, PicoQuant GmbH). The beam was coupled into a single-mode fiber (PMC-460Si-3,0-NA012-3APC-150-P and fiber coupler 60SMS-1-4-RGBV-11-47, both Schäfter + Kirchhoff GmbH, Hamburg, Germany). Behind the fiber, the beam was recollimated by an objective (UPlanSApo 10 \times 0.40 N.A., Olympus) and passed a clean-up filter (F94-640, AHE, Tübingen,

Germany). A 90/10 beam splitter was used to reflect the excitation light into the microscope and separate it from the emission light. The reflected beam was directed into a laser scanning system (FLIMbee, PicoQuant GmbH) and then into a custom sideport of the microscope (Olympus IX73). The three galvo mirrors in the scanning system were imaged onto the backfocal plane of the objective (UApo N 100 \times 1.49 N.A. oil, Olympus) with 180 mm and 90 mm achromatic lenses. The sample could be moved by a manual $x - y$ stage (Olympus). Fluorescence emitted by the sample was collected by the same objective. The fluorescence light that passed the 90/10 beam splitter was then focused onto a pinhole (100 μm , Thorlabs, Newton, NJ, USA) with an 180 mm achromatic lens. The light was collimated by a 100 mm lens and passed through a bandpass filter (F37-679, AHF, 679/41 BrightLine HC, Semrock) in front of a lens ($f = 30$ mm, Thorlabs) focusing the light onto the detector (τ -SPAD, PicoQuant GmbH). The signal of the photon detector was recorded by a TCSPC system (HydraHarp 400, PicoQuant GmbH). FLIM images were recorded with the SymPhoTime 64 software (PicoQuant GmbH), which controlled the TCSPC system and the laser scanner. A pixel size of 100 nm was chosen with a pixel dwell time of 20 μs and a TCSPC resolution of 16 ps. For a $10 \times 10 \mu\text{m}^2$ image, the scan speed was 3.3 fps. The rapid MIET data were partly recorded at 37°C and partly at room temperature, however, no difference in platelet behavior was observed.

Fluorescence Lifetime Data Evaluation

Both for rapid movies of adhering platelets and for single images of already spread platelets, fluorescence photons were detected in time-tagged, time-resolved (TTTR) mode. In TTTR mode, each photon carries two time tags, one with respect to the start of the experiment, which is counted as the number of preceding laser pulses, and a second with respect to the last laser pulse. Additionally, line change markers from the piezo driver are encoded in the raw data and are used for sorting the photons into individual pixels based on their arrival time in each line. In order to obtain higher photon numbers for images of spread cells, the same area of the sample was scanned several times. For each individual pixel, the arrival times of all recorded photons with respect to the last laser pulses were histogrammed (bin width 32 ns), yielding one time-correlated single-photon counting (TCSPC) curve per pixel. As described previously [157], measuring in TTTR mode at high count rates can introduce severe distortions of the TCSPC curves due to detector and electronics dead-time effects. We found the detector and electronics dead-times to be 74 ns and 80 ns, respectively,

and corrected the TCSPC curves as described in Ref. [157].

Since the vertical extension of the focus was on the order of a micrometer and we focused on the gold surface, fluorescence was collected simultaneously from the apical and basal cell membrane as shown in Fig. 6.1a. Assuming that the instrument response function (IRF) is given by $\text{IRF}(t)$, for each pixel (x, y) the measured signal $I(t|x, y)$ follows a Poisson distribution with expectation value

$$f_{\text{full}}(t|x, y) = \text{IRF}(t) \star \left[a(x, y) \cdot e^{-t/\tau_1(x, y)} + b(x, y) \cdot e^{-t/\tau_2(x, y)} \right] + c(x, y), \quad (6.1)$$

where \star denotes convolution and both the lifetimes $\tau_{1,2}$ and the amplitudes a, b, c are unknown. However, the convolution with the IRF only influences the result close to the position t_{max} of the peak. One can avoid the need of determining the IRF by performing a tail fit instead, where only the signal after a certain cutoff time after the peak, $t \geq t_{\text{max}} + t_{\text{cutoff}}$, is fitted with

$$f_{\text{tail}}(t|x, y) = \tilde{a}(x, y) \cdot e^{-t/\tau_1(x, y)} + \tilde{b}(x, y) \cdot e^{-t/\tau_2(x, y)} + \tilde{c}(x, y). \quad (6.2)$$

We typically used a cutoff time of $t_{\text{cutoff}} = 0.3$ ns. The IRF and the cutoff are shown in Fig. 6.4. The fit itself employs a Nelder-Mead downhill simplex method [158] to minimize the negative log-likelihood

$$\sum_t -I(t|x, y) \cdot \log [f_{\text{tail}}(t|x, y)] + f_{\text{tail}}(t|x, y) \quad (6.3)$$

for each pixel individually. To avoid large fitting errors at low photon numbers, only pixels with at least 3000 photons were evaluated, a number that was always reached within cells. The thus-acquired lifetime maps $\tau_1(x, y)$ and $\tau_2(x, y)$ are called *short lifetimes* and *long lifetimes* in the following.

Converting Lifetimes to Height Values

The theory behind MIET and how to calculate the lifetime-versus-height curve has been described in detail in a number of publications, such as Refs. [111] and [159]. Briefly, for a fluorophore positioned at height z above the substrate and with its emission dipole moment oriented at an angle θ with respect to the surface normal

(i.e. the optical axis in our setup), the fluorescence lifetime $\tau(z, \theta)$ is given by:

$$\frac{\tau(z, \theta)}{\tau_0} = \frac{1}{1 - \Phi + \Phi \cdot [S_{\perp}(z) \cos^2 \theta + S_{\parallel}(z) \sin^2 \theta] / S_0}. \quad (6.4)$$

Here, the *free-space lifetime* τ_0 is the fluorescence lifetime under identical conditions but in the absence of any metal structures. Similarly, Φ is the *free-space quantum yield* and S_0 is the total amount of energy emitted by the fluorophore per time in free space. When immersed in a medium with refractive index n and assuming a dipole moment p , classical electrodynamics yields $S_0 = cnk^4 p^2 / 3$, where c is the speed of light and k is the wave vector in vacuum. The total amount of energy emitted per time in the presence of a metal structure depends both on the position and orientation of the fluorophore. A calculation for dipoles oriented in parallel (S_{\parallel}) or perpendicularly (S_{\perp}) to a planar substrate can be found in Ref. [111]. The dye dSQ12S employed in this study has been shown to incorporate in parallel to the cell membrane due to its two amphiphilic anchor groups [133]. Since the cell membrane is for the most part (almost) parallel to the substrate, we set $\theta = \pi/2$ in all our calculations.

The free-space lifetime was obtained by measuring labeled cells seeded on untreated Petri dishes, yielding a value of $\tau_0 = (2.6 \pm 0.1)$ ns. The quantum yield of dSQ12S was measured in dimethyl sulfoxide (DMSO) using a nanocavity [70], yielding $\Phi_{\text{DMSO}} = 0.44$ and $\tau_{\text{DMSO}} = 1.3$ ns. As described in Ref. [73], the quantum yield value obtained in one medium can be converted to the value in a second medium provided the refractive indices of both media are known and the fluorescence lifetime has also been measured in both media. Then,

$$\Phi_{\text{cell}} = \Phi_{\text{DMSO}} \cdot \frac{\tau_{\text{cell}}}{\tau_{\text{DMSO}}} \cdot \frac{n_{\text{cell}}^5}{n_{\text{DMSO}}^5} \cdot \frac{(2n_{\text{DMSO}}^2 + 1)^2}{(2n_{\text{cell}}^2 + 1)^2}. \quad (6.5)$$

Using this formula, $n_{\text{DMSO}} = 1.47$, $n_{\text{cell}} = 1.33$ and the free space lifetime $\tau_{\text{cell}} = \tau_0 = 2.6$ ns, we found $\Phi_{\text{cell}} = 0.74$. The resulting MIET lifetime-versus-height calibration curve is shown in Fig. 6.2b. The curve was calculated based on the exact parameters for the metal layers for every sample.

Rapid MIET Data Analysis.

The rapid MIET data were acquired in TTTR mode as mentioned above. Because of the higher frame rate, the number of photons in a single pixel of a single frame is insufficient for reliable bi-exponential fitting. We therefore employed spatial and

temporal binning to obtain a higher number of photons per fit.

First, temporal binning of 15 frames was performed to obtain intensity images of each dynamic platelet. These images were used for intensity thresholding of a region of interest that contained the platelet only. A morphological erosion with a disk of radius of 500 nm as a structuring element was used to separate the rim of the platelet from the inner part. With a second threshold, the high intensity region containing residual membrane and organelles in the center of the platelet was excluded (see Fig. 6.3e for an example). Note that for the early time points of spreading, the intensity throughout the whole cell was similar and the cell was analyzed as a whole. By contrast, for later times points, differences between the major part of the cell and a high intensity region in the center led to artifacts. Thresholding alone produces holes in the ROIs due to noise and non-uniform brightness of the data. We used Gaussian smoothing before and morphological closing operations after the thresholding steps to obtain ROIs without holes. The first threshold value was determined by a parameter that was scaled by the maximum intensity value in the image. The parameter for the second threshold value was scaled proportionally to the maximum intensity and inversely proportional to the area of the platelet. These parameters were chosen manually for each platelet and were then kept constant for all images of the respective recording. This approach allowed for a semi-automated, reproducible separation of the three areas.

TCSPC curves of all pixels in the ROIs were then summed, corrected for dead-time [157], and fitted with a bi-exponential model as in eq. (1). In contrast to the fitting of the static images, this included the IRF to maximize the number of photons used for the fit. A linear shift of the IRF was included as an additional fit parameter which takes into account the count rate dependent shape of the IRF of our detector. From this fit, the short lifetime was converted into a height using the MIET curve as explained before. The temporal evolution of the height was fitted with an exponential model of the form $h(t) = h_{\text{ad}} \exp\{-t/\tau_{\text{ad}}\} + h_f$ where τ_{ad} is the adhesion time, $h_{\text{ad}} + h_f$ the initial height of the platelet at $t = 0$, and h_f is the final height of the platelet after spreading. Because the number of photons of each lifetime fit is different due to the spreading, bleaching, and occasional refocusing, we took the different errors into account by using a weighted fit. The square root of the number of photons was chosen as the weight of each data point which is a first order approximation of the error of the lifetime fitting and height conversion. The temporal evolution of the area was fitted with an exponential grow model of the form $a(t) = a_f - a_{\text{sp}} \exp\{-t/\tau_{\text{sp}}\}$ where τ_{sp} is the spreading time, $a_f - a_{\text{sp}}$ is the initial area of the platelet at $t = 0$, and

a_f is the final area of the platelet after spreading.

6.4 Results and Discussion

Cell adhesion is governed by dynamic changes in membrane height above the substrate as a function of the lateral dimensions. MIET imaging has been shown to be an excellent tool for investigating biomolecular objects close to surfaces and in particular for studying adherent cells [71, 72, 74]. Most cells are, however, too thick for MIET to detect both the basal and the apical membrane and the investigations are restricted to the basal membrane. Blood platelets are an exception to this rule as they are only a few tens of nanometers thick when fully spread. We thus apply MIET imaging to platelets to investigate the spreading process in detail and in a time-resolved manner and to benchmark MIET imaging as a method to distinguish membranes in close proximity. Our method may also be applicable to thin parts of other cells, such as lamellipodia, axons of neurons, or pili of bacteria.

3D Reconstruction of the Platelet Membranes

To investigate the exact height of the platelet membrane with respect to the substrate, and thereby gain information about its 3D profile, we perform static MIET imaging experiments. As the cell membrane is a lipid bilayer with a thickness of a few nanometers, we label specifically one membrane leaflet. For this purpose, we employ the previously developed membrane probe dSQ12S, designed to stain the outer membrane leaflet [133]. Platelets labeled with dSQ12S are exposed to the substrate and activated by the addition of thrombin. As a consequence, they adhere and spread. After an incubation time of at least 10 min, FLIM images are recorded, thus characterizing the fully spread state of the platelets. The method provides nanometer resolution in the axial direction and a diffraction limited lateral resolution. As platelets are thinner than other cell types [65, 66], in addition to the signal stemming from the dSQ12S probe in the basal membrane, we detect signal emitted by the probe in the apical membrane when recording the fluorescence lifetime. The situation is sketched in Fig. 6.1a: a platelet with a fluorescently labeled membrane spreads inside a glass bottom Petri dish that is coated with 2 nm of titanium and 15 nm of gold. The presence of the gold layer is crucial for MIET imaging, as it modulates the lifetime of the excited state of the fluorophores *via* an energy transfer from the fluorophore to the metal film [111]. For each platelet, three subsequent images are recorded to

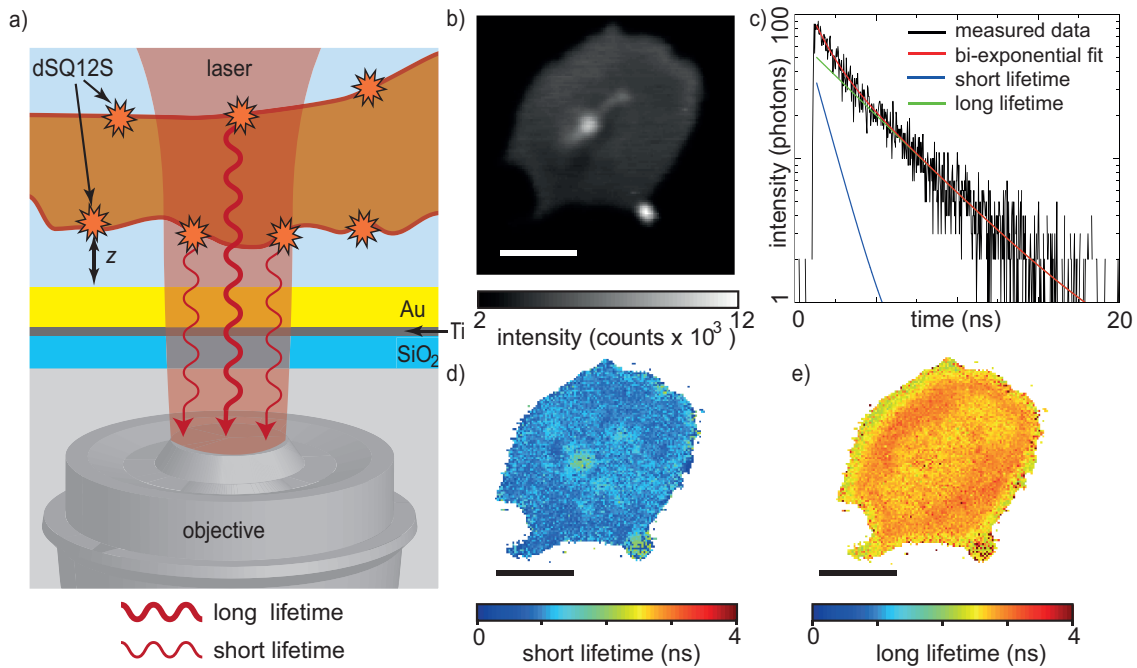


Figure 6.1: Schematic representation of a blood platelet membrane labeled with the fluorescent dye dSQ12S. Light from the basal membrane has a shorter lifetime than light from the apical membrane, because of its close proximity to the gold surface. (b) Fluorescence intensity image of an individual blood platelet taken with the laser focused on the gold surface. (c) Typical TCSPC histogram of a single pixel. The signal from a single pixel shows a complex decay curve (black), which is bi-exponentially fitted (red) to obtain the fluorescence lifetimes for the short (blue) and the long (green) components. (d) Values for the short lifetimes, corresponding to the basal membrane, plotted in a spatially resolved manner. (e) Plot of the long lifetime values, corresponding to the apical membrane. Scale bars correspond to $3 \mu\text{m}$.

increase the total number of detected photons. Additionally, the three individual scans are compared to make sure that the platelet spread area is in steady state and does not considerably change anymore, see Fig. 6.5.

The fluorescence intensity images of all three scans are added up as shown in Fig. 6.1b and provide information about the size of the platelet and its location in the field of view, whereas the FLIM data recorded simultaneously provide time correlated single photon counting (TCSPC) histograms, as shown in Fig. 6.1c, black line, for one typical pixel. TCSPC histograms contain the arrival times of all emitted photons with respect to the incident laser pulse. As mentioned above, in our case, the collected photons stem from both the basal and the apical membrane. We therefore use a bi-exponential decay model to fit the TCSPC histogram, as indicated by the red line in Fig. 6.1c. From these bi-exponential fits, we obtain both a short lifetime (blue line in Fig. 6.1c), and a long lifetime (green line) for each individual pixel and present the

results as spatial maps in Fig. 6.1d and e, respectively, or as histograms in Fig. 6.2a.

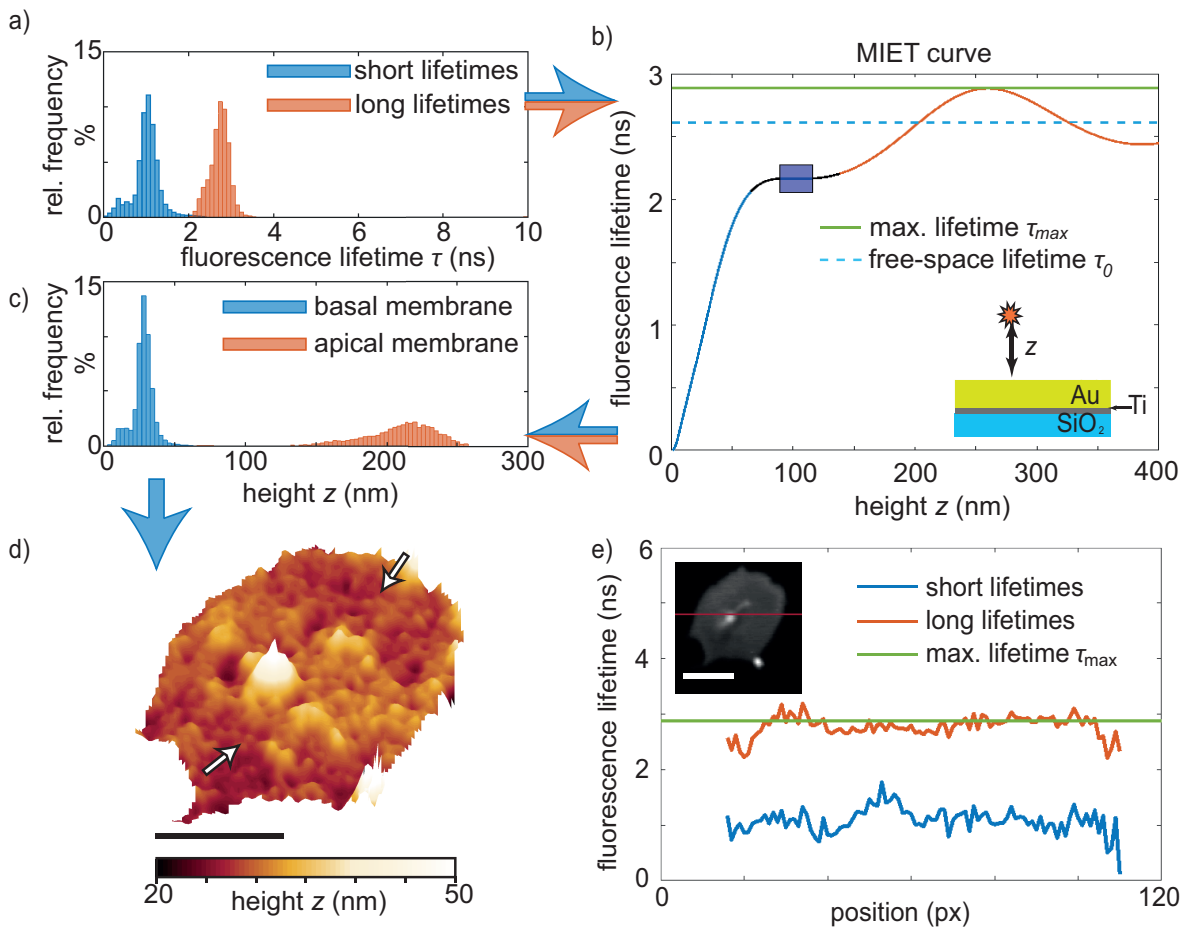


Figure 6.2: (a) Histograms of the collected short (blue) and long (red) lifetimes. (b) MIET calibration curve for dSQ12S with the maximum lifetime marked by the green solid line and the free space lifetime by the blue dashed line. The height z is measured from the gold surface to the labeled membrane. The blue rectangle marks a part of the curve with a slope of 0 for $89 \text{ nm} \leq z \leq 116 \text{ nm}$. The red part of the MIET curve corresponds to values used for the apical membrane. The blue part corresponds to the basal membrane. The black part of the curve denotes lifetime values not found in our data. (c) Height histogram for the basal (blue) and the apical (red) membrane after conversion using the MIET calibration curve. (d) Three-dimensional height profile of the basal membrane with examples of areas of lower surface-to-membrane distances marked by white arrows. We applied a Gaussian filter (kernel width $\sigma = 1$) to the data to reduce image noise. Note that for better visualization, the axial and lateral dimensions are shown on different scales. (e) Cross-sectional line plot through the blood platelet (inset) showing the short and the long lifetime information. Scale bars correspond to $3 \mu\text{m}$.

By taking into account all basic parameters of the sample, such as refractive index of the buffer, thickness of the metal film and emission spectrum of the dye molecules, we calculate the relation between the fluorescence lifetime of the molecules and their

height above the metal film [112]. This so-called MIET calibration curve is shown in Fig. 6.2b. It rises monotonously for the first ~ 250 nm, reaching a maximum at $z_{\max} = 257$ nm and $\tau_{\max} = 2.88$ ns. The first minimum after the peak is located at $z_{\min} = 384$ nm and $\tau_{\min} = 2.44$ ns. There is a region with zero slope in the curve between $89 \text{ nm} \leq z \leq 116 \text{ nm}$ marked by the blue rectangle, which in principle leads to an ambiguity of assignment between measured lifetime values and inferred height values. However, we find that almost no pixels exhibit lifetime values in this range. The MIET setup, including a high NA objective we use here is sensitive up to 400 nm above the surface and photons from higher values are not detected. We can therefore rule out any further minima in fluorescence lifetime.

With this curve, we convert our recorded lifetimes to height values for both the basal and the apical membrane and plot the results as histograms in Fig. 6.2c. For the short lifetimes $\tau_1(x, y)$, this conversion is straightforward as the data lie in the monotonically rising section of the MIET calibration curve, see histogram in Fig. 6.2c, blue. The resulting map for the example platelet shown in Fig. 6.1 is shown in Fig. 6.2d. Fig. 6.6 shows additional examples of individual platelets. Fig. 6.7 shows histograms of the distances of the basal membrane to the gold surface for each of the six platelets we analyzed and when averaged, it corresponds to 34 ± 4 nm. These results are in agreement with those reported by RICM on murine platelets. The authors observed close contact areas of ~ 40 nm above the surface [69]. With the assumption that the absence of fibrinogen coating in our case decreases the final height by about 5-8 nm [69, 160], our quantitative values confirm the earlier study with high precision. Interestingly, the basal membrane shows areas with a lower membrane-to-substrate distance, as indicated by the white arrows in Fig. 6.2d. These areas can be better visualized by masking out the heights in the upper tercile of the height distribution of the basal membrane, as detailed in Figs. 6.6 and 6.8. For the six platelets considered here, the average height of the first and second tercile is 29 ± 1 nm; the average height of the upper tercile is 43 ± 1 nm. Although it is unclear if such a modulation in height of the basal membrane would also occur in platelets spreading on soft substrates, there may be an analogy to TFM data on platelets that revealed hot spots of increased force in certain distinct positions of the platelet adhesion area [2]. These force hot spots and the areas of closer substrate adhesion may be related or co-localized, indicated by their stability in time.

For the long lifetimes $\tau_2(x, y)$, we follow a two-step approach for obtaining a complete height profile map. First, looking at the MIET data, we realize that for some pixels we obtain lifetimes that are longer than τ_{\max} . This observation becomes obvious in

the cross-section shown in Fig. 6.2e, red line, and can be explained by the uncertainty associated with fitting lifetime data from TCSPC curves. Indeed, the shape of the MIET calibration curve does not allow for directly determining the height values for lifetimes higher than $\tau_{\min} = 2.44$ ns. The reason is the maximum at z_{\max} with a decaying curve for higher z -values and the corresponding ambiguity, *i.e.* two possible height values for one measured lifetime value. As mentioned above, photons from above 400 nm do not get detected by our MIET setup. Second, we set our results in relation to literature data. If we assume the lower of the two height values, $< z_{\max}$, to be true, the mean height of the analyzable pixels of the apical membrane is 209 nm, as shown in the histogram in Fig. 6.2c, red. The lifetimes corresponding to the apical membrane increase from the rim to the center and show a “dip” in the center of the cell, as demonstrated in the long lifetime plot in Fig. 6.1e and in the cross-section in Fig. 6.2e (red). Assuming the lower of the two possible heights, this dip would directly transfer to a decreased platelet height in the center of the cell, which is in contradiction to published data, in particular SEM, AFM and SICM results [51, 53, 57, 152] that by contrast show an *increased* height of the apical membrane in the center of the platelet. We can therefore safely assume that the real height values in the cell center lie all the way to the right of the MIET calibration curve, *i.e.* right of the maximum τ_{\max} . The fact that the lifetime values in the center of the cell are never lower than τ_{\min} supports this hypothesis. According to this line of arguments, in the example shown in Fig. 6.1 and Fig. 6.2, where the central region of the apical membrane reaches a mean lifetime of 2.76 ± 0.04 ns we obtain a height of ~ 298 nm. Subtracting the height of the lower membrane (30 nm in this example), we obtain a thickness at the cell center of ~ 268 nm. This is in agreement with results from isoSTED measurements, where similar blood platelet thicknesses were found [65, 66], however, our data are taken on unfixed, living platelets. A detailed knowledge of the thickness and 3D shape of cells is very helpful, *e.g.*, when studying them in (micro)flow conditions or for understanding platelet-platelet interactions.

Rapid MIET Imaging

Platelets are extremely dynamic cells and spread within a few minutes [2, 3, 67, 69, 161]. Thus, we apply a fast scanning MIET mode to follow the spreading process in a time-resolved manner. This approach allows us to investigate the dynamic process with a temporal resolution of 3.3 fps, which we decrease by binning to 0.2 fps (4.5 s per frame). Thus, we obtain a good compromise between the spreading speed of the

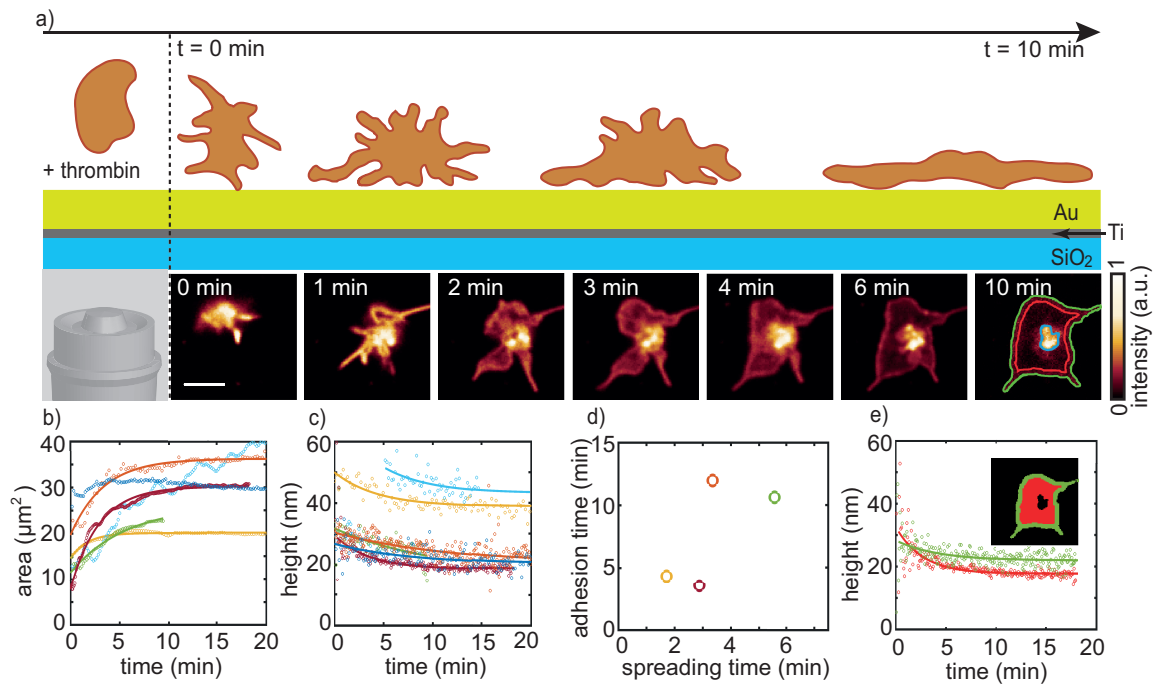


Figure 6.3: (a) Adhesion and spreading of a blood platelet upon stimulation with thrombin. Platelets show very fast dynamic changes as illustrated in the top scheme. The lower image sequence shows data recorded for dSQ12S-labeled cells by rapid FLIM with a scan speed of 3.3 fps (0.3 s per frame). For final analysis and display, 15 sequential images each are added to increase the signal-to-noise ratio. The sequence is modified by binning to 4.5 s per frame. The image at $t = 10$ min shows the segregation into three regions, the central area (disregarded, blue), the inner area (outlined in red) and the outermost rim of the platelet (outlined in green). The binned image sequence is provided as Movie S1. Scale bar corresponds to $3 \mu\text{m}$. (b) Time-dependent increase of spread area for 6 different cells. Each color denotes a single platelet. The data shown in dark red correspond to the platelet shown in a) and have been taken at 37°C , whereas the other data were recorded at room temperature. Open circles denote measured data, solid lines exponential fits. The platelets denoted by the dark blue and light blue data points do not show an exponential area increase and are thus not fitted. (c) Temporal evolution of the converted mean height values of the basal membrane for 6 different platelets. Color coding as in b). Open circles denote measured data, solid lines exponential fits. (d) Adhesion time constants plotted against spreading time constants for the 4 platelets that could be properly fitted. Color coding as in b) and c). (e) Temporal evolution of the basal membrane height for two different regions of the cell shown in Fig. 6.3a and in Fig. 6.3b,c and d as dark red color. The green data points correspond to the rim of the platelet and the red data points correspond to the inner area of the platelet without the bright central spot. Open circles show experimental data, solid lines exponential fits.

cells and the number of photons necessary for MIET imaging.

An illustration of the spreading process is shown in Fig. 6.3a, top, together with a typical image sequence between $t = 0$ min and $t = 10$ min (bottom). For most cells investigated here the platelet area does not change considerably at later time points. $t = 0$ min denotes the starting point of the scanning. The exact time between activation by thrombin and $t = 0$ min is variable and depends on how fast the

adhering platelet is localized and the microscope focused. Once we identify a platelet in its initial spreading state, we start to scan a small area of $10 \times 10 \mu\text{m}^2$ and wait for the platelet to fully adhere. The final spread area of approximately $30 \mu\text{m}^2$ for the example shown in Fig. 6.3a is reached with a time constant of 2.88 min as shown in Fig. 6.3b. The area data sets are fitted by an exponential growth function to obtain the spread time for each platelet and the time constants vary between 2 and 6 min as shown in Fig. 6.3d (x -axis). We exclude the dark and light blue curves from this analysis; for the dark blue curve, the recording had started only after the spreading process had already begun and extended filopodia affected the initial area. In the case of the light blue curve, the area is influenced by extending and retracting filopodia during the whole spreading time. The data curve shown in dark red denotes the increasing area of the platelet presented in Fig. 6.3a. These data were recorded at 37°C . The additional 5 data sets were recorded at room temperature and we observe no difference in platelet behavior, although the comparatively short spreading time may be due to the increased temperature. We include only platelets in the analysis that adhere to the substrate and spread *via* lamellipodia [161]. Our observed spreading times agree well with earlier studies [2, 3, 67, 69, 161].

For the example shown in Fig. 6.3a and Supplementary Movie S1, at the beginning of the spreading process, between $t = 0$ min and $t = 1$ min, we observe long, thin filopodia, which seem to search the substrate for optimal adhesion. These filopodia then increase in number and elongate. Between $t = 2$ min and $t = 3$ min, the filopodia start to expand laterally. As the platelet flattens, the filopodia are replaced by a thin lamellipodium centered around a bright spot. Such behavior is seen for all platelets considered in this work. This observation is in agreement with previous work, where platelets first form filopodia which are then transformed into lamellipodia, in particular if they spread on structured substrates [161] or if the substrate is coated with low-density fibrinogen [69, 162].

For further height analysis, the platelet spread area is split into separate regions as visualized in Fig. 6.3a at $t = 10$ min. The very bright emission in the cell center is likely linked to internalization of the membrane probe by endocytosis, as it was observed for a Nile Red analogue of dSQ12S [163]. For the reconstruction of our data, the signal from this region introduces artifacts and we thus exclude it from the analysis of later time points. For earlier points the intensity of the whole platelet is comparable and thus does not interfere with our analysis. TCSPC histograms of the remaining pixels are added and fitted with a bi-exponential decay. The short lifetime is converted into the height of basal membrane with help of a MIET calibration curve

like the one shown in Fig. 6.2b and plots of height against time are shown in Fig. 6.3c for 6 different platelets. Each color indicates an individual cell with the same color coding as for Fig. 6.3b. We observe a decrease of the basal membrane height over time, which indicates that the basal membrane of the platelet more closely approaches the metal surface as the spreading process proceeds. For the early time points, in some cases, it is impossible to distinguish between the contribution from the apical and the basal membrane as the membranes are not spread and unfolded yet. The data at later time points are fitted by an exponential decay function. The adhesion time constants vary between 3 to 12 min, and are thus larger than but in the same range as the spreading time constants of area increase. In Fig. 6.3d, we show adhesion times (y -axis, from Fig. 6.3c) plotted against spreading times (x -axis, from Fig. 6.3b). The platelet data shown in dark and light blue are omitted as we do not obtain a spreading time for those.

From Movie S1 it is evident that the rim of the platelet shows a higher level of activity than the central area. The morphological activity was previously described for thrombin-activated platelets using SICM [56]. In order to investigate the basal membrane activity, the platelet is segmented into two regions, as shown in Fig. 6.3a for $t = 10$ min and Fig. 6.3e, inset. The data in Fig. 6.3e and Movie S2 show that the inner area of the platelet (red) starts off higher, but then reaches a lower height than the rim (green). As discussed in the SICM study in Ref. [56], the reason might be that the rim has a higher activity compared to the rest of the platelet body.

6.5 Conclusions

Typical mammalian cells are several micrometers thick [71, 72] and extend well past the focal depth of a few hundreds of nanometers accessible by MIET imaging. Therefore, in previous studies it was safe to assume that all signal originated from the basal membrane of the cells under investigation. We show that single-color MIET imaging with a leaflet-specific fluorescent membrane probe allows for disentangling the contributions from the basal and apical membrane and obtaining accurate height profiles for the basal membrane. Even the apical membrane can be reconstructed when taking into account additional information gained by other methods. Thus, we are able to reconstruct the platelet shape in 3D. Whereas we applied the method to a particularly thin cell type, it may also be used to study flat parts of other cells, e.g. lamellipodia, axons or pili.

Apart from demonstrating the capability of single-color MIET imaging for distin-

guishing close-by membrane structures, our study quantifies platelet adhesion and spreading in a temporally and spatially resolved manner. Thus, we determine the three-dimensional structure of the basal membrane and find areas that are particularly close to the substrate and we speculate that they could be colocalized with force hot spots observed previously in traction force microscopy experiments [2]. The application of rapid MIET imaging to living cells allows us to distinguish the temporal evolution of adhesion for the very active outermost rim of the platelets and the central part that comes closer to the substrate as the platelet spreads.

This rapid MIET imaging mode, in particular, could well be applied to the study of other dynamic cell systems and in general the intracellular machinery which regulates cell spreading and adhesion, including integrins, signaling molecules and receptors. In this respect, it would be very interesting to study platelets from patients with bleeding disorders such as Glanzmann's thrombasthenia. By combining MIET with other super-resolution microscopy techniques, future prospects of our research could be extended to imaging distinct molecules simultaneously with the membrane. This option is becoming more feasible thanks to the development of new fluorescent dyes that will allow us to label specific molecules in non-nucleated platelets.

6.6 Acknowledgements

We thank J. Hanke for help with preliminary experiments, J.C. Thiele for help with the analysis software and N. Karedla for help with building the rapid FLIM setup, and the University Medical Center Göttingen, in particular T. Legler and J. Riggert, for providing the platelet concentrates. This work was funded by the German Research Foundation (DFG) in the framework of SFB 937, project A12 and A14 and under Germany's Excellence Strategy - EXC 2067/1- 390729940. The work was further financially supported by the European Research Council (ERC, Grant No. CoG 724932).

6.7 Supplementary Information

This section is published as Supplementary Information of "Time-resolved MIET measurements of blood platelet spreading and adhesion" (Anna Zelená, Sebastian Isbaner, Daja Ruhlandt, Anna Chizhik, Chiara Cassini, Andrey S. Klymchenko, Jörg Enderlein, Alexey Chizhik and Sarah Köster, *Nanoscale*, 2021, DOI:10.1039/D0NR05611A).

Reproduced from Ref. [6] with permission from Royal Society of Chemistry.

Supplementary Figures

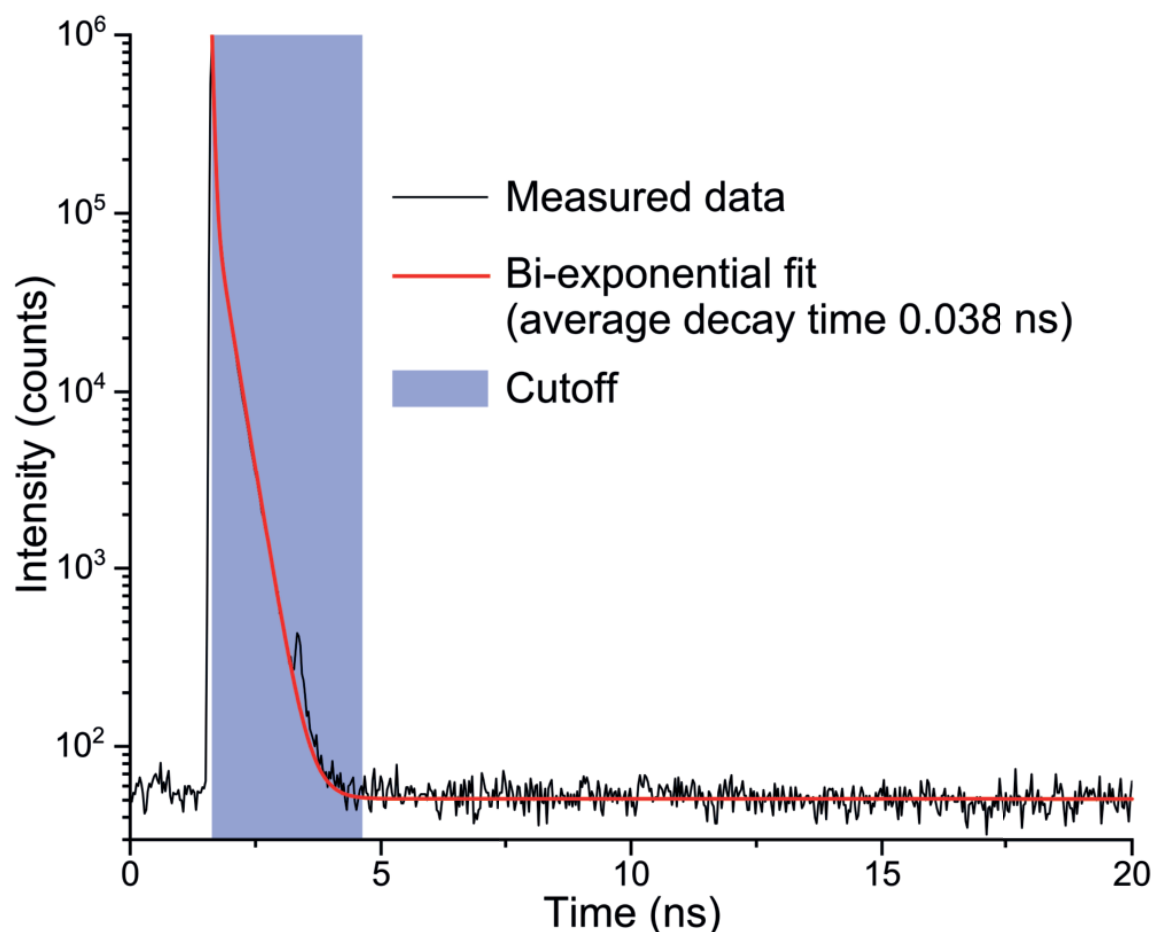


Figure 6.4: The instrument response function (IRF) of the microscope that was used for static MIET measurements. The curve was measured until reaching 10^6 counts at the maximum. The additional small peak at ~ 3 ns corresponds to a reflection of the excitation light from one of optical elements. Its intensity is, however, only 0.04% of the main maximum and does not lead to any change in the measured fluorescence decay curves.

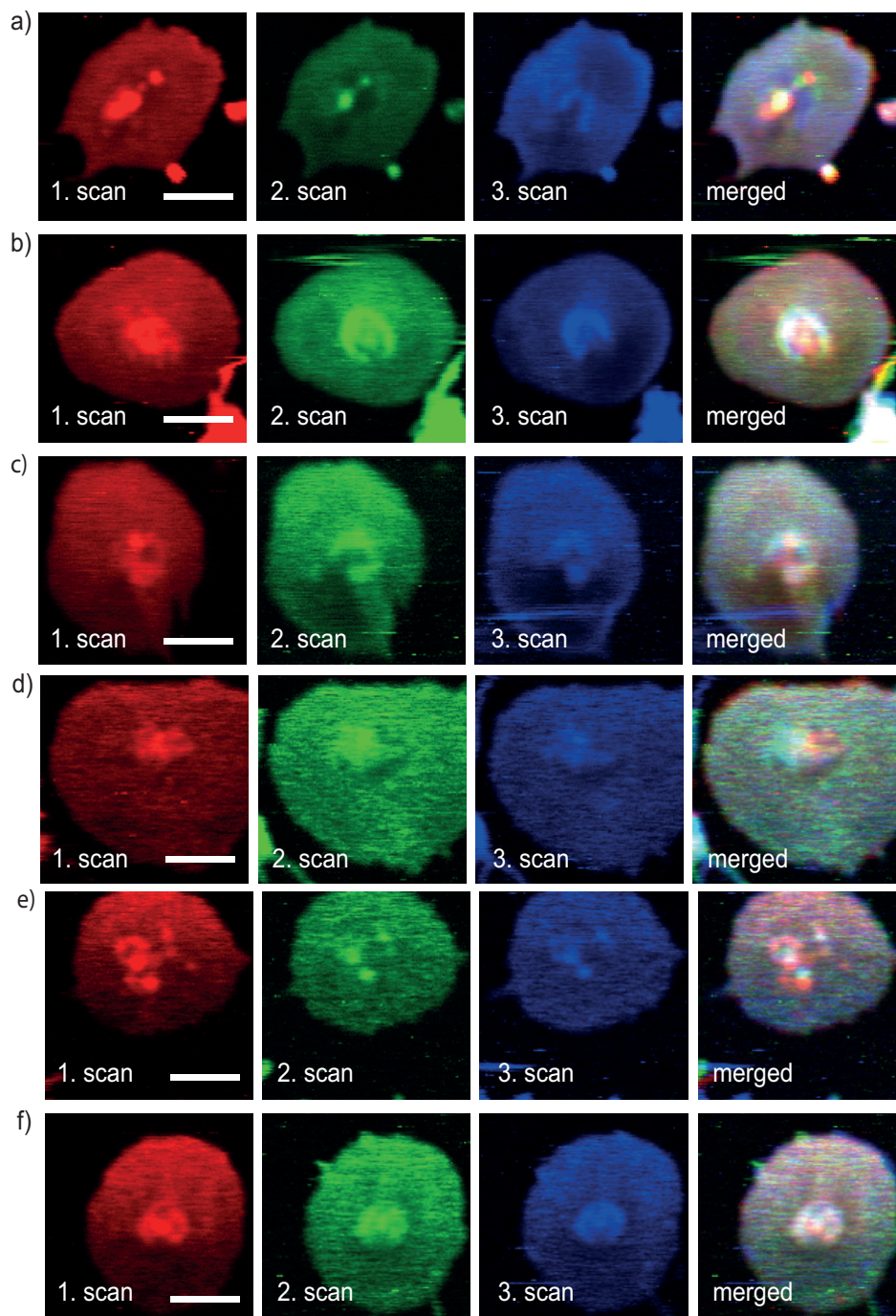


Figure 6.5: Triple scan for each platelet studied in static conditions. Each subfigure (a-f) represents a different platelet. Left to right: Individual scans of each blood platelet as well as a merged image from these three individual scans. The data show that the platelet area remains unchanged from the time point of the first scan on. Thus, we add the data of all three scans before further analysis. The total acquisition time of the three scans varies from 5.1 to 10.2 min depending on the size of the scanned area. Scale bars correspond to $3 \mu\text{m}$.

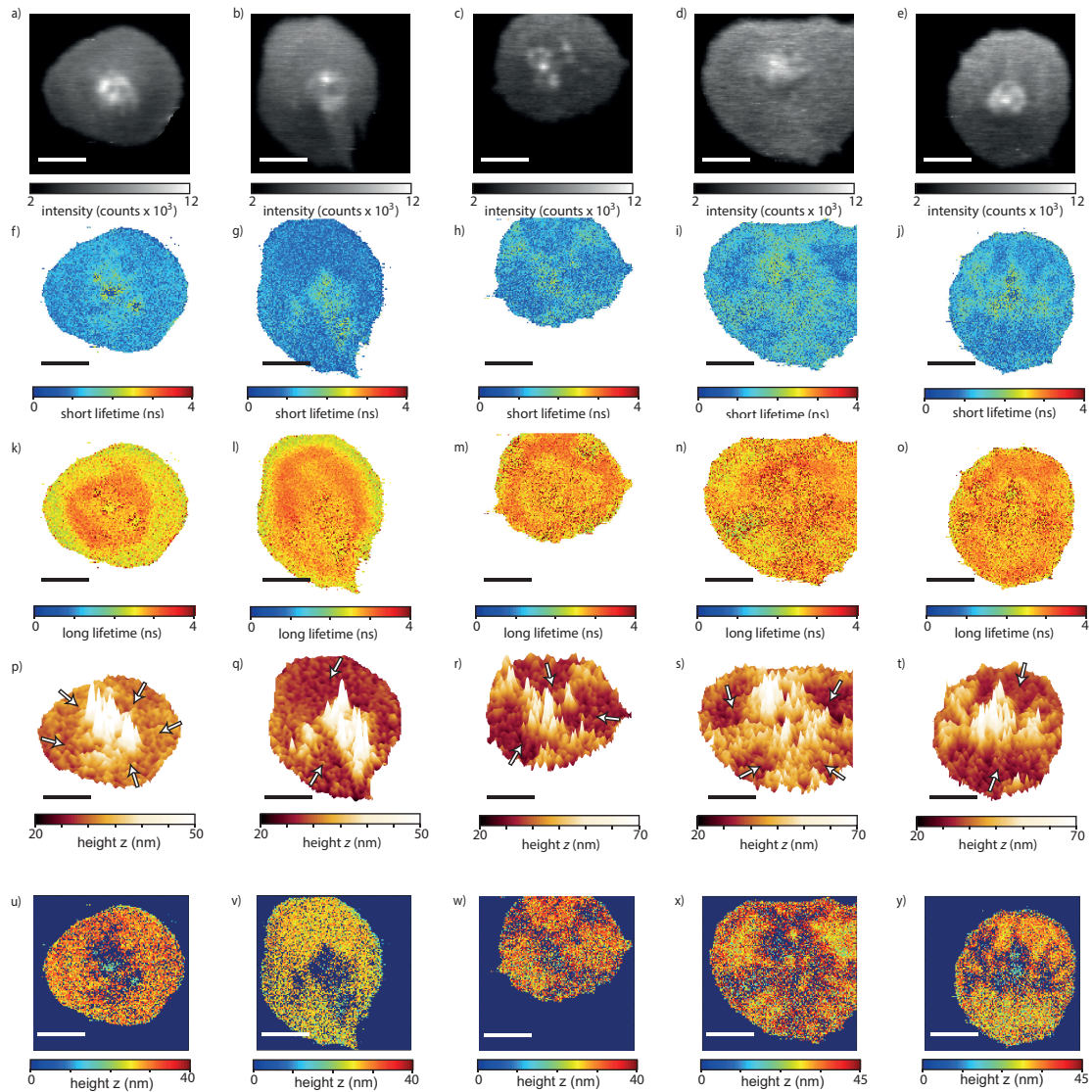


Figure 6.6: Additional examples of spread platelets. (a-e) Fluorescence intensity images. (f-j) Maps of the short life time components. (k-o) Maps of the long life-time components. (p-t) 3D reconstruction of the basal membrane; note the areas with smaller membrane-to-substrate distance (marked by the white arrows) in each platelet; for platelets (p-r) the color scale bar range is reduced compared to (s-t). The difference is due to a different noise level of the reconstruction. For clarity, the color scaling is chosen such that central bright areas show values above the color bar range. (u-y) Maps of membrane-to-substrate distance below the second tercile threshold. This representation highlights the localization of the areas with a smaller distance to the surface. The choice of the threshold is detailed in Fig. S4. Scale bars correspond to $3 \mu\text{m}$.

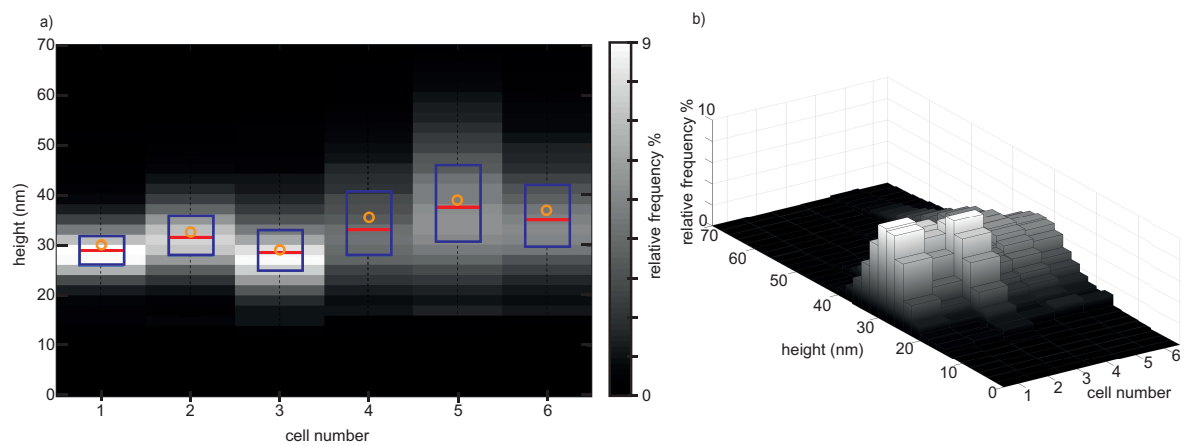


Figure 6.7: Histograms of the distance between gold layer and basal membrane for each of the six platelets analyzed here. (a) Top view of all histograms with the relative frequency color coded (see color scale). Each histogram was normalized by the total number of pixels. The overlaid boxplots show the 25-75 % percentile, the orange circle denotes the mean, and the red line the median. Outliers are less than 2% and hidden for clarity. Outliers occur when the separation of the basal and the apical membrane contributions is inaccurate. (b) 3D view of all histograms next to each other. The average height of the basal membrane is 34 ± 4 nm.

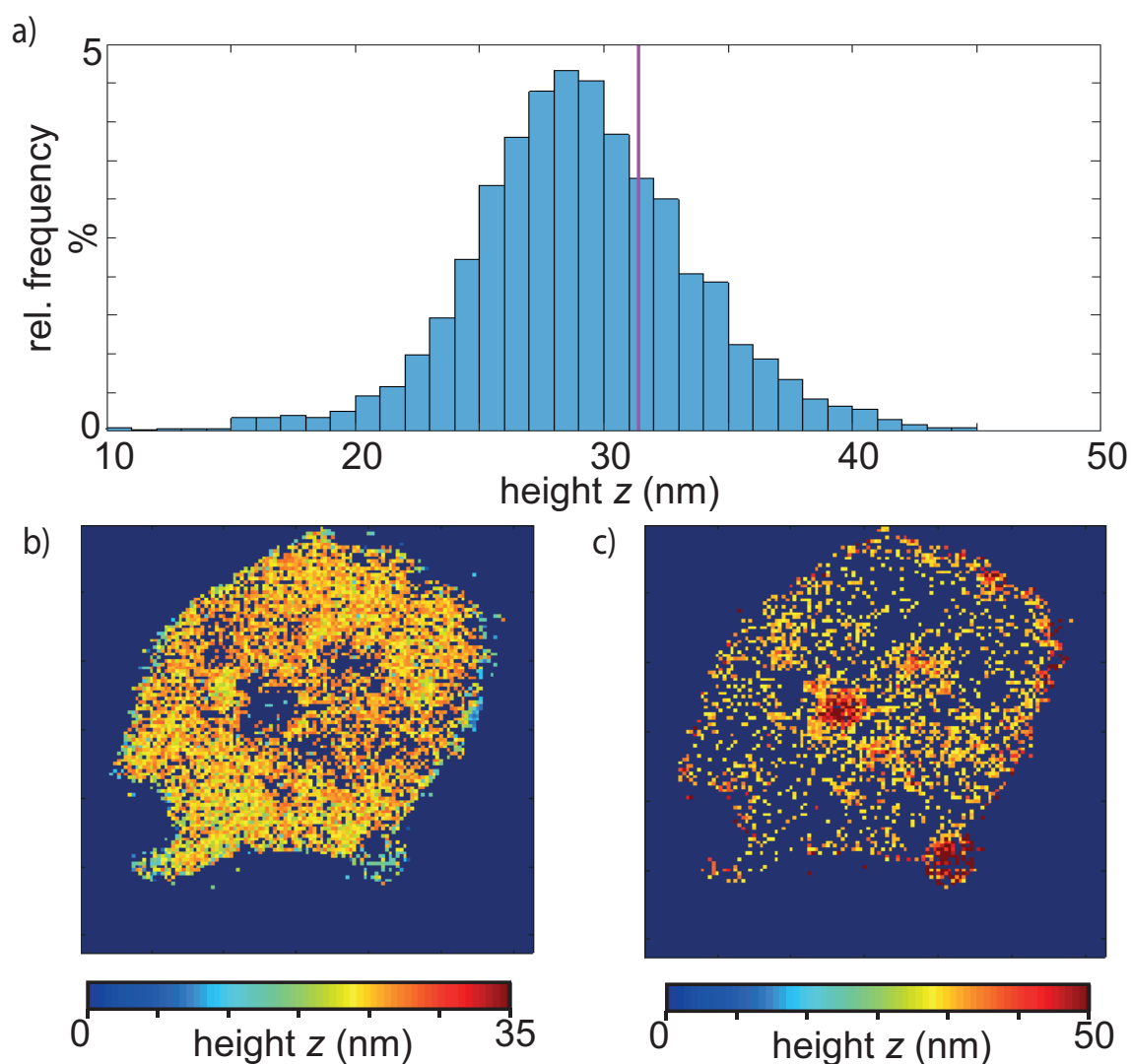


Figure 6.8: Analysis of the basal membrane profile. (a) Height histogram for the basal membrane after removal of outliers. Outliers are identified by using the “median absolute deviation” (MAD). For each data point, the MAD computes the absolute deviation from the data’s median and defines the median of all deviations. We define an outlier as a value that is more than three times the MAD away from the median.[164] As threshold we set the 2nd tercile, shown as the vertical purple line. (b) Height values below the threshold. (c) Height values above the threshold.

Supplementary movies

Electronic supplementary information (ESI) available: Supplementary figures and supplementary movies. See DOI: 10.1039/D0NR05611A

Movie S1: Adhesion and spreading of a blood platelet upon stimulation with thrombin. The platelet shows very fast dynamics, especially at the outermost rim of the cell. Data were recorded by rapid FLIM with a scan speed of 3.3 fps (0.3 s per frame). For final display, 15 sequential images each are added to increase the signal-to-noise ratio. The sequence is modified by temporal binning to 4.5 s per frame and shows intensities. Scale bar corresponds to 3 μm .

Movie S2: Adhesion and spreading of a blood platelet upon stimulation with thrombin, segmented into two areas. Each frame shows the averaged height for the outermost rim and the central area without the bright spot for later time points. Frame dimensions are $15 \times 15 \mu\text{m}^2$. The differing behavior of the rim and the rest of the cell is clearly visible.

Chapter 7

Force Generation in Human Blood Platelets by Actin Structures

This chapter has been prepared as a manuscript for publication with authors: Anna Zelená,^a Johannes Blumberg,^{b,c} Dimitri Probst,^{b,c} Ulrich S. Schwarz^{b,c} and Sarah Köster^{a,d,e}. S.K. and U.S.S. designed research and supervised this work; A.Z. performed research; J.B. and D.P. contributed data analysis tools; J.B. and A.Z. analyzed data; A.Z. and S.K. wrote and prepared the original manuscript for submission.

^a Institute for X-Ray Physics, University of Göttingen, Friedrich-Hund-Platz 1, 37077 Göttingen, Germany.

^b Institute for Theoretical Physics, University of Heidelberg, Philosophenweg 19, 69120 Heidelberg, Germany.

^c BioQuant-Center for Quantitative Biology, University of Heidelberg, Im Neuenheimer Feld 267, 69120 Heidelberg, Germany.

^d German Center for Cardiovascular Research (DZHK), partner site Göttingen, Germany.

^e Cluster of Excellence "Multiscale Bioimaging: from Molecular Machines to Networks of Excitable Cells" (MBExC), University of Göttingen, Germany.

7.1 Abstract

Blood platelets are known for their importance in blood clotting. Their correct function significantly affects the early steps of wound closing and thus restoring blood circulation. Their hemostatic function is directly connected to their mechanics and cytoskeletal morphology. However, the exact mechanism and connection between them remain elusive. As was previously investigated, the reorganization of their cytoskeleton is a very fast morphological process within minutes, and it forms various shapes of the stress fibers structures. Besides that, it was observed that high thrombin-activated platelets produce large forces in a range of hundreds nN typically exerted onto the substrate at hot spots locations. A similar trend was observed also for actin-labeled platelets and their shapes of the stress fibers structures. In this study, we shed more light on this missing connection by combining traction force microscopy (TFM) with silicon-rhodamine actin probes on living platelets in time-resolved manner and additionally test for different thrombin concentrations for platelet activation as well as different fibrinogen coverages on the substrate. We find that none of these parameters influences platelet spreading and contraction and interestingly, the hot spots in the force fields align well with the visualized end points of fibrous actin structures.

7.2 Introduction

Blood platelets are essential for blood clotting and primary hemostasis, and thus play an important role in wound healing. Platelets are non-nucleated fragments of megakaryocytes [1] with a large variability between the individual cells. They possess no microtubule organizing center [165], but contain the cytoskeletal filaments F-actin, microtubules [1], and desmin and vimentin intermediate filaments [29], as well as myosin molecular motors. In resting state, the platelets circulate in the blood stream as small discoids, shaped by the so-called marginal band consisting of a microtubule coil [1]. The activation of the platelets can be triggered by certain reagents such as adenosine diphosphate (ADP), thrombin, serotonin [153], but also by mechanical shear [166]. The most abundant activator of platelets is thrombin, which is also responsible for stabilization of the blood clot by enzymatic conversion of fibrinogen into fibrous fibrin [1, 167–169]. Once the platelets are activated, the marginal band is centralized by actomyosin [30, 31, 170, 171] and the platelet shape rapidly changes into a very flat and thin structure [65]. Subsequently, platelets first

start forming filopodia, then thin lamelopodia [33, 161, 172–174], and F-actin together with myosin forms stress fibers [61, 175].

Actomyosin is involved in force generation and platelet contraction. In order to gain a better understanding of the underlying mechanisms, direct – ideally dynamic – imaging of actin structures is of great importance. However, due to the lack of a nucleus, most experiments rely on staining of actin structures in fixed platelets by phalloidin. Using super-resolution fluorescence microscopy in combination with electron microscopy, actin structures have been imaged at high resolution [80]. The overall shapes of actin structures in platelets have been categorized and characterized by morphometric analysis, in dependence of different protein coatings and different substrate stiffnesses [80]. Notably, platelets from mice expressing LifeAct-GFP have been employed as well [42, 61]. These experiments revealed that platelets spread via actin-dependent structures, i.e., filopodia which are then filled by lamellipodia. The recently introduced silicon-rhodamine (SiR) actin probe [88] allows for life staining of actin in human platelets as well, and first experiments revealed a time constant of $245.2 \text{ s} \pm 143.9 \text{ s}$ for the formation of the complete actin cytoskeleton, compared to a faster spreading of the platelet membrane ($67.5 \text{ s} \pm 33.7 \text{ s}$ [3]).

Next to imaging, force measurements have been performed by, e.g., bulk rheology measurements [89] and on so-called microthrombi on elastic micro-pillars [99]. In order to distinguish effects by the platelets from influences of the matrix that connects them, single-cell measurements have been performed. Atomic force microscopy (AFM) reveals an average contractile force of $19 \pm 3.1 \text{ nN}$ ($n=30$) [90]. A similar force range, albeit slightly higher, was obtained from platelet contraction cytometry (PCC), based on the displacement of fibrinogen coated microdot pairs on hydrogels [102]. By staining fixed platelets, the authors showed that actin is involved in platelet force generation and the force are in the range of 20-50 nN . Traction force microscopy (TFM), rather than revealing total forces only, is able to compute spatio-temporally resolved force fields. Experiments with soft gels (4 kPa) have shown contractile forces in the range of 34 nN 25 minutes after platelet attachment to the gels [67]. Further development of the experimental setup and data analysis procedure has shown that forces produced by platelets can reach an averaged value of 200 nN in the range of 30 minutes. Moreover, the increased spatial resolution has allowed us to detect so-called force hot spots of the traction forces at the periphery of the platelets [2]. Thus, the force levels obtained by TFM are about an order of magnitude higher

than values from experiments with other methods. One reason might be different thrombin activation levels or fibrinogen coverage of the substrates employed in the different experiments. This idea is supported by experiments with larger clusters of platelets, which show that the generated forces increase with higher thrombin activation [99].

The imaging experiments of actin structures in platelets along with force measurements indicate that actomyosin is responsible for platelet spreading, shape formation and contraction. Here, we combine time-resolved TFM with live imaging of actin, and can thus quantify and correlate force fields and actin structures in a time-resolved manner. Interestingly, the force hot spots that have been observed before are spatially and temporally correlated with the endpoints of the actin stress fiber structures. We thus provide the first direct proof of force generation by actomyosin in platelets.

7.3 Materials and Methods

Platelet Purification and Actin Staining

Experiments are performed in accordance with the Ethics Committee of the University Medical Center Göttingen, votum 11/11/09. Platelet concentrates are obtained from healthy donors. Platelets are purified as previously described [2, 6, 67]. In brief, 4 mL of the platelet concentrate is transferred into a tube together with prostaglandin E1 (PGE1 2.6 $\mu\text{g}/\text{mL}$, Cayman Chemical Company, Ann Harbor, MI, USA). The content is mixed and centrifuged for 20 min at $480 \times g$ and 21°C . The supernatant is replaced by PIPES saline glucose buffer (PSG: 5 mM PIPES, 145 mM NaCl, 5 mM glucose, 4 mM KCl, 1 mM MgCl_2 , 0.05 mM Na_2HPO_4 , pH 6.8) with PGE1. The centrifugation step is repeated twice. After the last removal of the supernatant, the pellet is re-suspended in HEPES-Tyrode buffer (HT: 134 mM NaCl, 12 mM NaHCO_3 , 2.9 mM KCl, 1 mM MgCl_2 , 5 mM HEPES, 5 mM glucose, 0.34 mM NaH_2PO_4 , pH 7.4) with bovine serum albumin (BSA, 5 mg/mL, Macs BSA stock solution, Milteny Biotech, Bergisch Gladbach, Germany). The platelets are counted using a hematocrit capillary (sodium heparinized 75 mm and 75 μL , Hirschmann Laborgeräte GmbH, Eberstadt, Germany) and diluted to a final concentration of 2×10^7 cells/mL. SiR-actin (final concentration 0.5 μM , Ex/Em: 652/674 nm, Spirochrome Ltd., Stein am Rhein, Switzerland) is added to the diluted platelet suspension and incubated to 15 min, before the samples are used in the experiments.

Fabrication of PAA Substrates

The protocol is adapted from Ref. [134]. Square glass coverslips (24 mm × 24 mm No. 1, VWR, Radnor, Pennsylvania, USA) are cleaned with isopropanol and dried under a nitrogen stream. Subsequently, both sides of the glass coverslips are exposed to an air plasma (0.5 mbar, ZEPTO, Diener Electronics GmbH, Ebhausen, Germany) for 1.5 minutes at 50 W. Next, the coverslips are soaked in a silanization solution consisting of 2%(v/v) 3-(trimethoxysilyl)propyl methacrylate (Sigma-Aldrich, St. Louis, Missouri, USA) and 1%(v/v) acetic acid (100%, Carl-Roth GmbH, Karlsruhe, Germany) in absolute ethanol ($\geq 99.8\%$, Carl-Roth GmbH) for 10 minutes. The excess of the solution is aspirated, and the coverslips are rinsed with ethanol. Air-dried silanized coverslips are baked at 120° C for 1 hour and stored at room temperature.

For the experiments employing different thrombin concentrations, circular glass coverslips (\varnothing 18 mm No. 1, VWR) are cleaned with isopropanol, dried under a nitrogen stream, coated with PlusOne Repel-Silane (GE Healthcare, Little Chalfont, UK) from both sides for 5 minutes, and washed with ethanol. A PAA mixture for a final gel stiffness of 34 kPa is prepared by mixing 2.5 mL of acrylamide (40%, Bio-Rad Laboratories Inc., Hercules, CA, USA), 0.75 mL of bis-acrylamide (2%, Bio-Rad Laboratories Inc.), and 6.75 mL of phosphate-buffered saline (1×PBS: 137 mM NaCl, 2.7 mM KCl, 10 mM Na₂HPO₄, 1.8 mM KH₂PO₄, pH 7.2). 10 μ L carboxylated beads (0.2% solids, FluoSpheres, carboxylate-modified microspheres, 40 nm in diameter, yellow-green, 505/515 nm, Thermo Fisher Scientific Inc., Waltham, MA, USA) are added to 490 μ L of the PAA solution. The addition of 10 μ L ammonium persulfate (10% APS, Bio-Rad Laboratories Inc.) and 0.5 μ L TEMED (N,N,N',N'-Tetramethylethane-1,2-diamine, Bio-Rad Laboratories Inc.) initiates the polymerization. The PAA solution is mixed and 10 μ L are pipetted on a circular, PlusOne Repel-Silane-treated coverslip and covered by a squared silanized coverslip. The gel is polymerized upside-down for 1 hour. After the polymerization, the gel is soaked in PBS and the circular glass coverslip is removed. The top layer of the gel is coated twice with Sulfo-SANPAH (0.4 mM in 50 mM HEPES buffer (pH=8), Thermo Fisher Scientific Inc.) by applying UV light for 8 minutes (365 nm 2 tube 8 W, Herolab GmbH Laborgeräte, Wiesloch, Germany). Subsequently, 150 μ L of fibrinogen solution (100 μ g/mL, CalBiochem-Merck KGaA, Darmstadt, Germany) is added on top of the gel and incubated overnight at 5° C to achieve uniform coverage. Coated gels are washed with PBS and kept submerged in PBS until used in the experiments.

For testing different degrees of fibrinogen coating, we use micro-patterned substrates. To do so, we employ Light-Induced Molecular Adsorption of Proteins (LIMAP) using a PRIMO setup (Alveóle, Paris, France) installed on an inverted fluorescence microscope (IX83, Olympus, Hamburg, Germany) equipped with a 20× objective (LUCPLFLN, /0.45 N.A. air, Olympus) and controlled *via* the software Leonardo (Alveóle). Circular glass coverslips (Ø 20 mm No. 1, VWR) are washed with isopropanol, dried under a nitrogen stream, and plasma-treated for 3 minutes at 50 W. A PDMS (polydimethylsiloxane) stencil with a well of Ø 3.5 mm is placed on top of the plasma-treated coverslip. The glass coverslip area inside the well is passivated using 10 µL of PLL-g-PEG (0.1 mg/mL in PBS (PLL(20)-g[3.5]-PEG(2 kDa)), SuSoS AG, Dübendorf, Switzerland) and incubated for 1 hour, followed by washing three times with PBS. After removing the PBS, the empty well is filled with 5 µL PLPP (Alveóle). The PLPP degrades the passivated layer of PLL-g-PEG after exposure to UV light to a degree that is linearly dependent on the dose [136]. The maximum dose we use for printing a pattern is 2000 mJ/mm² corresponding to 100% fibrinogen coverage. According to the linear dependence between dose and coverage, we prepare samples with 25% and 10% of the dose. After exposure to the UV light, the glass area inside the well is washed three times with PBS and subsequently filled by 10 µL of fibrinogen solution (100 µg/mL, CalBiochem-Merck KGaA). The protein is incubated inside of the well for 2 hours at 5° C and washed three times with PBS. Successful patterning is proven by using fluorescently labeled fibrinogen (100 µg/mL, AlexaFluor 488 conjugate, Ex/Em: 495/519 nm, Invitrogen, Darmstadt, Germany).

To transfer the fibrinogen patterns from the glass coverslips to PAA gels, the PDMS stencil is removed and the glass coverslip is dried by blotting with tissues. A PAA mixture is prepared as described above (note that in this case the fluorescent beads are passivated with PLL-g-PEG (0.1 mg/mL in PBS (PLL(20)-g[3.5]-PEG(2 kDa)), SuSoS AG)), pipetted to the top of the circular, patterned coverslip, and covered by a squared, silanized coverslip. After 1 hour, the gels are soaked in PBS and the top glasses with the pattern are gently removed. The surface of the gel now presents the previously produced fibrinogen pattern.

Traction Force Microscopy and Imaging

All TFM experiments, independent of the gel preparation procedure, are conducted on an inverted microscope (IX81, Olympus), equipped with a 60X water immersion objective (UPlanApo, NA = 1.2, Olympus) and a CMOS camera (Orca Flash 4.0, Hamamatsu Photonics Deutschland GmbH, Herrsching am Ammersee, Germany). Prepared PAA gels are washed with HT buffer containing BSA and placed inside an incubation chamber (Stage Top Incubator STX, Tokai Hit Co., Ltd., Fujinomiya, Shizuoka-ken, Japan), including a home-built sample holder optimized for 24 mm × 24 mm coverslips. The incubation chamber guarantees stable physiological conditions of 5% CO₂ and 37°C throughout the experiment. All gels have a thickness of at least 50 μm and we select areas with homogeneous bead coverage for the experiments.

Ninety μL of SiR-actin stained platelet suspension are pipetted on the preheated PAA gel. Ten μL of thrombin solution (thrombin from human plasma activity 2800 U/mg (U denotes NIH-units here), Sigma-Aldrich; diluted in HT with BSA) is added directly before the recording starts to activate the platelets. The final thrombin concentration varies from 0.05 U/mL to 11.2 U/mL. The different fibrinogen coatings are investigated using a thrombin concentration of 0.1 U/mL. For the fluorescence imaging, we employ a dual-band filter (FITC/Cy5; excitation at 470 nm and 628 nm and emission at 537 nm and 694 nm (AHF Analysentechnik AG, Tübingen, Germany)). We record the platelet spreading for 2 hours at one frame every 7.5 s.

Data Analysis

Traction force microscopy

For analysis of the TFM data, we employ optical flow using the Kanade-Lucas-Tomasi (KLT) algorithm with a regularization-based approach [2]. Briefly, the image sequences with the recorded beads are down-sampled from 16 to 8 bit in ImageJ[144]. The Shi-Tomasi corner detector tracks to find position of maximum 1000 beads. To avoid double-counting of clusters, a minimum distance between beads is set to 3 pixels. The pyramidal KLT algorithm is used to track the intensity gradients around the detected beads within search windows of size 48 by 48 pixels and in the second round of size 24 by 24 pixels. The displacements are tracked between successive

images and the complete trace is reconstructed with reference to the undeformed image before adhesion of the platelet. We assume a linear movement inside each of the search windows using an Euler forward approach. The drift correction is applied on a small area of the image sequence without deformation and the detected drift is subtracted from all calculated displacements. The drift-corrected displacements are distributed on a regular 4 by 4 pixels grid. Application of a Tukey filter ($\alpha=0.2$) ensures a zero velocity field at the border of the grid with drift-corrected displacements. The traction forces are calculated by Fourier Transform Traction Cytometry (FTTC) with Tikhonov regularization using regularization parameters defined by a Generalized Cross-Validation (GCV) function. The total force F_{tot} is given by

$$F_{tot} = \int_{A_{roi}} |\vec{T}(\vec{x})| dA_{roi}, \quad (7.1)$$

where $\vec{T}(\vec{x})$ is the traction force at a given position \vec{x} , A_{roi} defines the selected area containing a single contracting platelet.

Area Covered by Actin Structures

The time point $t_0 = 0$ min for each video is defined such that it corresponds to the starting point of contraction determined from the total force $F_{tot}(t)$. For the determination of t_0 the curve is smoothed using the *rloess* function in Matlab [149], which reduces the effect of outliers. t_0 is defined as the time point of the first maximum of the second derivative of the smoothed $F_{tot}(t)$.

The area $A_a(t)$ covered by actin at any given time point in the image sequence corresponds to the platelet spread area. It is determined by first applying a Gaussian filter with standard deviation 1 on the image sequence to reduce the noise. The smoothing is essential in particular for the analysis of the early time points. Next, we threshold the image following Kittler's method of minimum error thresholding [150]. The method performs well in cases where the distributions of the object and background have unequal variances. The finally obtained area A_a is cleaned of unconnected segments.

7.4 Results

Influence of Thrombin Concentration on Platelet Spreading and Force Generation

To investigate the spreading speed and force evolution of platelets when activated by different thrombin concentrations between 0.05 U/mL and 11.2 U/mL, we record movies of the emerging actin structures and, in parallel, the bead patterns below the platelets, which are then used to calculate the force fields. All gels are incubated with a fibrinogen solution with a concentration of 100 $\mu\text{g/mL}$. At a concentration of 0.05 U/mL, we do not observe spreading, actin structure formation or force generation. We thus find that the threshold thrombin concentration for platelet activation lies between 0.05 U/mL and 0.1 U/mL. The actin structures in thrombin-activated platelets dramatically change upon spreading on a fibrinogen-coated gel as shown for a typical example in Fig. 7.1B. We analyze the increase of the area occupied by actin structures A_a with respect to time rather than the fluorescence intensity, as it has been shown that the binding kinetics of the SiR actin probe is slower than the actin polymerization dynamics [3]. Fig. 7.1C shows $A_a(t)$, color-coded for the different thrombin concentrations used for platelet activation. The dashed lines denote the data, averaged from a minimum of 19 platelets each, whereas the transparent areas show the standard deviations. Whereas the data show a slight, systematic decrease with increasing thrombin concentration, the standard deviations strongly overlap. The total force $F_{tot}(t)$, derived from the traction forces according to Eq. 7.1, for each thrombin concentration is shown in Fig. 7.1D. The averaged data are shown as dotted lines and the standard deviations transparent areas. For a quantitative comparison, we fit an exponential growth function,

$$F_{tot}(t) = F_{max} \cdot [1 - B \cdot \exp(-t/\tau)], \quad (7.2)$$

where F_{max} is the maximum force, $F_{max} - B$ is the initial force and τ is the time constant. The resulting parameters F_{max} and τ are shown in Fig. 7.1E and F, respectively. The values show no significant difference (Kolmogorov-Smirnov test, $p > 0.05$). Thus, our data confirm that despite their small size, platelets produce large forces of several hundreds nN and we show that these forces are independent of the thrombin concentration.

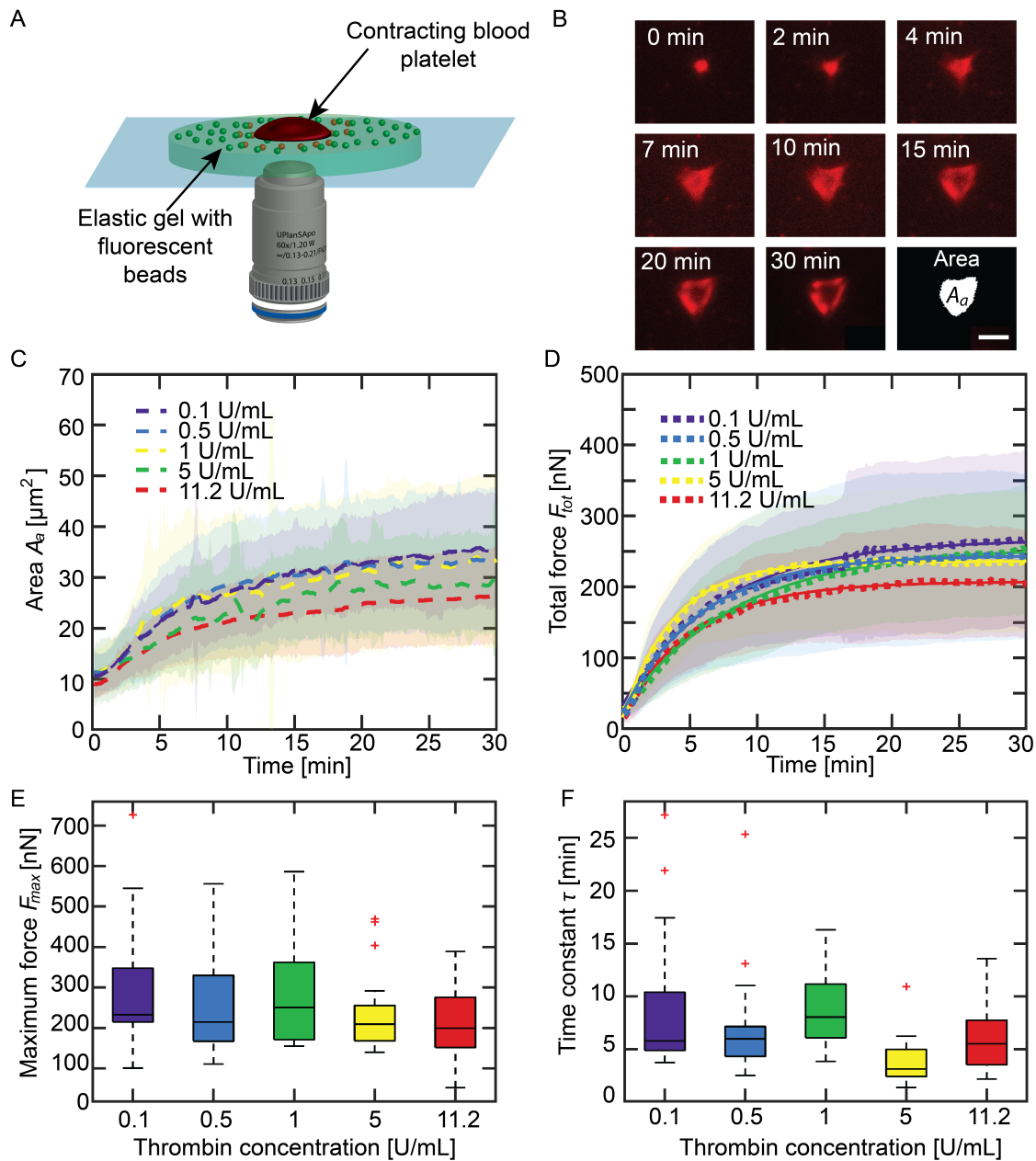


Figure 7.1: (A) Schematic representation of the experimental setup. A contracting platelet (red) on top an elastic gel (light green) displaces the fluorescent beads (green). The deformation of the gel due to the contraction is visualized as orange beads. (B) Epifluorescence micrographs of a blood platelet stained for actin spreading on an elastic gel after stimulation by thrombin. The last image shows a binarized version of the $t = 30$ min micrograph. The scale bar corresponds to $5 \mu\text{m}$ and refers to all sub-panels. (C) The average time-dependent total area covered by actin structures upon stimulation by different concentrations of thrombin. Each averaged curve contains a minimum of 19 data sets and the standard deviations as the transparent areas. (D) Average total force curves for blood platelets ($n \geq 19$) upon stimulation by different concentrations of thrombin are shown as dotted lines, the standard deviations are included as the transparent areas. Averaged exponential fits are shown as solid lines. (E) Maximum forces for each data set comprising the averaged total force curves shown in subfigure (D). The red crosses indicate outliers. (F) Time constants for each data set comprising the averaged total force curves shown in subfigure (D). The red crosses indicate outliers.

Influence of Fibrinogen Coverage on Platelet Spreading and Force Generation

In a next step, we systematically investigate – similar to the experiments described above – the spreading speed and force evolution in dependence of the fibrinogen coverage. We use a thrombin concentration of 0.1 U/mL just above the threshold determined above and a fibrinogen solution with a concentration of 100 $\mu\text{g}/\text{mL}$. The varying surface coverage (100%, 25%, 10%) is obtained by photo patterning (LIMAP). Fig.7.2A shows the average area $A_a(t)$ covered by actin structures for each coverage (dashed lines). The actin area shows no systematic influence of the fibrinogen coating and the standard deviations (transparent areas) overlap. In parallel for the actin imaging, we again record the substrate deformation and determine the total force $F_{tot}(t)$ for each fibrinogen coverage, see Fig. 7.2B. Each single measurement curve is fitted exponentially according to Eq. 7.2, and the averaged fit curves are shown as solid lines. The fit parameters F_{max} and τ are shown in Fig. 7.2C and D, respectively, and they show no significant difference. Our results show that neither the thrombin concentration in the platelet suspension nor the fibrinogen coverage on the substrate influence the platelet spreading, actin structure formation and force generation.

Spatial Correlation of Actin Structures and Force Fields in Spread Platelets

When carefully inspecting both the force fields (Fig. 7.3A) and the outlines of the actin structures (Fig. 7.3B), we observe similar geometrical patterns. The force is mostly concentrated at the edges of the cell in so-called force hot spots [2]. To quantify the spatial and temporal correlation of the force fields and actin structures, we first determine the position of the force hot spots using the Matlab function *Fast 2D peak finder* [151]. Here, we focus on those peaks that exceed a level of 50% of the highest traction force at each time point. For each platelet, we determine the centroid of these peaks $C_f(x_{cf}, y_{cf})$ (see orange crosses in Fig. 7.3A) and the mean radial distance of the force MRD_f , defined as the average Euclidean distance between the centroid C_f and the detected hot spots:

$$\text{MRD}_f = \frac{1}{K_f} \cdot \sum_{k=1}^{K_f} \sqrt{(x_{cf} - x_f(k))^2 + (y_{cf} - y_f(k))^2},$$

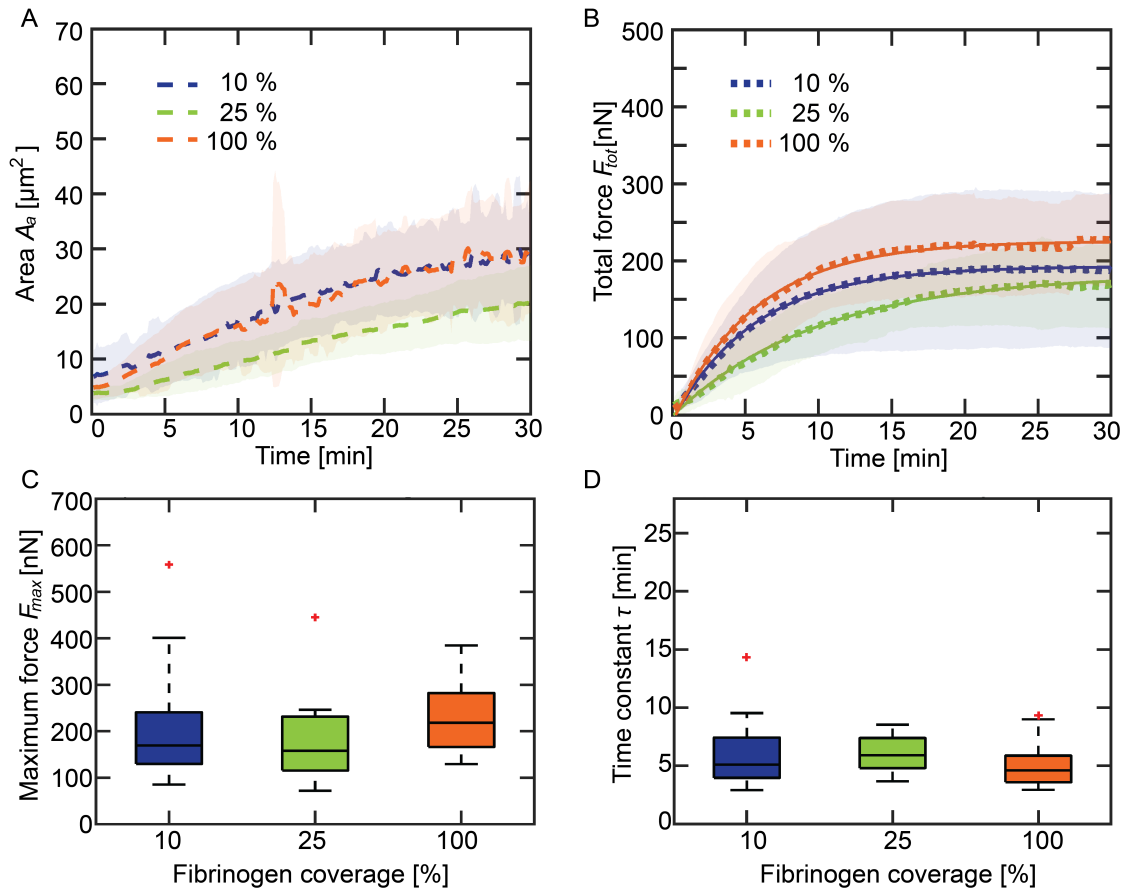


Figure 7.2: (A) Average time-dependent total area covered by actin structures on elastic gels coated in various fibrinogen concentrations. The thrombin concentration is 0.1 U/mL. Each averaged curve contains a minimum of 13 data sets and the standard deviations as the transparent areas. (B) Average total force curves for blood platelets ($n \geq 13$) upon stimulation by thrombin (0.1 U/ml) on gels covered by various concentrations of fibrinogen (dotted lines), the standard deviations are included as the transparent areas. Averaged exponential fits are shown as solid lines. Each dataset comprising the averaged curves is also fitted and the maximum forces and time constants are determined. (C) Maximum forces for each data set comprising the averaged total force curves shown in subfigure (B). The red crosses indicate outliers. (D) Time constants for each data set comprising the averaged total force curves shown in subfigure (B). The red crosses indicate outliers.

where K_f is number of detected peaks and (x_f, y_f) are coordinates of the detected peaks.

Second, we determine the centroid of the actin boundary $C_a(x_{ca}, y_{ca})$ (see blue stars in Fig. 7.3B) at each time point. Additionally, we introduce a variable for the mean radial distance of the actin area MRD_a , defined as the average Euclidean distance between the centroid C_a and the actin boundary:

$$MRD_a = \frac{1}{K_a} \cdot \sum_{k=1}^{K_a} \sqrt{(x_{ca} - x_a(k))^2 + (y_{ca} - y_a(k))^2},$$

where K_a is number of pixels on the actin boundary and (x_a, y_a) are the coordinates of the pixels.

In Fig. 7.3C, we show a typical example of the time-dependent distance between the centroid of the force hot spots C_f and centroid of the actin boundary C_a . The averaged value is indicated by the black dashed line. For each measurement, we determine the time-averaged distance, shown in Fig. 7.3D and E. The results show no significant difference (Kolmogorov-Smirnov test, $p > 0.05$) between the thrombin concentrations and fibrinogen coverages.

In Fig. 7.3F we present an example of the MRD_a and MRD_f of one typical platelet. It is evident that both curves show a very similar exponential increase. We quantify this trend by fitting the curves with an exponential model:

$$MRD(t) = MRD_{max} \cdot [1 - B \cdot \exp(-(t + d)/\tau)],$$

where MRD_{max} is the maximum MRD_a or MRD_f , respectively, d is the time offset, and τ is the time constant. We determine the time constants as plotted in Fig. 7.3G and H. In agreement with all previous results, also τ_{MRD_a} and τ_{MRD_f} show no significant difference between the measured conditions (Kolmogorov-Smirnov test, $p > 0.05$). However, when comparing the medians and interquartile ranges (IQR) of τ_{MRD_a} ($n=147, 4.35 \pm 3.1$ min) and τ_{MRD_f} ($n=147, 2.3944 \pm 1.96$ min) for all conditions, we find that τ_{MRD_f} is significantly faster (Kolmogorov-Smirnov test $p < 0.05$).

To illustrate the variability of the geometrical shapes, in Fig. 7.4A-D we present different geometrical patterns with concentrated force hot spots at the edges of the cell. These hot spots are located at the ends of the clearly visible actin structures as shown in Fig. 7.4E-H and are more obvious from their overlay in Fig. 7.4I-L. This model is schematically shown in Fig. 7.4M.

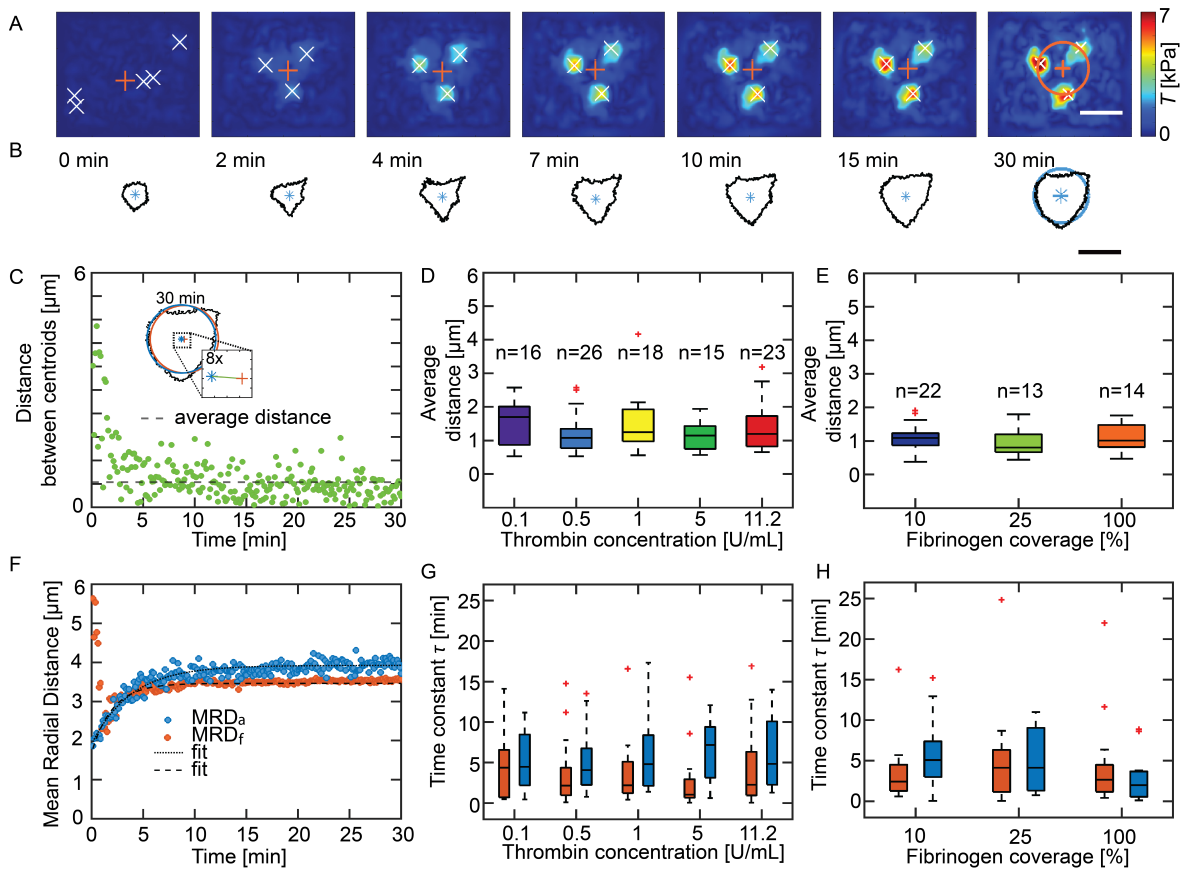


Figure 7.3: (A) Image sequence showing the temporal evolution of the force distribution corresponding to the same time points shown in subfigure B. White crosses represent the centers of the force hot spots. For each image, the centroid of the hot spots is calculated and is represented as an orange cross. The orange circle shown on the $t = 30$ min image has a radius equal to the mean radial distance of the force (MRD_f) between the centroid and the black crosses. (B) Image sequence showing the time evolution of the actin boundary. For each image, the centroid is represented by a blue star. As an example, the blue circle shown in the $t = 30$ min image has a radius equal to the mean radial distance (MRD_a) between the centroid and the actin boundary. Corresponding MRD_a are calculated for each time point of the video and each individual platelet. The scale bar corresponds to $5 \mu\text{m}$ and refers to all sub-panels. (C) Inset shows overlay of the actin boundary (black), MRD_a circle (blue) and MRD_f circle (orange) for the $t = 30$ min image. The distance between the centroids of the two circles is shown in the inset and is represented by the green line. The distance between the centroids is calculated for each time point and is plotted in a time-resolved manner. The average distance is represented as the dashed black dashed line. This analysis is repeated for every platelet used in the experiments with thrombin and fibrinogen concentration. (D) Distribution of the average distance between the MRD_a and MRD_f circles for each thrombin concentration. The red crosses indicate outliers. (E) Distribution of the average distance between the MRD_a and MRD_f circles for each fibrinogen concentration. The red cross indicates outliers. (F) Temporal evolution of the MRD_a (blue) and MRD_f (orange) for the example shown in subfigures (A-C). (G-H) Distribution of the time constant for the radial evolution for each MRD_a circle (blue box plots) and MRD_f circle (orange box plots). See axis labels for different conditions. The red crosses indicate outliers.

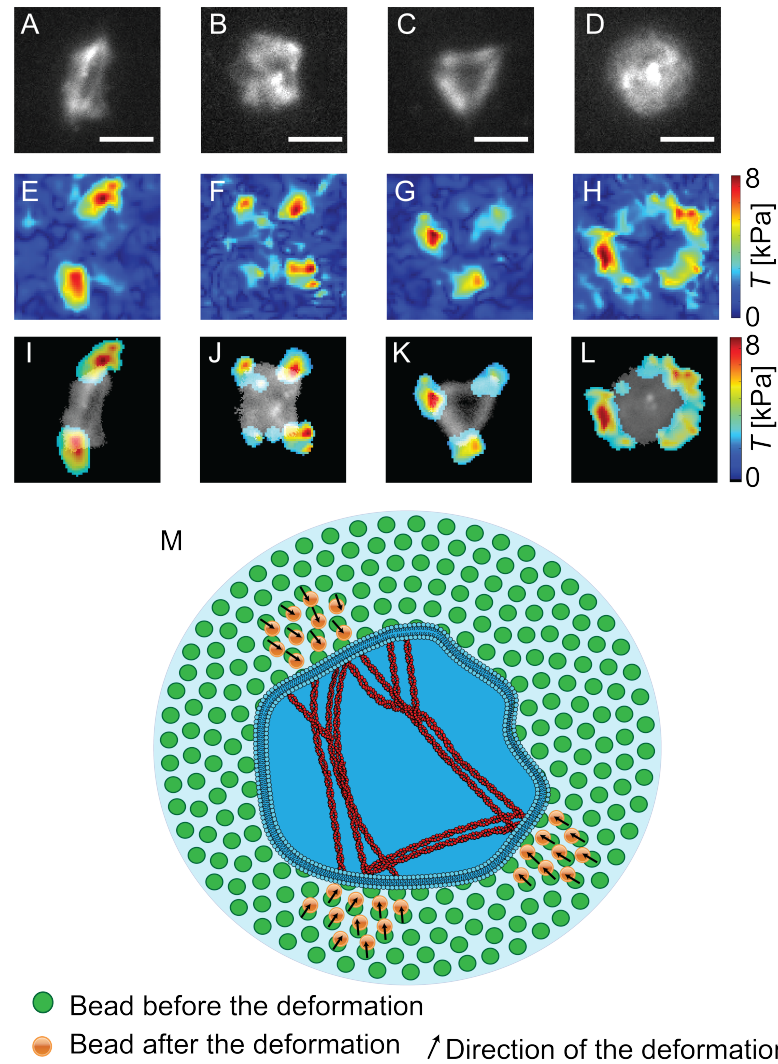


Figure 7.4: (A-D) The recorded actin structures at the final time point of spreading for four typical platelets. In most cases, the actin pattern shows an (A) spindle-like, (B) square, (C) triangular, or (D) elliptic/circular shape. (E-H) Reconstructed traction forces for the platelets shown in (A-D). We observe a stable force hot spot distribution. (I-L) The shape of the hot spot distribution overlaps with the actin structure. Note that for reasons of visibility, the background color is changed to black (see colormap). (M) Schematic representation of a mechanism for force generation that is supported by our findings. The deformations in the substrate due to the contraction of the platelet are represented by the orange (versus green in a relaxed state) beads. The black arrows indicate the directions of the bead displacements. The actin stress fibers, whose endpoints coincide with the force hot spots, are shown in red.

7.5 Discussion and Conclusions

Despite the challenge of measuring forces and imaging the cytoskeleton in small cells such as platelets, great efforts and the employment of different methods have led to a number of important results concerning the force-generating mechanism, as presented in the introduction. Here, we add to this picture by building on our earlier work and combining the direct in situ actin imaging [3] with TFM [2] and thereby directly connect force generation and cytoskeletal structure formation. The lack of a nucleus in platelets enforces us to use SiR actin as a probe to visualize the formation of stress-fibers in human platelets and we reveal similar structures as have been observed by immunostaining of chemically fixed platelets [42, 61, 80] as well as in time-resolved experiments with spreading platelets on stiff glass substrates[3]. In agreement with our earlier work[2], we find that the maximum total force of few hundreds nN is generated within 30 min and with the average time constant for the force increase is 6.7 ± 4.04 min. This observation is also in a good agreement with the observed time constant for actin structure formation on glass (4.1 ± 2.40 min) [3].

Because of the limited resolution of our imaging, in particular for the early time points, we analyze the overall substrate coverage by actin, which corresponds to the spreading area, rather than individual stress fibers. The limitations in resolution are caused by the slow binding kinetics of the SiR actin probe [88] as well as by the fact, that the imaging is performed through a relatively thick PAA gel with an increasing background by unbound dyes. Our results confirm that platelets produce the largest traction forces in force hot spots [2] and are able to spatially and temporarily correlate these hot spots with the end points of straight actin structures, which we interpret as actin stress fibers. Similarly, a recent study reports that at a high-level tension regime integrins are focused at two to three spots at the periphery after 4 minutes [105]. This is in a good agreement with our observed results. Interestingly, we observe a significantly slower time constant for the development of actin structures compared to the time constant for the evolution of force fields. This indicates that the hot spots are spatially stabilized before the actin structures are fully rearranged. This could indicate, that the spatial force distribution is organized at early time points of the actin polymerization; at a later stage, the acto-myosin interactions increase the force and stabilize the contraction.

Interestingly, neither the total force, nor the time constant for force generation, nor

the actin area or the correlation of actin structures and forces fields are influenced by varying concentrations of thrombin added to the platelets suspension or the fibrinogen coverage on the substrate. Biologically, this could indicate that platelet contraction, and possibly function in general, is a very robust process that is not easily influenced by external parameters. By contrast to our results, a recent study shows that an increasing thrombin concentration increases platelet forces in microthrombi [99]. Hence, our results on a single platelet may indicate that the force increase in microthrombi is more likely connected to the cell-cell interaction or to the tension of fibrin fibers in the larger cluster of cells. It is not clear yet, if all platelets within a microthrombus actively contribute to the force increase and how. Therefore, further research on small ensembles of platelets is needed to validate this hypothesis. An investigation of their adhesion and dynamics of the forces could provide information in this regard.

The biological significance is undeniable. Our study provides a missing connection between the formation of actin structures and force generation and thus uncovers the behavior of native healthy platelets. This study has the potential in the future to better understand, how bleeding disorders like Glanzmann's thrombasthenia or Bernard-Soulier syndrome influence the force generation and formation of actin structures.

7.6 Acknowledgments

We thank the University Medical Center Göttingen, in particular Alexander Strate, Tobias Legler and Joachim Riggert, for providing platelet concentrates. This work was funded by the German Research Foundation (DFG) in the framework of SFB 937, project A12 and under Germany's Excellence Strategy - EXC 2067/1- 390729940. The work was further financially supported by the European Research Council (ERC, Grant No. CoG 724932). U.S.S. is a member of the cluster of excellence CellNetworks and of the Interdisciplinary Center for Scientific Computing (IWR) at Heidelberg.

Chapter 8

Summary, Conclusion and Outlook

This thesis aims to characterize the dynamics of the adhesion and contraction behavior of spreading platelets with high time resolution. Two studies implementing two different methods are presented here; the first study is focused on the adhesion of the platelet membrane using MIET in static and rapid modes, while the second is focused on the correlation of contraction forces with actin structures formation using TFM analysis and in situ actin imaging.

The first study presented in this thesis contributes to a better understanding of platelet-matrix interactions and additionally demonstrates the resolution capability of single-color MIET in static and rapid mode. The high axial and spatial resolutions in the static MIET mode reveal three-dimensional structures of the basal membrane with areas that are particularly close to the metal substrate. The spatial distribution of these areas likely corresponds to focal adhesion spots, and we hypothesize that they co-localize with the force hot spots previously observed with TFM experiments [2].

In the study of the dynamic adhesion process, the MIET method is extended for a fast scanning mode, the so-called rapid MIET. We demonstrate the applicability of the rapid mode to the adhesion process of human blood platelets and confirm its applicability for other fast biological models. The resolution of the rapid mode allowed us to distinguish the behavior of the outer rim of the platelet and central part. We demonstrate, that the central part of the platelet adheres particularly closer to the metal surface than the outer rim.

The second study presented in this thesis follows up on our previous results by measuring traction forces on soft (4 kPa) and stiff hydrogels (19-83 kPa) [2, 67], and correlates the force distribution with the shape of actin structures using in situ actin imaging [3]. This thesis expands the application of SiR actin stained platelets to the

simultaneous measurement of contraction forces with TFM and actin structures of human blood platelets with high spatial and temporal resolutions.

In agreement with previous studies, we confirm the production of relatively high forces independent of the activation level by various thrombin concentrations and different fibrinogen coverage. We confirm our hypothesis that the distribution of so-called hot spots correlates with the shape of actin structures. Additionally, we observe that the force hot spots reach their final distribution before the actin structures become stagnant. This indicates that the force distribution is organized at early time points of the actin polymerization and the acto-myosin interactions increase the force and stabilize the contraction. The investigation of filament formation is experimentally demanding, but more data need to be collected for conclusive results. The limitations of the actin resolution are due to the slow binding kinetics of the SiR actin probe and the resulting background signal caused by unbound dye [88]. Moreover, the imaging is performed through a ~ 50 μm PAA gel, which further increases the background signal. Improvement of the imaging and actin staining will allow for the correlation of actin filament formation and stress fibers.

Interestingly, we observe no significant difference in the formation of actin structures or the temporal distribution of contraction forces under the influence of various thrombin concentrations or changes in the fibrinogen coverage of the substrate. However, as a recent study shows, increasing thrombin concentration results in larger forces produced in microthrombi [99]. So far, the contributions of single platelets to the contraction of microthrombi are not known. Our observations indicate that the force increase in microthrombi is likely connected to cell-cell interactions or increasing tension between fibrin fibers rather than to cell-matrix interactions. This hypothesis requires more investigation of interactions within larger platelet groups. Altogether, the studies presented in this thesis, contribute many new insights into the mechanisms of the platelet spreading and adhesion processes. The biological significance is undeniable for both studies. Application of the measurements described in this thesis to platelets from patients with bleeding disorders like Glanzmann's thrombasthenia (dysfunction of integrin $\alpha\text{IIb}\beta 3$) [176] or Bernard-Soulier syndrome (abnormalities of GPIb-IX) [177] will give insight into the mechanisms that interfere with the spreading and adhesion process and might, eventually, allow for therapeutic measures.

In future, it would be interesting to spatially and temporally correlate the observed trends in structures of the basal membrane with actin filaments and distributions of force hot spots. This may be potentially the next step in the development of the

MIET method, which is constantly evolving, as evidenced by the latest research using new materials like graphene-based MIET [178] or coating with silica spacers [115]. Nevertheless, the results with the stiff surface can still provide a lot of new information. The current knowledge of the platelet behavior in presence of gels with stiffness above 50 kPa [179] as well as around 35 kPa [80] reveals a similar trend in the platelet adhesion and spreading areas as on the stiff glass substrate >50 GPa [180]. The membrane morphology and dynamics we observe by MIET on stiff substrate might therefore be, at least partially, transferable to the force distributions and actin structures we obtain from the TFM studies on soft substrates. This indicates that there may be an analogy between our observed membrane structures in the first MIET study and the actin structures and force distributions from the second TFM study. While this assumption would need to be further confirmed by application of softer materials together with MIET, the current set up can further help to answer how platelets interact within a small group of platelets or in microthrombi as mentioned earlier. Additionally, it would be interesting to also investigate the dynamic of other platelet systems occurring in the regularization and spreading mechanisms of platelets like integrins or signaling molecules. To strengthen the link between the cytoskeletal organization and contractility, it is alternatively possible to use also single-platelet experiments with micropatterning and obtain rather regular than randomly distributed cells of required shape. It would be interesting to investigate the single-platelet behavior on micropatterned surfaces. The spatial control over the platelet shape would allow for controlled actin structures and eventually also interactions between more cells.

From this work, we conclude that, despite the lack of nuclei and the relatively small size of platelets, high-resolution techniques can be optimized to investigate the morphological changes during platelet spreading and adhesion, along with their contraction forces. We reveal the dynamics of the basal membrane morphology during platelet spreading. In particular, we confirm that the edge of the membrane is further away from the surface than the central part of the platelet. Moreover, we demonstrate that human blood platelets, despite their small size, are able to produce large forces comparable to large cells. These forces are independent of external activation levels and the spatial distribution of force hot spots is clearly correlated to the actin structures. By extending these detailed single-platelet studies to the investigation of small clusters of platelets the contribution of single cell and cell-cell properties will be revealed and, finally, allow a clearer picture of the physics that define the vital process of blood clot formation.

Bibliography

1. Michelson, A. D. *Platelets* <https://doi.org/10.1016/c2016-0-03693-8> (Elsevier, 2019).
2. Hanke, J., Probst, D., Zemel, A., Schwarz, U. S. & Köster, S. Dynamics of force generation by spreading platelets. *Soft Matter* **14**, 6571–6581. <http://dx.doi.org/10.1039/C8SM00895G> (2018).
3. Paknikar, A. K., Eltzner, B. & Köster, S. Direct characterization of cytoskeletal reorganization during blood platelet spreading. *Prog. Biophys. Mol. Biol.* **144**, 166–176. <https://doi.org/10.1016/j.pbiomolbio.2018.05.001> (2019).
4. Hanke, J. *The Influence of Substrate Elasticity and Shear Rate on Human Blood Platelet Contraction* <https://doi.org/10.17875/gup2019-1128> (Göttingen University Press, 2018).
5. Probst, D. Continuum Modeling of Cell Contractility. <http://archiv.ub.uni-heidelberg.de/volltextserver/id/eprint/25143> (2018).
6. Zelená, A. *et al.* Time-resolved {MIET} measurements of blood platelet spreading and adhesion. *Nanoscale* **12**, 21306–21315. <https://doi.org/10.1039/d0nr05611a> (2020).
7. Ribatti, D. & Crivellato, E. Giulio Bizzozero and the discovery of platelets. *Leuk. Res.* **31**, 1339–1341. <https://doi.org/10.1016/j.leukres.2007.02.008> (2007).
8. Garraud, O. & Cognasse, F. Are Platelets Cells? And if Yes, are They Immune Cells? *Front. Immunol.* **6**. <https://doi.org/10.3389/fimmu.2015.00070> (2015).

9. Moras, M., Lefevre, S. D. & Ostuni, M. A. From Erythroblasts to Mature Red Blood Cells: Organelle Clearance in Mammals. *Front. Physiol.* **8**. <https://doi.org/10.3389/fphys.2017.01076> (2017).
10. Grozovsky, R., Hoffmeister, K. M. & Falet, H. Novel clearance mechanisms of platelets. *Current Opinion in Hematology* **17**, 585–589. <https://doi.org/10.1097%2Fmoh.0b013e32833e7561> (Nov. 2010).
11. Becker, R. P. & De Bruyn, P. P. H. The transmural passage of blood cells into myeloid sinusoids and the entry of platelets into the sinusoidal circulation; a scanning electron microscopic investigation. *Am. J. Anat.* **145**, 183–205 (1976).
12. Thiery, J. P. & Bessis, M. Genesis of blood platelets from the megakaryocytes in living cells. *C. R. Hebd. Seances Acad. Sci.* **242**, 290–292 (1956).
13. Nishikii, H. *et al.* Metalloproteinase regulation improves in vitro generation of efficacious platelets from mouse embryonic stem cells. *Journal of Experimental Medicine* **205**, 1917–1927. <https://doi.org/10.1084/jem.20071482> (July 2008).
14. Wang, Y. *et al.* Comparative analysis of human ex vivo-generated platelets vs megakaryocyte-generated platelets in mice: a cautionary tale. *Blood* **125**, 3627–3636. <https://doi.org/10.1182/blood-2014-08-593053> (June 2015).
15. Avanzi, M. P., Izak, M., Oluwadara, O. E. & Mitchell, W. B. Actin Inhibition Increases Megakaryocyte Proplatelet Formation through an Apoptosis-Dependent Mechanism. *PLOS ONE* **10** (ed Mandal, M.) e0125057. <https://doi.org/10.1371/journal.pone.0125057> (Apr. 2015).
16. Patel, S. R. The biogenesis of platelets from megakaryocyte proplatelets. *J. Clin. Invest.* **115**, 3348–3354. <https://doi.org/10.1172/jci26891> (2005).
17. Wright, J. H. The origin and nature of the blood plates. *Bost. Med. Surg. J.* **154**, 643–645 (1906).
18. Martin, J. F. & Wagner, G. P. The origin of platelets enabled the evolution of eutherian placentation. *Biol. Lett.* **15**, 20190374. <https://doi.org/10.1098/rsbl.2019.0374> (2019).
19. Schwertz, H. *et al.* Anucleate platelets generate progeny. *Blood* **115**, 3801–3809. <https://doi.org/10.1182/blood-2009-08-239558> (2010).

20. Italiano, J. E., Lecine, P., Shivdasani, R. A. & Hartwig, J. H. Blood Platelets Are Assembled Principally at the Ends of Proplatelet Processes Produced by Differentiated Megakaryocytes. *J. Cell Biol.* **147**, 1299–1312. <https://doi.org/10.1083/jcb.147.6.1299> (1999).
21. Choi, E. S., Nichol, J. L., Hokom, M. M., Hornkohl, A. C. & Hunt, P. Platelets generated in vitro from proplatelet-displaying human megakaryocytes are functional. *Blood* **85**, 402–413. <https://doi.org/10.1182/blood.v85.2.402.402> (Jan. 1995).
22. Cramer, E. M. *et al.* Ultrastructure of platelet formation by human megakaryocytes cultured with the Mpl ligand. *Blood, J. Am. Soc. Hematol.* **89**, 2336–2346 (1997).
23. Bornert, A. *et al.* Cytoskeletal-based mechanisms differently regulate. *Haematologica* **106**, 1368–1380. <https://doi.org/10.3324/haematol.2019.239111> (2020).
24. Frelinger, A., Michelson, A. & Gremmel, T. Platelet Physiology. *Semin. Thromb. Hemost.* **42**, 191–204. <https://doi.org/10.1055/s-0035-1564835> (2016).
25. Shamova, E. V. *et al.* Redox regulation of morphology, cell stiffness, and lectin-induced aggregation of human platelets. *Eur. Biophys. J.* **40**, 195–208. <https://doi.org/10.1007/s00249-010-0639-2> (2010).
26. Behnke, O. Electron microscopical observations on the surface coating of human blood platelets. *J. Ultrastruct. Res.* **24**, 51–69. [https://doi.org/10.1016/s0022-5320\(68\)80016-4](https://doi.org/10.1016/s0022-5320(68)80016-4) (1968).
27. Rosa, J.-P., Raslova, H. & Bryckaert, M. Filamin A: key actor in platelet biology. *Blood* **134**, 1279–1288. <https://doi.org/10.1182/blood.2019000014> (2019).
28. O\textquotesingleHalloran, T., Beckerle, M. C. & Burridge, K. Identification of talin as a major cytoplasmic protein implicated in platelet activation. *Nature* **317**, 449–451. <https://doi.org/10.1038/317449a0> (1985).
29. Cerecedo, D. Platelet cytoskeleton and its hemostatic role. *Blood Coagul. {&} Fibrinolysis* **24**, 798–808. <https://doi.org/10.1097/mbc.0b013e328364c379> (2013).
30. Diagouraga, B. *et al.* Motor-driven marginal band coiling promotes cell shape change during platelet activation. *J. Cell Biol.* **204**, 177–185. <https://doi.org/10.1083/jcb.201306085> (2014).

31. Sadoul, K. New explanations for old observations: marginal band coiling during platelet activation. *J. Thromb. Haemost.* **13**, 333–346. <https://doi.org/10.1111/jth.12819> (2015).
32. Hartwig, J. & Italiano, J. The birth of the platelet. *J. Thromb. Haemost.* **1**, 1580–1586. <https://doi.org/10.1046/j.1538-7836.2003.00331.x> (2003).
33. Hartwig, J. H. The Platelet: Form and Function. *Semin. Hematol.* **43**, S94–S100. <https://doi.org/10.1053/j.seminhematol.2005.11.004> (2006).
34. Hartwig, J. H. & DeSisto, M. The cytoskeleton of the resting human blood platelet: structure of the membrane skeleton and its attachment to actin filaments. *J. Cell Biol.* **112**, 407–425. <https://doi.org/10.1083/jcb.112.3.407> (1991).
35. Patel-Hett, S. *et al.* The spectrin-based membrane skeleton stabilizes mouse megakaryocyte membrane systems and is essential for proplatelet and platelet formation. *Blood* **118**, 1641–1652. <https://doi.org/10.1182/blood-2011-01-330688> (2011).
36. Hartwig, J. *Thrombosis and Hemorrhage* 1998.
37. Fox, J., Boyles, J. K., Berndt, M. C., Steffen, P. K. & Anderson, L. K. Identification of a membrane skeleton in platelets. *The Journal of cell biology* **106**, 1525–1538 (1988).
38. Niederman, R. & Pollard, T. D. Human platelet myosin. {II}. In vitro assembly and structure of myosin filaments. *J. Cell Biol.* **67**, 72–92. <https://doi.org/10.1083/jcb.67.1.72> (1975).
39. Adam, F. *et al.* Kinesin-1 Is a New Actor Involved in Platelet Secretion and Thrombus Stability. *Arterioscler. Thromb. Vasc. Biol.* **38**, 1037–1051. ISSN: 1079-5642. <https://doi.org/10.1161/atvbaha.117.310373> <https://www.ahajournals.org/doi/10.1161/ATVBAHA.117.310373> (2018).
40. Zaninetti, C., Sachs, L. & Palankar, R. Role of Platelet Cytoskeleton in Platelet Biomechanics: Current and Emerging Methodologies and Their Potential Relevance for the Investigation of Inherited Platelet Disorders. *Hamostaseologie* **40**, 337–347. <https://doi.org/10.1055/a-1175-6783> (2020).
41. Bender, M. & Palankar, R. Platelet Shape Changes during Thrombus Formation: Role of Actin-Based Protrusions. *Hamostaseologie* **41**, 14–21. <https://doi.org/10.1055/a-1325-0993> (2021).

42. Calaminus, S. D. J., Thomas, S., McCarty, O. J. T., Machesky, L. M. & Watson, S. P. Identification of a novel, actin-rich structure, the actin nodule, in the early stages of platelet spreading. *J. Thromb. Haemost.* **6**, 1944–1952. <https://doi.org/10.1111/j.1538-7836.2008.03141.x> (2008).
43. Hou, Y. *et al.* Platelets in hemostasis and thrombosis: Novel mechanisms of fibrinogen-independent platelet aggregation and fibronectin-mediated protein wave of hemostasis. *J. Biomed. Res.* <https://doi.org/10.7555/jbr.29.20150121> (2015).
44. Rao, L. V. M. & Pendurthi, U. R. Tissue Factor{\textendash}Factor {VIIa} Signaling. *Arterioscler. Thromb. Vasc. Biol.* **25**, 47–56. <https://doi.org/10.1161/01.atv.0000151624.45775.13> (2005).
45. Rumbaut, R. E. & Thiagarajan, P. Platelet-Vessel Wall Interactions in Hemostasis and Thrombosis. *Colloq. Ser. Integr. Syst. Physiol. From Mol. to Funct.* **2**, 1–75. <https://doi.org/10.4199/c00007ed1v01y201002isp004> (2010).
46. Geiger, B., Bershadsky, A., Pankov, R. & Yamada, K. M. Transmembrane crosstalk between the extracellular matrix and the cytoskeleton. *Nat. Rev. Mol. Cell Biol.* **2**, 793–805. <https://doi.org/10.1038/35099066> (2001).
47. Hui, S. W. & Costa, J. L. Topography and Thickness of Air-Dried Human Platelets Measured by Correlative Transmission and Scanning Electron Microscopy. *J. Microsc.* **115**, 203–206. <https://doi.org/10.1111/j.1365-2818.1979.tb00171.x> (1979).
48. White, J. G. in *Platelets and Megakaryocytes* 47–64 (Humana Press, 2004). <https://doi.org/10.1385/1-59259-782-3:047>.
49. Neumüller, J., Ellinger, A. & Wagner, T. in *Transm. Electron Microsc. - Theory Appl.* (InTech, 2015). <https://doi.org/10.5772/60673>.
50. Fritz, M., Radmacher, M. & Gaub, H. E. In Vitro Activation of Human Platelets Triggered and Probed by Atomic Force Microscopy. *Exp. Cell Res.* **205**, 187–190. <https://doi.org/10.1006/excr.1993.1074> (1993).
51. Fritz, M., R., M. & Gaub, H. E. Granula motion and membrane spreading during activation of human platelets imaged by atomic force microscopy. *Biophys. J.* **66**, 1328–1334. ISSN: 0006-3495. <http://www.sciencedirect.com/science/article/pii/S0006349594809634> (1994).

52. Radmacher, M., Fritz, M., Kacher, C. M., Cleveland, J. P. & Hansma, P. K. Measuring the viscoelastic properties of human platelets with the atomic force microscope. *Biophys. J.* **70**, 556–567. [https://doi.org/10.1016/s0006-3495\(96\)79602-9](https://doi.org/10.1016/s0006-3495(96)79602-9) (1996).
53. Zhang, Y. *et al.* Contact- and agonist-regulated microvesiculation of human platelets. *Thromb. Haemost.* **110**, 331–399. <https://doi.org/10.1160/th12-11-0853> (2013).
54. Rheinlaender, J. *et al.* Imaging the elastic modulus of human platelets during thrombin-induced activation using scanning ion conductance microscopy. *Thromb. Haemost.* **113**, 305–311. <https://doi.org/10.1160/th14-05-0414> (2015).
55. Kraus, M.-J. *et al.* Comparative morphology analysis of live blood platelets using scanning ion conductance and robotic dark-field microscopy. *Platelets* **27**, 541–546. <https://doi.org/10.3109/09537104.2016.1158400> (2016).
56. Seifert, J., Rheinlaender, J., Lang, F., Gawaz, M. & Schäffer, T. E. Thrombin-induced cytoskeleton dynamics in spread human platelets observed with fast scanning ion conductance microscopy. *Sci. Rep.* **7**, 4810. ISSN: 2045-2322 (2017).
57. Liu, X. *et al.* Use of non-contact hopping probe ion conductance microscopy to investigate dynamic morphology of live platelets. *Platelets* **26**, 480–485. <https://doi.org/10.3109/09537104.2014.940888> (2014).
58. Heintzmann, R. & Ficz, G. Breaking the resolution limit in light microscopy. *Brief. Funct. Genomics Proteomics* **5**, 289–301. <https://doi.org/10.1093/bfgp/e11036> (2006).
59. Schermelleh, L., Heintzmann, R. & Leonhardt, H. A guide to super-resolution fluorescence microscopy. *J. Cell Biol.* **190**, 165–175. <https://doi.org/10.1083/jcb.201002018> (2010).
60. MacDonald, L., Baldini, G. & Storrie, B. in *Membrane Trafficking* 255–275 (Springer New York, 2014). https://doi.org/10.1007/978-1-4939-2309-0_19.
61. Poulter, N. S. *et al.* Platelet actin nodules are podosome-like structures dependent on Wiskott-Aldrich syndrome protein and {ARP}2/3 complex. *Nat. Commun.* **6**. <https://doi.org/10.1038/ncomms8254> (2015).
62. Schmidt, R. *et al.* Spherical nanosized focal spot unravels the interior of cells. *Nat. Methods* **5**, 539–544. <https://doi.org/10.1038/nmeth.1214> (2008).

63. Hell, S. W., Schmidt, R. & Egner, A. Diffraction-unlimited three-dimensional optical nanoscopy with opposing lenses. *Nat. Photonics* **3**, 381–387. <https://doi.org/10.1038/nphoton.2009.112> (2009).
64. Schmidt, R. *et al.* Mitochondrial Cristae Revealed with Focused Light. *Nano Lett.* **9**, 2508–2510. <https://doi.org/10.1021/nl901398t> (2009).
65. Aquino, D. *et al.* Two-color nanoscopy of three-dimensional volumes by 4Pi detection of stochastically switched fluorophores. *Nat. Methods* **8**, 353–359. ISSN: 1548-7091. <https://doi.org/10.1038/nmeth.1583><http://www.nature.com/articles/nmeth.1583> (2011).
66. Okamura, Y. *et al.* A few immobilized thrombins are sufficient for platelet spreading. *Biophys. J.* **100**, 1855–1863 (2011).
67. Henriques, S., Sandmann, R., Strate, A. & Köster, S. Force field evolution during human blood platelet activation. *J. Cell Sci.* **125**, 3914–3920. <https://doi.org/10.1242/jcs.108126> (2012).
68. Hanke, J., Ranke, C., Perego, E. & Köster, S. Human blood platelets contract in perpendicular direction to shear flow. *Soft Matter* **15**, 2009–2019. <https://doi.org/10.1039/c8sm02136h> (2019).
69. Lee, D., Fong, K. P., King, M. R., Brass, L. F. & Hammer, D. A. Differential Dynamics of Platelet Contact and Spreading. *Biophys. J.* **102**, 472–482. ISSN: 0006-3495 (2012).
70. Chizhik, A. I., Gregor, I., Ernst, B. & Enderlein, J. Nanocavity-Based Determination of Absolute Values of Photoluminescence Quantum Yields. *ChemPhysChem* **14**, 505–513 (2013).
71. Chizhik, A. I., Rother, J., Gregor, I., Janshoff, A. & Enderlein, J. Metal-induced energy transfer for live cell nanoscopy. *Nat. Photonics* **8**, 124 (2014).
72. Baronsky, T. *et al.* Cell–Substrate Dynamics of the Epithelial-to-Mesenchymal Transition. *Nano Lett.* **17**, 3320–3326 (2017).
73. Chizhik, A. M. *et al.* Three-dimensional reconstruction of nuclear envelope architecture using dual-color metal-induced energy transfer imaging. *ACS Nano* **11**, 11839–11846 (2017).
74. Chizhik, A. M. *et al.* Dual-color metal-induced and Förster resonance energy transfer for cell nanoscopy. *Mol. Biol. Cell* **29** (ed Bassereau, P.) 846–851. <https://doi.org/10.1091/mbc.e17-05-0314> (2018).

75. White, J. G. Fine Structural Alterations Induced in Platelets by Adenosine Diphosphate. *Blood* **31**, 604–622. <https://doi.org/10.1182/blood.v31.5.604.604> (1968).
76. Maupin, P., Phillips, C. L., Adelstein, R. S. & Pollard, T. D. Differential localization of myosin- $\{II\}$ isozymes in human cultured cells and blood cells. *J. Cell Sci.* **107**, 3077–3090. <https://doi.org/10.1242/jcs.107.11.3077> (1994).
77. Fegghi, S., Tooley, W. W. & Sniadecki, N. J. Nonmuscle Myosin $\{IIA\}$ Regulates Platelet Contractile Forces Through Rho Kinase and Myosin Light-Chain Kinase. *J. Biomech. Eng.* **138**. <https://doi.org/10.1115/1.4034489> (2016).
78. Wu, C. Focal Adhesion: A Focal Point in Current Cell Biology and Molecular Medicine. *Cell Adhes. $\{\&\}$ Migr.* **1**, 13–18. <https://doi.org/10.4161/cam.1.1.4081> (2007).
79. Cardo, L. *et al.* Accessible Synthetic Probes for Staining Actin inside Platelets and Megakaryocytes by Employing Lifeact Peptide. *ChemBioChem* **16**, 1680–1688. <https://doi.org/10.1002/cbic.201500120> (2015).
80. Lickert, S. *et al.* Morphometric analysis of spread platelets identifies integrin $\alpha IIb\beta 3$ -specific contractile phenotype. *bioRxiv* (2018).
81. Nachmias, V. T. & Golla, R. Vinculin in relation to stress fibers in spread platelets. *Cell Motil. Cytoskeleton* **20**, 190–202 (1991).
82. Reinhard, M. *et al.* The 46/50 kDa phosphoprotein VASP purified from human platelets is a novel protein associated with actin filaments and focal contacts. *EMBO J.* **11**, 2063–2070 (1992).
83. Flaumenhaft, R. *et al.* The actin cytoskeleton differentially regulates platelet alpha-granule and dense-granule secretion. *Blood* **105**, 3879–3887. <https://doi.org/10.1182/blood-2004-04-1392> (2005).
84. Woronowicz, K. *et al.* The Platelet Actin Cytoskeleton Associates with SNAREs and Participates in alpha-Granule Secretion. *Biochemistry* **49**, 4533–4542. <https://doi.org/10.1021/bi100541t> (2010).
85. Lee, S. E., Kamm, R. D. & Mofrad, M. R. K. Force-induced activation of talin and its possible role in focal adhesion mechanotransduction. *J. Biomech.* **40**, 2096–2106 (2007).
86. Mierke, C. T. *et al.* Mechano-coupling and regulation of contractility by the vinculin tail domain. *Biophys. J.* **94**, 661–670 (2008).

87. Calderwood, D. A., Campbell, I. D. & Critchley, D. R. Talins and kindlins: partners in integrin-mediated adhesion. *Nat. Rev. Mol. cell Biol.* **14**, 503–517 (2013).
88. Lukinavičius, G. *et al.* Fluorogenic probes for live-cell imaging of the cytoskeleton. *Nat. Methods* **11**, 731–733. <https://doi.org/10.1038/nmeth.2972> (2014).
89. Jen, C. J. & McIntire, L. V. The structural properties and contractile force of a clot. *Cell Motil.* **2**, 445–455. <https://doi.org/10.1002/cm.970020504> (1982).
90. Lam, W. A. *et al.* Mechanics and contraction dynamics of single platelets and implications for clot stiffening. *Nature Materials* **10**, 61–66. <https://doi.org/10.1038/nmat2903> (2010).
91. Nguyen, T. *et al.* Rupture Forces among Human Blood Platelets at different Degrees of Activation. *Sci. Rep.* **6**. <https://doi.org/10.1038/srep25402> (2016).
92. Sorrentino, S., Studt, J.-D., Horev, M. B., Medalia, O. & Sapra, K. T. Toward correlating structure and mechanics of platelets. *Cell Adh. Migr.* **10**, 568–575 (2016).
93. Lam, W. A. *et al.* Mechanics and contraction dynamics of single platelets and implications for clot stiffening. *Nat. Mater.* **10**, 61–66. ISSN: 14764660. <https://doi.org/10.1038/nmat2903> (2010).
94. Soiné, J. R. D. *et al.* Model-based Traction Force Microscopy Reveals Differential Tension in Cellular Actin Bundles. **11** (ed Vikram, D.) e1004076. <https://doi.org/10.1371/journal.pcbi.1004076> (2015).
95. Cassereau, L., Miroshnikova, Y. A., Ou, G., Lakins, J. & Weaver, V. M. A 3D tension bioreactor platform to study the interplay between ECM stiffness and tumor phenotype. *J. Biotechnol.* **193**, 66–69 (2015).
96. Mekhdjian, A. H. *et al.* Integrin-mediated traction force enhances paxillin molecular associations and adhesion dynamics that increase the invasiveness of tumor cells into a three-dimensional extracellular matrix. *Mol. Biol. Cell* **28**, 1467–1488 (2017).
97. Legant, W. R. *et al.* Multidimensional traction force microscopy reveals out-of-plane rotational moments about focal adhesions. *Proc. Natl. Acad. Sci.* **110**, 881–886. <https://doi.org/10.1073/pnas.1207997110> (2012).

98. Blumberg, J. W. & Schwarz, U. S. Comparison of direct and inverse methods for 2.5D traction force microscopy. *{PLOS} {ONE}* **17** (ed Aznar, J. M. G.) e0262773. <https://doi.org/10.1371/journal.pone.0262773> (2022).
99. Liang, X. M., Han, S. J., Reems, J.-A., Gao, D. & Sniadecki, N. J. Platelet retraction force measurements using flexible post force sensors. *Lab Chip* **10**, 991. <https://doi.org/10.1039/b918719g> (2010).
100. Lam, R. H. W., Sun, Y., Chen, W. & Fu, J. Elastomeric microposts integrated into microfluidics for flow-mediated endothelial mechanotransduction analysis. *Lab Chip* **12**, 1865. <https://doi.org/10.1039/c21c21146g> (2012).
101. Zhang, Y. *et al.* Platelet integrins exhibit anisotropic mechanosensing and harness piconewton forces to mediate platelet aggregation. *Proc. Natl. Acad. Sci.* **115**, 325–330. <https://doi.org/10.1073/pnas.1710828115> (2017).
102. Myers, D. R. *et al.* Single-platelet nanomechanics measured by high-throughput cytometry. *Nat. Mater.* **16**, 230–235. ISSN: 14764660 (2017).
103. Zhang, Y., Ge, C., Zhu, C. & Salaita, K. {DNA}-based digital tension probes reveal integrin forces during early cell adhesion. *Nat. Commun.* **5**. <https://doi.org/10.1038/ncomms6167> (2014).
104. Rothenberg, K. E., Neibart, S. S., LaCroix, A. S. & Hoffman, B. D. Controlling cell geometry affects the spatial distribution of load across vinculin. *Cell. Mol. Bioeng.* **8**, 364–382 (2015).
105. Wang, Y. *et al.* Force-activatable biosensor enables single platelet force mapping directly by fluorescence imaging. *Biosens. Bioelectron.* **100**, 192–200. <https://doi.org/10.1016/j.bios.2017.09.007> (2018).
106. Feghhi, S. *et al.* Glycoprotein Ib-IX-V complex transmits cytoskeletal forces that enhance platelet adhesion. *Biophys. J.* **111**, 601–608 (2016).
107. Clegg, R. M. Fluorescence resonance energy transfer. *Curr. Opin. Biotechnol.* **6**, 103–110. [https://doi.org/10.1016/0958-1669\(95\)80016-6](https://doi.org/10.1016/0958-1669(95)80016-6) (1995).
108. Diaspro, A., Bianchini, P., Cella Zanacchi, F. & Usai, C. in *Encycl. Biophys.* (ed Roberts, G. C. K.) 1790–1792 (Springer Berlin Heidelberg, Berlin, Heidelberg, 2013). ISBN: 978-3-642-16712-6. https://doi.org/10.1007/978-3-642-16712-6%7B%5C_%7D826.

109. Gregor, I., Chizhik, A., Karedla, N. & Enderlein, J. Metal-induced energy transfer. *Nanophotonics* **8**, 1689–1699. <https://doi.org/10.1515/nanoph-2019-0201> (2019).
110. Chizhik, A. I. & Enderlein, J. *Metal-Induced Energy Transfer Imaging* (eds Salditt, T., Egner, A. & Luke, D. R.) 227–239. ISBN: 978-3-030-34413-9. https://doi.org/10.1007/978-3-030-34413-9_7B%5C_%7D8 (Springer International Publishing, Cham, 2020).
111. Enderlein, J. Single-molecule fluorescence near a metal layer. *Chem. Phys.* **247**, 1–9 (1999).
112. Karedla, N. *Single-Molecule Metal-Induced Energy Transfer* <https://doi.org/10.1007/978-3-319-60537-1> (Springer International Publishing, 2017).
113. Enderlein, J. A Theoretical Investigation of Single-Molecule Fluorescence Detection on Thin Metallic Layers. *Biophys. J.* **78**, 2151–2158. [https://doi.org/10.1016/s0006-3495\(00\)76761-0](https://doi.org/10.1016/s0006-3495(00)76761-0) (2000).
114. Enderlein, J., Gregor, I. & Ruckstuhl, T. Imaging properties of supercritical angle fluorescence optics. *Opt. Express* **19**, 8011–8018. <http://opg.optica.org/oe/abstract.cfm?URI=oe-19-9-8011> (2011).
115. Karedla, N. *et al.* Three-dimensional single-molecule localization with nanometre accuracy using Metal-Induced Energy Transfer ({MIET}) imaging. *J. Chem. Phys.* **148**, 204201. <https://doi.org/10.1063/1.5027074> (2018).
116. Ghosh, A. *et al.* Graphene-based metal-induced energy transfer for sub-nanometre optical localization. *Nat. Photonics* **13**, 860–865. <https://doi.org/10.1038/s41566-019-0510-7> (2019).
117. Strack, R. {MIET} with graphene. *Nat. Methods* **16**, 1079. <https://doi.org/10.1038/s41592-019-0645-y> (2019).
118. Jannat, R., Dembo, M. & Hammer, D. Traction Forces of Neutrophils Migrating on Compliant Substrates. *Biophys. J.* **101**, 575–584. <https://doi.org/10.1016/j.bpj.2011.05.040> (2011).
119. Munevar, S., Wang, Y. & Dembo, M. Traction Force Microscopy of Migrating Normal and H-ras Transformed 3T3 Fibroblasts. *Biophys. J.* **80**, 1744–1757. [https://doi.org/10.1016/s0006-3495\(01\)76145-0](https://doi.org/10.1016/s0006-3495(01)76145-0) (2001).

120. Schwarz, U. S. & Soiné, J. R. D. Traction force microscopy on soft elastic substrates: A guide to recent computational advances. *Biochim. Biophys. Acta - Mol. Cell Res.* **1853**, 3095–3104. ISSN: 0167-4889. <https://www.sciencedirect.com/science/article/pii/S0167488915001822> (2015).
121. Landau, L. D. *et al.* *Theory of Elasticity: Volume 7* ISBN: 9780750626330. <https://books.google.at/books?id=tpY-VkwCkAIC> (Elsevier Science, 1986).
122. Plotnikov, S. V., Sabass, B., Schwarz, U. S. & Waterman, C. M. in *Methods Cell Biol.* 367–394 (Elsevier, 2014). <https://doi.org/10.1016/b978-0-12-420138-5.00020-3>.
123. Sabass, B., Gardel, M. L., Waterman, C. M. & Schwarz, U. S. High Resolution Traction Force Microscopy Based on Experimental and Computational Advances. *Biophys. J.* **94**, 207–220. <https://doi.org/10.1529/biophysj.107.113670> (2008).
124. Butler, J. P., Tolić-Nørrelykke, I. M., Fabry, B. & Fredberg, J. J. Traction fields, moments, and strain energy that cells exert on their surroundings. *Am. J. Physiol. Physiol.* **282**, C595–C605. <https://doi.org/10.1152/ajpcell.00270.2001> (2002).
125. Delanoë-Ayari, H. *et al.* Changes in the magnitude and distribution of forces at different dictyostelium developmental stages. *Cell Motil. Cytoskeleton* **65**, 314–331. ISSN: 1949-3584 (2008).
126. Aratyn-Schaus, Y., Oakes, P. W. & Gardel, M. L. Dynamic and structural signatures of lamellar actomyosin force generation. *Mol. Biol. Cell* **22** (ed Mogilner, A.) 1330–1339. <https://doi.org/10.1091/mbc.e10-11-0891> (2011).
127. Hui, K. L., Balagopalan, L., Samelson, L. E. & Upadhyaya, A. Cytoskeletal forces during signaling activation in Jurkat T-cells. *Mol. Biol. Cell* **26** (ed Wang, Y.-L.) 685–695. <https://doi.org/10.1091/mbc.e14-03-0830> (2015).
128. Legant, W. R. *et al.* Measurement of mechanical tractions exerted by cells in three-dimensional matrices. *Nat. Methods* **7**, 969–971. <https://doi.org/10.1038/nmeth.1531> (2010).
129. Holenstein, C. N., Silvan, U. & Snedeker, J. G. High-resolution traction force microscopy on small focal adhesions - improved accuracy through optimal marker distribution and optical flow tracking. *Sci. Rep.* **7**. <https://doi.org/10.1038/srep41633> (2017).

130. Lucas, B. D. & Kanade, T. *An iterative image registration technique with an application to stereo vision* in *In IJCAI81* (1981), 674–679.
131. Dracos, T. in *Three-Dimensional Veloc. Vor. Meas. Image Anal. Tech.* 155–160 (Springer Netherlands, 1996). https://doi.org/10.1007/978-94-015-8727-3%7B%5C_%7D7.
132. Lukas, M. A. Strong robust generalized cross-validation for choosing the regularization parameter. *Inverse Probl.* **24**, 34006. <https://doi.org/10.1088/0266-5611/24/3/034006> (2008).
133. Collot, M. *et al.* Bright fluorogenic squaraines with tuned cell entry for selective imaging of plasma membrane vs. endoplasmic reticulum. *Chem. Commun.* **51**, 17136–17139. <http://dx.doi.org/10.1039/C5CC06094J> (2015).
134. Vignaud, T., Ennomani, H. & Théry, M. in *Micropatterning Cell Biol. Part B* (eds Piel, M. & Théry, M.) 93–116 (Academic Press, 2014). <https://www.sciencedirect.com/science/article/pii/B9780124171367000069>.
135. Strale, P.-O. *et al.* Multiprotein Printing by Light-Induced Molecular Adsorption. *Adv. Mater.* **28**, 2024–2029. <https://doi.org/10.1002/adma.201504154> (2015).
136. Melero, C. *et al.* Light-Induced Molecular Adsorption of Proteins Using the {PRIMO} System for Micro-Patterning to Study Cell Responses to Extracellular Matrix Proteins. *J. Vis. Exp.* <https://doi.org/10.3791/60092> (2019).
137. Sanchez, T., Chen, D. T. N., DeCamp, S. J., Heymann, M. & Dogic, Z. Spontaneous motion in hierarchically assembled active matter. *Nature* **491**, 431–434. <https://doi.org/10.1038/nature11591> (2012).
138. Möhle, S. *Stiffness characterisation of hydrogels by nanoindentation* Bachelor's thesis (Georg-August University Göttingen, 2018).
139. Lundkvist, A. *et al.* Viscoelastic Properties of Healthy Human Artery Measured in Saline Solution by {AFM}-Based Indentation Technique. *{MRS} Proc.* **436**. <https://doi.org/10.1557/proc-436-353> (1996).
140. Style, R. W. *et al.* Traction force microscopy in physics and biology. *Soft Matter* **10**, 4047. <https://doi.org/10.1039/c4sm00264d> (2014).

141. Simič, R., Mathis, C. H. & Spencer, N. D. A two-step method for rate-dependent nano-indentation of hydrogels. *Polymer (Guildf)*. **137**, 276–282. ISSN: 0032-3861. <https://www.sciencedirect.com/science/article/pii/S0032386118300181> (2018).
142. Fortun, D., Bouthemy, P. & Kervrann, C. Optical flow modeling and computation: A survey. *Comput. Vis. Image Underst.* **134**, 1–21. <https://doi.org/10.1016/j.cviu.2015.02.008> (2015).
143. Bouguet, J.-y. Pyramidal implementation of the Lucas Kanade feature tracker. *Intel Corporation, Microprocessor Research Labs* (2000).
144. Schindelin, J. *et al.* Fiji: an open-source platform for biological-image analysis. *Nat. Methods* **9**, 676–682. <https://doi.org/10.1038/nmeth.2019> (2012).
145. Phillips, D. L. A Technique for the Numerical Solution of Certain Integral Equations of the First Kind. *J. {ACM}* **9**, 84–97. <https://doi.org/10.1145/321105.321114> (1962).
146. Golub, G. H., Heath, M. & Wahba, G. Generalized Cross-Validation as a Method for Choosing a Good Ridge Parameter. *Technometrics* **21**, 215–223. <https://doi.org/10.1080/00401706.1979.10489751> (1979).
147. Huang, Y. *et al.* Traction force microscopy with optimized regularization and automated Bayesian parameter selection for comparing cells. *Sci. Rep.* **9**, 1–16 (2019).
148. Tukey, J. W. An introduction to the calculations of numerical spectrum analysis. *Adv. Semin. Spectr. Anal. Time Ser.* (1967).
149. *MATLAB Optimization Toolbox* 2020.
150. Kittler, J. & Illingworth, J. Minimum error thresholding. *Pattern Recognit.* **19**, 41–47. [https://doi.org/10.1016/0031-3203\(86\)90030-0](https://doi.org/10.1016/0031-3203(86)90030-0) (1986).
151. Natan. *Fast 2D peak finder* 2021. <https://www.mathworks.com/matlabcentral/fileexchange/37388-fast-2d-peak-finder>.
152. Michelson, A. D. *Platelets* 3. Aufl. ISBN: 978-0-123-87837-3. <https://doi.org/10.1016/c2016-0-03693-8> (Elsevier, Amsterdam, Boston, 2013).
153. Blockmans, D., Deckmyn, H. & Vermylen, J. Platelet actuation. *Blood Rev.* **9**, 143–156 (1995).
154. Loftus, J. C. & Albrecht, R. M. Redistribution of the fibrinogen receptor of human platelets after surface activation. *J. Cell Biol.* **99**, 822–829 (1984).

155. van Nispen tot Pannerden, H. *et al.* The platelet interior revisited: electron tomography reveals tubular α -granule subtypes. *Blood* **116**, 1147–1156. <https://doi.org/10.1182/blood-2010-02-268680> (2010).
156. Pokrovskaya, I. D. *et al.* STEM tomography reveals that the canalicular system and α -granules remain separate compartments during early secretion stages in blood platelets. *J. Thromb. Haemost.* **14**, 572–584. <https://doi.org/10.1111/jth.13225> (2016).
157. Isbaner, S. *et al.* Dead-time correction of fluorescence lifetime measurements and fluorescence lifetime imaging. *Opt. Express* **24**, 9429–9445. <http://www.opticsexpress.org/abstract.cfm?URI=oe-24-9-9429> (2016).
158. Nelder, J. A. & Mead, R. A simplex method for function minimization. *Comput. J.* **7**, 308–313 (1965).
159. Karedla, N. *et al.* Single-Molecule Metal-Induced Energy Transfer (smMIET): Resolving Nanometer Distances at the Single-Molecule Level. *ChemPhysChem* **15**, 705–711 (2014).
160. Yermolenko, I. S. *et al.* The Assembly of Nonadhesive Fibrinogen Matrices Depends on the α C Regions of the Fibrinogen Molecule. *J. Biol. Chem.* **287**, 41979–41990. <https://doi.org/10.1074/jbc.m112.410696> (2012).
161. Sandmann, R. & Köster, S. Topographic Cues Reveal Two Distinct Spreading Mechanisms in Blood Platelets. *Sci. Rep.* **6**. <https://doi.org/10.1038/srep22357> (2016).
162. Jiroušková, M., Jaiswal, J. K. & Coller, B. S. Ligand density dramatically affects integrin α IIb β 3-mediated platelet signaling and spreading. *Blood* **109**, 5260–5269. <https://doi.org/10.1182/blood-2006-10-054015> (2007).
163. Darwich, Z., Klymchenko, A. S., Dujardin, D. & Mély, Y. Imaging lipid order changes in endosome membranes of live cells by using a Nile Red-based membrane probe. *{RSC} Adv.* **4**, 8481–8488. <https://doi.org/10.1039/c3ra47181k> (2014).
164. Leys, C., Ley, C., Klein, O., Bernard, P. & Licata, L. Detecting outliers: Do not use standard deviation around the mean, use absolute deviation around the median. *J. Exp. Soc. Psychol.* **49**, 764–766. <https://doi.org/10.1016/j.jesp.2013.03.013> (2013).

165. Patel-Hett, S. *et al.* Visualization of microtubule growth in living platelets reveals a dynamic marginal band with multiple microtubules. *Blood* **111**, 4605–4616. <https://doi.org/10.1182/blood-2007-10-118844> (2008).
166. Holme, P. A. *et al.* Shear-Induced Platelet Activation and Platelet Microparticle Formation at Blood Flow Conditions as in Arteries With a Severe Stenosis. *Arterioscler. Thromb. Vasc. Biol.* **17**, 646–653. <https://doi.org/10.1161/01.atv.17.4.646> (1997).
167. Litvinov, R. I. *et al.* Polymerization of fibrin: direct observation and quantification of individual B:b knob-hole interactions. *Blood* **109**, 130–138. <https://doi.org/10.1182/blood-2006-07-033910> (2006).
168. Jennings, L. Mechanisms of platelet activation: Need for new strategies to protect against platelet-mediated atherothrombosis. *Thromb. Haemost.* **102**, 248–257. <https://doi.org/10.1160/th09-03-0192> (2009).
169. Storey, R. & Thomas, M. The role of platelets in inflammation. *Thromb. Haemost.* **114**, 449–458. <https://doi.org/10.1160/th14-12-1067> (2015).
170. Johnoson, G. J., Leis, L. A., Krumwiede, M. D. & White, J. G. The critical role of myosin {IIA} in platelet internal contraction. *J. Thromb. Haemost.* **5**, 1516–1529. <https://doi.org/10.1111/j.1538-7836.2007.02611.x> (2007).
171. Dmitrieff, S., Alsina, A., Mathur, A. & Nédélec, F. J. Balance of microtubule stiffness and cortical tension determines the size of blood cells with marginal band across species. *Proc. Natl. Acad. Sci.* **114**, 4418–4423. <https://doi.org/10.1073/pnas.1618041114> (2017).
172. Hartwig, J. H. Mechanisms of actin rearrangements mediating platelet activation. *J. Cell Biol.* **118**, 1421–1442. <https://doi.org/10.1083/jcb.118.6.1421> (1992).
173. Hartwig, J. H. *et al.* Thrombin receptor ligation and activated rac uncap actin filament barbed ends through phosphoinositide synthesis in permeabilized human platelets. *Cell* **82**, 643–653. [https://doi.org/10.1016/0092-8674\(95\)90036-5](https://doi.org/10.1016/0092-8674(95)90036-5) (1995).
174. Hartwig, J. H. *et al.* D3 Phosphoinositides and Outside-in integrin Signaling by Glycoprotein {IIb}-{IIIa} Mediate Platelet Actin Assembly and Filopodial Extension Induced by Phorbol 12-Myristate 13-Acetate. *J. Biol. Chem.* **271**, 32986–32993. <https://doi.org/10.1074/jbc.271.51.32986> (1996).

175. Calaminus, S. D. J. *et al.* {MyosinIIa} contractility is required for maintenance of platelet structure during spreading on collagen and contributes to thrombus stability. *J. Thromb. Haemost.* **5**, 2136–2145. <https://doi.org/10.1111/j.1538-7836.2007.02696.x> (2007).
176. Solh, T., Botsford, A. & Solh, M. Glanzmann's thrombasthenia: Pathogenesis, diagnosis, and current and emerging treatment options. *J. Blood Med.* **2015**, 6–219 (2015).
177. Lanza, F. Bernard-Soulier syndrome (Hemorrhagic thrombocytopenic dys-trophy). *Orphanet J. Rare Dis.* **1**. <https://doi.org/10.1186/1750-1172-1-46> (2006).
178. Ghosh, A., Chizhik, A. I., Karedla, N. & Enderlein, J. Graphene- and metal-induced energy transfer for single-molecule imaging and live-cell nanoscopy with (sub)-nanometer axial resolution. *Nat. Protoc.* **16**, 3695–3715. <https://doi.org/10.1038/s41596-021-00558-6> (2021).
179. Qiu, Y. *et al.* Platelet mechanosensing of substrate stiffness during clot formation mediates adhesion, spreading, and activation. *Proc. Natl. Acad. Sci. U.S.A.* **111**, 14430–14435. <https://doi.org/10.1073/pnas.1322917111> (2014).
180. Inaba, S., Fujino, S. & Morinaga, K. Young's modulus and compositional parameters of oxide glasses. *J. Am. Ceram. Soc.* **82**, 3501–3507 (1999).

Acknowledgements

Finally, I would like to thank everyone who helped me along the way. Without your support, I would not have been able to accomplish this goal as it is.

First of all, I would like to thank my supervisor **Prof. Sarah Köster**, who never gave up on me and allowed me to work on such a great topic with her amazing team. Thank you for all your constructive feedback during meetings and for many interesting collaborations. Thanks to **Dr. Florian Rehfeldt** for being part of my thesis committee and the second reviewer of my thesis and for all the suggestions and helpful discussions during the meetings and conferences. Thanks also to **Dr. Marco Tarantola** for all the advice and ideas as a member of my thesis committee. I am grateful to **Prof. Timo Betz**, **Prof. Andreas Janshoff**, **Prof. Stefan Klumpp** and **Prof. Niels Voigt** for being a part of my examination board. Thanks to **Dr. Alexey Chizhik** and his wife **Dr. Anna Chizhik** for all the great discussions during collaboration on my first paper. Thanks also to **Dr. Sebastian Isbaner** and **Dr. Daja Ruhlandt** for all your time with data analysis and for explaining all the fascinating theories behind MIET. Great thanks also come to **Prof. Ulrich Schwarz** and **Johannes Blumberg** from the University of Heidelberg for the theory discussion behind traction force microscopy and their help with understanding all analytical steps. Big thanks to all **IRP** group members, who were kept together at all times and always tried to keep the healthy optimism also during the pandemic. I thank the **University of Göttingen Klinikum** for providing us the platelet concentrates and also for a friendly atmosphere. Big thanks come to the secretaries, **Christine Wilke-Feist**, **Kerstin Pluschke** and **Michaela Ständer** for all your help with my paper works and administrative care. An extra thanks come to **Jan Goeman** for all the IT troubles you solved for me and to **Peter Luley** thanks to you; no technical problem was left unresolved. Thanks to **Susanne Bauch** for the great and funny chatting in the lab. Big thanks also come

to **Dr. Ulrike Rölleke** and **Kamila Sabagh**, who always helped me in the lab. A great thanks to you all for all the support and a friendly working environment.

I can see it like yesterday, my first days in Germany, confused about the bureaucracy and all paperwork. I would never be able to finish without my office girls in the first place. Thank you, **Manu**, for always staying on my side and cheering me up when my days were blue. To **Julia** for calling my doctor's appointments, driving lessons, listening, and baking the most amazing cakes! Without you girls, I would never survive in the adult world. Thanks to **Jana** for introducing me to the topic of blood platelets and showing me all tricks on how to process them. Thank you for taking your free time for useful discussions and giving me some extra Swedish lessons. Thanks also come to **Magdalena** for all the nice talks and help with my project. I also have to thank all my students I had a chance to meet, especially for my bachelor students **Swantje** and **Sarah**, who I am always happy to meet. A special thanks to my **An ACE** group, namely **Anna B.** and my Italian friends **Chiara** and **Eleonora** for being the coolest people on the planet! To **Andrew** and his big heart and shared love for all German shepherds, to **Heidi** for all the crazy situations and conversations we had, to **Lotta** for saying the most amazing and clever things at the right moment. A huge thanks come to **Anna (Nr. 1)**, without you I would never be able to finish in time. Thank you **Ruth** for being around when I needed a hug. To **Charlotte** for making a friendly environment and always a friendly mood. To **Jan-Philipp** and **Gerrit** for being great companions for an early lunch. I would like to thank you all for your support during writing, especially big thanks to Anna and Anna, Julia and Chiara for reading and brainstorming 24/7.

I want to thank all people I had a chance to meet in Göttingen, inside or outside the University. For amazing hiking tours and showing the outside of the city as well. Thanks to all of you, I felt here like I belong to a big family. However, I should not forget to thank my family, parents and siblings for always keeping me motivated, taking me on fishing trips. My deepest thanks to **Andreas**, for being my partner in crime and his family, for always supporting me, and finally teaching me to speak proper German. Thank you for making me the person I am today. To all my friends around the world, it has been a bumpy ride and I will never forget your parts in that journey!

Abbreviations

AFM	Atomic force microscopy
APS	Ammonium persulfate
ADP	Adenosin diphosphate
ATP	Adenosin triphosphate
BSA	Bovine serum albumin
CCD	Charged-coupled device
CLSM	Confocal laser scanning microscopy
CMOS	Metal-oxide-semiconductor
Cy5	Cyanine 5 dye
DMD	Digital micro-mirror device
DMSO	Dimethyl sulfoxide
dSQ12S	squaraine dye with two zwitterionic amphiphilic anchors
dSTORM	Direct Stochastic optical reconstruction microscopy
ECM	Extracellular matrix
EMT	Epithelial-to-mesenchymal transition
FA(s)	Focal adhesion(s)
F-actin	Filamentous actin
FITC	Fluorescein isothiocyanate
FLIM	Fluorescence lifetime imaging microscopy
FTTC	Fourier transform traction cytometry
FRET	Föster resonance energy transfer
G-actin	Globular actin
GFP	Green fluorescent protein
GP	Glykoproteins
HT	HEPES-Tyrode
HPICM	Hopping probe ion conductance microscopy
IRF	Instrument response function
ITS	Integrative tension sensor
KLT	Kanade-Lucas-Tomasi algorithm

LEDs	Light-emitting diode
LIMAP	Lighth-induced molecular adsorption of proteins
MB	Marginal band
MK(s)	Megakaryocyte(s)
MIET	Metal-induced energy transfer
MQ	MilliQ, ultra-pure water
MRD	Mean radial distance
NA	Numerical aperture
OCS	Open canalicular system
PAA	Polyacrylamide
PAR	Protease-activated receptor
PBS	Phosphate buffered saline
PCC	Platelet contraction cytometry
PDMS	Poly(dimethylsiloxane)
PGE1	Prostaglandin E1
PLPP	Product of Liaison for Protein Patterning
PSG	PIPES Saline Glucose
QE	Quantum efficiency
QY	Quantum Yield
RICM	Reflection interference contrast microscopy
ROCK	Rho kinase
ROI	Region of interest
RT	Room temperature
SEM	Scanning electron microscopy
SICM	Scanning ion-conductance microscopy
SIM	Structured illumination microscopy (SIM)
SiR	Silicon-rhodamine
STED	Stimulated emission depletion
TCSPC	Time-correlated single photon counting
TEM	Transmitting electron microscopy
TEMED	Tetramethylethylenediamine
TIRF	Total internal reflection fluorescence
TF	Tissue factor
TFM	Traction force microscopy
TMSPMA	3-(Trimethoxysilyl)propyl methacrylate
TTTR	Time-tagged time-resolved

vWF	von Willebrand factor
2D	Two-dimensional
3D	Three-dimensional

List of Publications

- Anna Zelená, Sebastian Isbaner, Daja Ruhlandt, Anna Chizhik, Chiara Cassini, Andrey S. Klymchenko, Jörg Enderlein, Alexey Chizhik and Sarah Köster, "Time-resolved MIET measurements of blood platelet spreading and adhesion", In: *Nanoscale* 12.41 (2020), pp. 21306-21315. DOI: 10.1039/D0NR05611A.
- Daniel Meyer, Saba Telele, Anna Zelená, Alice J. Gillen, Alessandra Antonucci, Elsa Neubert, Robert Nißler, Florian A. Mann, Luise Erpenbeck, Ardemis A. Boghossian, Sarah Köster and Sebastian Kruss, "Transport and programmed release of nanoscale cargo from cells by using NETosis", In: *Nanoscale* 12.16 (2020), pp. 9104-9115. DOI: 10.1039/D0NR00864H.